SIGNAL ACQUISITION, MODELING AND ANALYSIS OF THE PULMONARY CIRCULATION SYSTEM

by

Ye Jian
(葉 健)

A Dissertation

Submitted in partial fulfilment of the requirements

for the degree of

Doctor of Philosophy

in

Department of Electronic Engineering

The Chinese University of Hong Kong

May 1993

To my wife Dan-Hong

and my son Cong-Hua

SIGNAL ACQUISITION, MODELING AND ANALYSIS OF THE PULMONARY CIRCULATION

ABSTRACT

In recent years, much attention has been focused on the clinical application of the electrical impedance rheopneumography (EIR) in China. This technique, though simple and non-invasive in nature, is not without certain basic problems. These include determination of optimal electrode size and configuration, elimination of the respiratory artefact, development of physiologically based analysis and last but not the least development of suitable technique for real-time (RT) monitoring applications[1].

In the human thoracic section the origins of impedance change include the lungs, the heart and vascular beds of the systemic and pulmonary circulations. All these origins contribute to the measured impedance signal. It was found that the composition of the impedance signal depended much on the electrode positions and size. Moreover it is difficult if not impossible to determine this composition via measurements alone. In doing this, a 2D numerical model had been developed and computer simulations carried out. With precisely assigning tissue resistivity, the differential potential distribution within the model between end systolic and end diastolic states of the heart was calculated via the finite element method. The simulation results not only gave the wave composition of conventional electrode configuration, but also provided a suggestion of optimum electrode configuration with which the impedance signal can be measured with the least interference from other origins

In order to eliminate the respiratory artefact, several signal processing techniques with real time and adaptive features had been studied in the simple and modified forms. These

[1] The BME laboratory of Dept. of Electronic Eng. of CUHK, in cooperation with the Pulmonary Function Lab of Dept. of Medicine, CUHK and Dept. of Respiratory Medicine at Guangxi Medical University at Nanning, is actively engaged in works towards tackling the above mentioned problems, with a view of eventually the technique of EIR, a useful clinical diagnostic tool for RT monitoring and analyzing the pulmonary circulation much ignored over the years.

include the adaptive noise canceller (ANC), the moving averager (MA) and the FIR filter. A modified ANC method had been developed such that the respiratory reference signal was picked up from another pair of impedance detecting electrodes. In its reference path a MA was applied to make the cardiac component insignificant. With these modifications, better signal-to-noise ratio (SNR) and signal-distortion ratio (SDR) in the ANC output could be obtained. As the ANC method might fail in some case in view of its finite time of convergence, improvements to the simple MA and FIR filter were made by adding adaptive feature to these filters. DFT technique was applied to track the frequencies of the respiratory and rheopneumographic components so that at any time an optimum cutoff frequency could be determined. For the adaptive FIR filter, a coefficient look up table (CLT) was used so that all coefficients could be reset by searching them from the CLT when the cutoff frequency changed. We have implemented and compared the three filters. Results show that the adaptive FIR filter presents the best performance in terms of SNR and SDR and the modified MA is the fastest and simplest in implementation.

For the analysis of rheopneumogram, an EIR modeling method was proposed which could reflect the state of the pulmonary circulation in terms of the blood vessel compliance, the blood inertance and the peripheral resistance to blood flow and other related factors. This model is mainly based on the two-chamber lumped model in view of the impedance measurement itself is a lumped effect. A two-stage parameter identification scheme, viz curve fitting the model output to the measured data and solving the parameter equations, was proposed to estimate the model parameters from a given measured waveform. Thus from the impedance measurement, both of the physical and physiological properties of the pulmonary circulation can be estimated. This modeling method has been verified with some specific physical and pathological data. Results show good agreements between the model parameters and the known physical and physiological pictures.

肺血阻抗圖信號之優化提取、呼吸干擾的去除與模型分析

（摘　要）

近年來，肺血阻抗圖技術在臨床應用上受到廣泛重視。雖然這項技術具有非損傷性及儀器簡單的優點，但仍存在一些尚未解決的根本問題，包括確定最佳電極擺放位置、去除呼吸干擾以及分析阻抗圖所反應的生理和病理意義。針對上述問題，本文進行了一些探索並且提出和建立了一套肺血圖實時監測與分析技術。

在人體胸腔中，阻抗變化源有肺、心臟和體循環與肺循環中的血流。在以往的測量中，我們發現肺阻抗圖的成份與電極的大小及擺放位置有很大關系。但是在實際測量上，卻無法有效計算出各個變化源的成份。爲此，我們在電腦中構造出一個二維數值模型，模擬人體胸部的一個橫截面並且利用有限元方法計算其中之電勢分佈。當心臟從舒展期末狀態變化到收縮期末時，由於各個阻抗源的體積變化，數值模型中的電勢分佈也會產生相應之變化。根據此電勢變化分佈圖，我們可以計算出阻抗圖中來自各個源的成份和找出最佳電極設置。在此設置下，肺循環產生的阻抗變化具有最顯著的效應而其它阻抗變化源產生的效應近乎等于零。

對於呼吸干擾的去除，我們著重於研究具實時處理及自適應改變截止頻率功能的濾波器。這包括改進的自適應噪聲消除濾波器（MANC）、改進的自適應移動窗口濾波器（MMA）與自適應有限沖激響應濾波器（AFIR）。

改進型自適應噪聲濾波器的呼吸參考信號是通過另外一對阻抗提取電極在第五及第六條肋骨位間提取。同時利用一個簡單的移動窗口低通濾波器（SMA）處理提取到的阻抗呼吸信號以期進一步減少其

中肺血圖信號的成份。如此，在ＭＡＮＣ的輸出端，我們可以取得較好的信噪比。

由于自適應噪聲消除方法未能快速跟蹤呼吸信號的變化，因此在某些情況下，ＭＡＮＣ的ＬＭＳ算法未能處於收斂穩定的狀態，所處理的信號具有較大變形。針對這種情況，考慮ＦＩＲ濾波器具有穩定及線性相位的特性，我們對其進行研究並且加以改進。只要能針對肺血圖及呼吸信號的特點（時變頻率特性），實時地改變濾波器的截止頻率，就能得到一個較理想的濾除呼吸噪聲之輸出信號。對此，我們利用快速離散付里葉技術實時獲取所需截止頻率並且提出一個濾波器系數查對表技術。當截止頻率改變時，不需重新計算濾波器的系數，而只根據截止頻率，就可以在查對表中獲得所需之系數。這樣節省了重新計算所需時間，加快了處理速度。

我們還考慮了這個自適應ＦＩＲ濾波器的一個特殊情形，即自適應平滑窗口濾波器。由於它的各個系數相同，所以需求的乘法次數大大減少，進一步提高了處理速度。

最後，對於肺血圖信號的分析，我們提出一種模型分析方法。它可以根據測量的波形計算出肺循環中血管的柔順性、血流的慣性以及血流阻力等參數。由於阻抗測量法是一種區域效應的測量，因此本文提出的模型以一種稱爲"雙腔"的集中參數模型爲基礎。爲計算出模型中的各項參數，我們提出一個二步參數估計法。首先用曲線擬合技術計算出擬合函數的各項系數。然後求解模型參數方程，得到模型的各項參數。爲証明模型方法的有效性，我們研究了兩類特殊生理現像，如要求受試者改變姿式與呼吸狀態等。對兩種特殊病理現像如二尖瓣狹窄與阻塞性肺氣腫也做了測試。結果顯示出模型的參數與相應的生理及病理現像相當符合。

ACKNOWLEDGEMENTS

I would like to express my deepest appreciation and gratitude to my supervisor, Mr. Thomas T. C. Choy, for his continuous guidance and support throughout the years of this research work, and for his patient reading and useful comments in the preparation of this thesis and other manuscripts.

I am grateful to the help of Professor J. F. Xiong and his research group at Guangxi Medical University, and Dr H. S. Chan of the Medicine Dept, CUHK. The animal experiments and clinical observations reported in this thesis show their importance.

It is my pleasure to thank Mr S. M. Chu, who helped me in many aspects during the work. Special thanks to Dr K T Lo for his useful suggestions to the format and style of this thesis. Thanks also to Gary Leung, Franky Fan, K. Y. Yu, and Alan G. Miller. Without them there would not be so much enthusiasm and vitality in the BME-228.

I wish to express my sincerely gratitude to all my friends from PRC pursuing their PhD degrees here. We have shared not only our knowledge of science but also many depressed and happy times.

Finally, but not the least, I am indebted to my wife and parents for their patience, understanding and encouragement during my years of study. They have been taking care all the family affairs so that I can concentrate on my work.

LIST OF ABBREVIATIONS

2D	Two dimension
3D	Three dimension
A/D	Analog to digital conversion
AC	Alternating current
AFIR	adaptive FIR
AM	Amplitude modulation
AMA	adaptive MA
ANC	Adaptive noise canceller
ANC&RIP	ANC with RIP as the reference input
CCU	Cardiac care unit
CLT	Coefficient look-up table
DAS	Data acquisition system
DC	Direct current
DFT	Digital fourier transform
EBI	Electrical Bio-impedance
ECG	Electrocardiography
EIR	Electrical impedance rheopneumograph-y or -ic
EIT	Electrical impedance tomography
EM	Electro-Magnetic
FEM	Finite element method
FIR	Finite impulse response
g(t)	The conductivity at every point in space at time t
GMU	Guangxi Medical University
Hc	The amplitude of C-wave
Hz	The amplitude of Z-wave
ICU	Intensive care unit

LMS	Least mean square
MA	Moving averager
MANC	Modified ANC
MMA	Modified MA
PA	Main pulmonary artery
PC	Pulmonary capillaries
PCG	Phonocardiography
PNT	Pneumotachography
PV	Pulmonary veins
REG	Rheoencephalography
RIP	Respiratory inductance plethysmography
RPTRC	The composite ratio of the right pulmonary circuit response to remaining circulatory system response
RT	Real time
SDR	Signal distortion ratio
SMA	Simple moving averager
SNR	Signal to noise ratio
SNRI	Signal to noise ratio improvement
TIS	Transthoracic impedance signal
VOP	Venous occlusion phlebography
Z(t)	The measured impedance at time t

TABLE OF CONTENTS

CHAPTER 1 INTRODUCTION

1.1 WHAT IS THE EBI TECHNIQUE

The EBI is a non-invasive technique widely applied to detect the impedance signals of bio-systems and the term of EBI is abbreviated from Electrical Bio-Impedance. Since the first international conference on EBI held in New York in 1969, tremendous progress have been made in the various aspect of EBI technique ([ICEB 81] [ICEB 83] [ICEB 87] [ICEB 92]).

Through injecting a low amplitude (eg. 1 mA) and high frequency (eg. 100 kHz) alternating current into the human body with surface electrodes, the total tissue impedance as well as any physiological event which can exhibit a change in dimension, dielectric, or conductivity or a rearrangement (geometric variation) of these components between the surface electrodes can be detected by the EBI technique. It is extremely practical for phenomena that produce a large change in one or more of the quantities just mentioned. As such, the potential applications can be found in the detection of blood flow, cardiac activity, respired volume, bladder, blood, kidney volumes, uterine contractions, nervous activity, the galvanic skin reflex, the volume of blood cells, clotting, blood pressure, and salivation. In some instances the impedance is separated into its resistive and reactive components; in others, the total impedance is measured.

While comparing to other available techniques such as X-ray, ultrasound, nuclear magnetic resonance, etc, this EBI technique is very attractive in many aspects because of its non-invasive nature and simple equipments involved. First and the most important is that in many applications the integument need not be penetrated to make the measurement. Second, practicality is an attractive feature of the method since no specialized transducers but electrodes are required and unlike many transducers, electrodes are affected little by temperature and barometric pressure changes in conventional impedance measurements. Third, the impedance signal is detected through employment of frequency carrier-system techniques, which permit the use of narrow-band amplifiers with consequent enhancement of the signal-

to-noise ratio.

1.2 APPLICATIONS OF THE EBI TECHNIQUE

The EBI technique has been actively applied to monitor physiological events for many years. These applications can be classified into several categories by the kind of observation involved for different purposes viz, detecting the values of absolute impedance and its change, monitoring and analyzing the morphological variations of impedance waveforms. The former kind of observation can be easily and simply carried out which extracts some indices such as the peak amplitude, maximum slope, etc. However, the latter can provide much information because of the morphological change in the waveform closely relating to the system characteristics.

The absolute impedance value can reflect the resistive and reactive properties of the tissues between the electrodes. However, the reactive component of the impedance can almost be ignored at the frequencies used for impedance measurement (50-100 kHz). Applications of this kind include the assessment and detection of body fat, pulmonary edema, tumor, etc. Volumes of such organs can be estimated via the absolute impedance with suitable calibration of the EBI measuring unit.

Impedance phlebography ([WHEE 73] [WHEE 74]) is such an application which detects the venous occlusion in extremities (well known as VOP). With this technique, the basal impedance of a segment of an extremity (arm or leg) is measured. When the venous outflow is occluded, a decrease in impedance occurs due to swelling of the blood. If the major veins are obstructed by a blood clot, the initial volume increase (indicated by a decrease in impedance) is smaller than in the normal subject.

Impedance changes reflecting cardiac activity or the impedance cardiogram can be measured if electrodes are placed to encompass the thorax ([KUBI 74]). A number of investigators have studied the thoracic impedance cardiogram, hoping to calibrate it in terms of the systolic discharge from the heart. Probably the earliest were Atzler and Lehmann

(1932), who placed metal-plate electrodes in front of and behind the thorax and detected ultrahigh-frequency impedance changes synchronous with cardiac activity.

Thoracic impedance cardiography continues to be actively investigated because it is virtually the only noninvasive method available to estimate stroke volume (the volume of blood ejected with each heart beat), cardiac output and cardiac indices. Nyboer developed what is now called the backslope or end-systolic extrapolation technique ([NYBO 59]) to obtain a value for the impedance change ΔZ that reflects the cardiac output. Many verifications and modifications to this work have also been made ([ALLI 65] [KUBI 66] [BILL 86] [MUZI 85a] [BARA 92]).

The EBI waveform has been widely used to monitor and analyze the cardiac and respiratory signals because of its noninvasive nature. From the waveform morphology, some properties of the physiological systems can be estimated. The use of the EBI technique for recording peripheral volume pulses was first described by Mann. Within a few years there appeared numerous papers on the subject, and the technique soon became known as impedance plethysmography. Pioneering in this field were Nyboer et al ([NYBO 44] [NYBO 50] [NYBO 59]). His studies included recording impedance pulsations from almost every area of the body. Since then, a number of investigators have evaluated such measurements for diagnosing peripheral arterial disease ([BROW 85] [WEBS 90]).

Impedance plethysmograph can be used to detect respiration and this is known as the impedance pneumography. Since the conductivity of air is very low, when a man breathes, his lung is full of air and the conductivity of this region decreases which resulting in an impedance change. In 1926, Lanbert and Gremels first used contact electrodes and AC Wheatstone bridge to monitor the impedance between two electrodes placed on the surface of the lung and to follow impedance changes caused by the development of pulmonary edema.

Besides the applications mentioned above, there are still many other applications such as the impedance rheoencephalography or REG which is employed to assess cerebral blood

flow [HADI 72]; the impedance rheopneumography which is the major theme of this thesis and will be introduced in the next section.

1.3 THE ELECTRICAL IMPEDANCE RHEOPNEUMOGRAPHY-AN OVERVIEW

Of the many applications of the EBI technique, the Electrical Impedance Rheopneumography (EIR) or the study of the pulmonary circulation has attracted much attention in China but not so in the West. The latter has paid more attention to the impedance cardiography. Since both of the impedance rheopneumogram and impedance cardiogram are measured with the thoracic surface electrodes, there are some similarities between these two signals and sometimes they may merge together and interferes with each other.

The EIR is very useful since it is the only noninvasive method to detect the blood flows in the pulmonary circulation. The measured waveform can reflect the properties of the right heart, the lung and the pulmonary blood vessels. In China, there are many researchers and clinicians using this method to study the diseases of pulmonary circulation. *However, there are some factors with this method which have much restricted its becoming a popular clinical tool. These include the interference of the systemic circulation, the respiratory artefact and the assessment method of the rheopneumographic waveform.*

Figure 1.1 shows the conventional electrode configuration and equipment setup for rheopneumographic measurement. The electrodes are positioned as close as possible to the object of interest (eg. the right lung) just according to the anatomic view. Since the human body is not a homogeneous medium, the current lines in it do not necessarily go in straight lines but diverge in a way unknown. As a result, a purely anatomically based placement scheme can hardly guarantee a resulting signal that is optimised with respect to such interfering sources, particularly those coming from the major components of the systemic circulation for reasons as stated above. Moreover, the resulting signal can be a composite wave consisting of components of useful and interfering sources, and the composition may change with the positions of detecting electrodes. Although this is so obvious, no report has been given as to how an optimum electrode configuration can be found such that one can pick

up the rheopneumographic signal with the least interference from the systemic circulation.

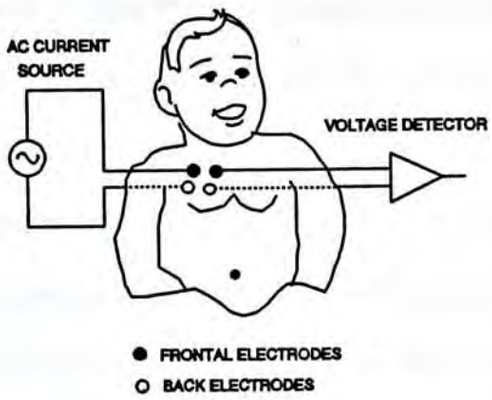

Figure 1.1 Diagram of rheopneumogram measurement

The respiratory artefact has a much bigger amplitude and a varying spectrum near to or even inbanded at times in the rheopneumographic spectrum. Figure 1.2 shows a typical transthoracic impedance signal taken along with the ECG, dZ/dt and PCG. The spectrum of the impedance signal in the insert, shows a large respiratory artefact and the spectra inbanding can be observed. As such, no conventional method of filtering is effective in this respiratory artefact suppression. To remove the respiratory artefact, the conventional method used in practice is to ask the subject to hold his/her breath during measurement. This requirement can be easily carried out by normal people. But for those with problems in the lung and respiratory system, it is not an easy thing to do and usually may affect the waveform pattern because of unnatural respiratory conditions. Moreover, the rheographic waveforms are somewhat different for different apneic states and for prolonged period of apnea, the waveform also changes progressively ([YE 92]). In the extreme cases of patients with severe respiratory problems, application of the apneic technique is totally impossible.

The existing method of the assessment of the impedance waveform has been based mainly on the computation of the absolute, relative or ratiometric values of peak amplitude, time intervals or delays relative to some ECG or PCG landmarks ([WEGL 83] [LI 83a]). This

method can be best described in figure 1.3 which shows the significant indices including *Hz*, the amplitude of Z-wave; *Hc*, the amplitude of C-wave; Q-j interval, the time interval between the Q point of ECG and the starting point of the leading edge of Z-wave, and the like. Since the peak positions of C-wave and even the Z-wave are not so significant in some circumstances and these can result in difficulties in extracting the indices mentioned above. Moreover, as the physiological conditions or dynamic behaviour are not readily available from such assessed parameters, the etiopathology or at times the differential diagnosis is not too obvious. At present, there are many assessment methods based on such indices in China and as a result, different diagnostic methods are used among the research groups and in clinical settings in hospitals and hence it is hard for one to follow the method of other's.

1.4 GOAL OF THE WORK

In view of the above problems and difficulties in the application of the EIR technique, this work is mainly concentrated on studying these problems and finding solutions in the engineering and physiology viewpoint.

Firstly, we need to find all possible origins and the composition of the measured signal with a given electrode configuration. Following this an optimum electrode configuration is found with which one can obtain a right signal just reflecting the pulmonary circulation and having the least interference from other origins. This is very important for further analysis of the rheopneumographic signal. Since if interference signal exists, the analysis result will be inaccurate. In practical measurements, it is difficult or impossible for one to determine the composition of the measured signal, because all the origins are active at the same time. However, with the computer simulation, all origins can be controlled to be active together or individually. As such, an approach based on a numerical model and computer simulation is proposed. The cardiac activities can be simulated in this model so that the composition of the resulted signal be estimated.

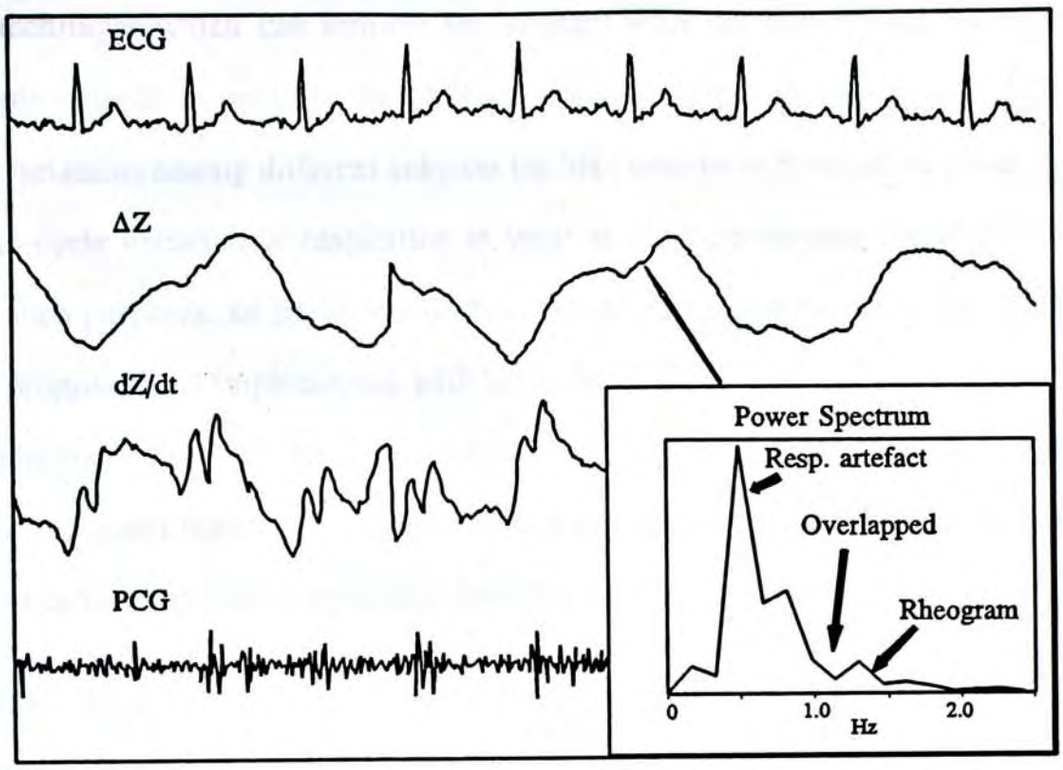

Figure 1.2 A typical transthoracic impedance waveform (ΔZ) recorded along with its first derivative (dZ/dt), ECG and phonocardiogram (PCG); The power spectrum of ΔZ is shown in insert.

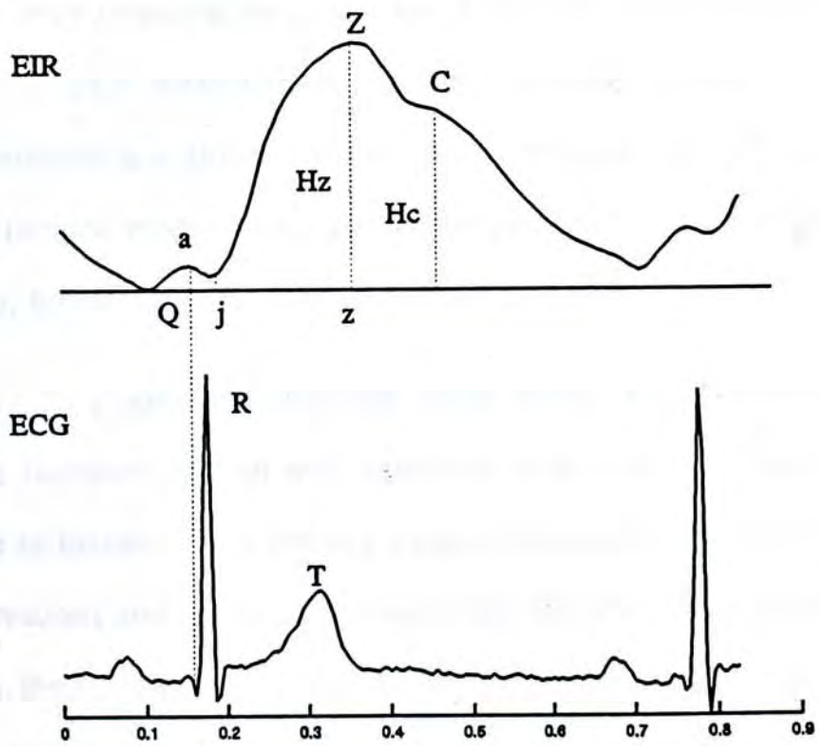

Figure 1.3 The terminology of the EIR and ECG waveforms.

Secondly, with regard to the respiratory artefact, our goal to this problem is to develop a suitable technique which can remove the artefact with the least distortion to the rheopneumographic signal as possible. In addition, such technique should be able to adapt not only to the variations among different subjects but also beat-to-beat variation of cardiac cycles and cycle-to-cycle variation of respiration in view of the time-varying nature of biomedical signal. For such purposes, an adaptive FIR filter based on a Coefficient Lookup Table (CLT) concept is proposed and implemented with the help of short time DFT technique to obtain real time spectral feature of the input signal. If the spectra of the respiratory and rheopneumogram vary and hence the cutoff frequency changes, the filter coefficients need not be re-calculated as they are readily available from the CLT and so fast processing is guaranteed.

Thirdly, the assessment technique for the rheopneumogram is studied. As stated above, the conventional method can not provide enough physical and physiological information about the properties of the circulatory system from the measured signal and sometimes it is difficult to calculate accurately the indices from the waveform because of difficulty in determining the peak positions. In order to assess the properties of the pulmonary circulatory system from a single rheopneumographic measurement, an EIR modeling method is proposed. As the impedance measurement is a global regional effect, therefore, the pulmonary circulation is represented by a lumped model where the model parameters can provide information like vessel compliance, blood inertance, lung peripheral resistance, etc.

And finally, Li proposed a composite wave theory of EIR in the late seventies and suggested that the rheopneumogram was composed of an arterial and a venous components and the waveform so measured was actually a superposition of the two ([LI 83a]). He showed via clinical observations and animal experiments that the wave composite varied alternately and in most cases, the arterial component was more prominent than its venous counterpart but in some specific circumstances such as mitral valve stenosis the reverse might be the case. However a theoretical verification of this hypothesis has never been attempted by any worker in this field. Our study on the composite waves of the EIR signal via a numerical model has

provided a quantitative verification to this hypothesis.

1.5 MAIN CONTRIBUTIONS OF THIS WORK

- Suggesting an optimum electrode configuration for the impedance rheopneumographic measurement.
- Introducing a Coefficient Lookup Table (CLT) concept in adaptive FIR filter design for fast and adaptive biomedical signal processing.
- Presenting an EIR modeling method to estimate the properties of the pulmonary circulatory system.
- Providing a verification to the composite wave theory via computing the composition of the EIR waveform and resolving the EIR waveform into its arterial and venous component waves by modeling method.

1.6 ORGANIZATION OF THE THESIS

Having stated our goal and highlighted the main contribution of the work, we now describe the organization of this thesis. Following this chapter, a background of the notation and terminology of the EBI technique and the EIR signal will first be reviewed at the beginning of chapter 2. The physiological background of the human circulatory systems will also be given in the same chapter.

In chapter 3, an approach to calculate the composition of the EIR signal based on a numerical model and finite element method will be presented. The electrode configuration and the corresponding morphological variations of the rheopneumogram at different electrode positions will also be presented and discussed in this chapter.

The respiratory artefact removal techniques will be presented in chapter 4. We will pay more attention to the techniques dealing with on-line processing and the adaptive features.

A modeling analysis method will be proposed in chapter 5. With the EIR model

developed, some properties of the pulmonary circulatory system can be estimated via the model parameters. The curve fitting and parameter estimation technique will also be presented and discussed.

Chapter 6 describes the animal experiments and clinical observations carried out in Guangxi Medical University and Prince of Walse Hospital. The usefulness of our modeling methods proposed in chapter 3 and chapter 5 will be discussed and verified in this chapter.

And finally, an overall summary of the thesis will be given in chapter 7. The limitation of the approaches proposed in this thesis and topics for further investigations will also be highlighted in that chapter.

CHAPTER 2 PRINCIPLES OF THE EBI TECHNIQUE AND PHYSIOLOGICAL BACKGROUND OF THE RHEOPNEUMOGRAM

In this chapter, the principle and data acquisition system of the electrical impedance rheopneumographic measurement will first be described. Following this a brief introduction to the cardiopulmonary circulation and the physiological background of the EIR signal will be given.

2.1 TISSUE IMPEDANCE AND ORIGINS OF IMPEDANCE CHANGE

2.1.1 IMPEDANCE OF LIVING ORGANS[1]

The unit of living tissue is the single cell, which can be idealized as an electrolyte containing a variety of subcellular structures necessary for metabolism, repair, and reproduction (if the cell exhibits this latter property), enveloped completely by a membrane having a low electrical leakage in the resting state. The passive capacitance values for cell membranes range from 0.001 to 0.12 F/m^2, with a typical value of about 0.01 F/m^2. The resistivity of cytoplasm ranges from 0.1k to 3M Ω-m; 30-40 kΩ-m are typical values for mammalian cells.

Biological tissue consists of an aggregation of cells of differing shapes bonded together and surrounded by tissue fluids that are electrolytes. Therefore, current passing through a specimen of living tissue can pass around the cells by way of the environmental fluid (figure 2.1a) if the current is DC or varies slowly (low frequency). If the frequency is high enough, the reactance of the capacitance of the cell membranes will be small, and current will flow through the cytoplasm as well as the environmental fluid (figure 2.1b). *Therefore, the low-frequency impedance is high and the high-frequency impedance is low, as idealized in figure 2.1c.* The transition from the high to the low value is characteristic for the type of tissue and reflects the capacitive nature of cell membranes. This characteristic feature of living tissue led to the concept of equivalent circuits. The circuit in figure 2.2a is

[1] Introduction in this section is based on the book of Geddes Baker ([GEDD 89]).

frequently used to describe the passive electrical behaviour of biological specimens.

To display the electrical properties of tissue specimens in a more informative manner, Cole employed the impedance-locus method. For the idealized circuit in figure 2.2a, the impedance-locus plot consists of a semicircle of radius $R_m/2$ on the resistance axis with its center located at $R_s+R_m/2$ units from the origin (figure 2.2b). The line joining the origin to a point on the semicircle is the impedance (Z_f) at the frequency f. Increasing the frequency moves the point f in a counterclockwise direction on the semicircle. The angel θ made by the impedance vector with the resistance (horizontal) axis is the phase angle between the voltage and current measured at the terminals of the circuit.

2.1.2 ORIGINS OF IMPEDANCE CHANGE[2]

The basis of the EBI technique as applied to body segments is that any change in the dimension and conductivity in the body segments can be reflected in the detected impedance change. In the human thorax, the possible origins of impedance change include the lungs, the blood vessels, the heart chambers and the blood resistivity.

A. Impedance change with volume

To derive the relationship between the impedance change and volumetric change, a body segment is considered to be a cylindrical conductor of cross-sectional area A_0 and length L, and the electric field through the cross-sectional area is considered uniform (figure 2.3). Then, ignoring reactive elements and inhomogeneities, we have a resistance R_0 which is determined by the resistivity ρ of the medium, or

$$R_0=\rho\frac{L}{A_0}=\rho\frac{L^2}{V_0} \tag{2.1}$$

where $V_0 = A_0L$ is the volume of the segment. The change in R (ΔR) with volumetric change V_1-V_0(ΔV) is then given as

[2] Introduction in this section is based on the review paper of Penney ([PENN 86]).

$$\Delta R=R_1-R_0=\rho L^2(\frac{1}{V_1}-\frac{1}{V_0})=\rho L^2(-\frac{\Delta V}{V_1V_0}) \quad (2.2)$$

Since ΔV is small compared with V_0 and V_1, therefore

$$\Delta R \doteq -\frac{\rho L^2 \Delta V}{V^2} \quad or \quad \Delta R = -\frac{R\Delta V}{V} \quad (2.3)$$

Moreover, with the equation (2.1), it is easy to derive the impedance change with relation to the resistivity change as

$$\Delta R = \frac{\Delta\rho\ L}{A} \quad (2.4)$$

B. Blood-resistivity change with velocity

The conductivity of blood is known to change as blood begins to flow. This observation can be explained by the electrical property and orientation of the red blood cells shown in figure 2.4. At the frequency typically used in impedance plethysmograph (50k to 100kHz), the red blood cells are essentially nonconductors. At rest, Brownian motion keeps their orientation random. Electrical current flowing along a vessel must take a tortuous path around the cells resulting in a low conductivity. Laminar flow produces shear forces which cause the cells to turn parallel to the flow. The electrical current "sees" a smaller nonconductive cross section, resulting in a higher conductivity and an increase in impedance change thereof.

2.2 DATA ACQUISITION SYSTEM (DAS)

2.2.1 IMPEDANCE DETECTOR

To measure the tissue impedance, there are usually two ways, viz applying a known voltage across the object and then measure the current through it or injecting a known current into that object and measure the voltage across it. Both of these methods have been used for various impedance measuring systems. The criterion for selecting a source is that if it can

maintain constant when an unknown contact impedance between the electrode and the patient's tissue exists. This contact impedance can be a factor affecting system accuracy. With consideration about this, a good current source should have high output impedance, while a good voltage source should have low output impedance. This means that while the contact impedance will be negligible for a current source, it will degrade the operation of a voltage source. Likewise, the input impedance of a voltmeter is high, while the input impedance of an ammeter should be near zero. Hence the contact impedance will be much smaller than a voltmeter's input impedance, but will be large compared with an ammeter's input impedance. *This suggests that a system using current injection and voltage measurement would produce the best results with an unknown, varying contact impedance.*

The current injection method does require more complex hardware than a system using voltage application and current measurement. But, because it is more accurate, at present most researchers in the impedance technique use current injection and so is in our study.

In human rheopneumogram recording, alternating current is injected into the body through the surface electrodes. While the current passing through the tissues, any impedance change in tissue will modulate this current resulting in an AM signal. This AM signal is picked up by another pair of surface electrodes (voltage electrodes) and is then demodulated to restore the impedance change signal. This signal is digitized and stored in the computer for further processing and analyzing. Figure 2.5 shows a diagram of the impedance data acquisition system (DAS) which consists of several modules, eg. an oscillator, a constant current source, a voltage detector, an analog to digital converter, a signal processing unit and a computer.

2.2.2 CONSTANT CURRENT SOURCE AND SAFETY CONSIDERATION

In human impedance rheographic recording, the current used must not stimulate or heat the tissue as far as safety and tissue linearity are concerned. Frequencies lower than 20 kHz may stimulate the nerve activities. It is obvious that the minimum risk of stimulation is achieved by using high-frequency alternating current. However, if frequencies above 200 kHz,

measurement becomes difficult in view of the effect of stray wiring capacitance and tissue can no longer be regarded as purely resistive. Therefore, the constant alternate current of 50 kHz and 1 milliampere is used in the impedance measurements.

With the current of low intensity and high frequency to measure physiological events, tissue heating is not a problem. Current in the range of 50 μA at frequencies above 1 kHz and up to a few milliamperes at 100 Khz are typical. Moreover, since the power supply of most current generators used in the impedance measurement is in the range of $\pm$15 V, the voltage drop between the current electrodes can not be out of this range. If the impedance between the current electrodes is larger than the output impedance of the current generator, the current produced can no longer keep in constant. Therefore, it can not result in large voltage drop between the skin and the electrode when any disattachment of the electrode is happened.

Since this project is in cooperation with the Guangxi Medical University (GMU, China), and in order to keep consistency of all the acquired data, the impedance four-electrode systems (Model WSY-4B) manufactured by Luoyang Radio Equipment Factory are used in both CUHK and GMU. In this impedance system, the generated constant AC current is at 50 kHz and 1 mA and the detected AM signal is separated by the four-quadrant multiplier method (Appendix A).

2.2.3 COMPUTER INTERFACE

To digitize the analog impedance signal, an analog to digital converter made by Dataq Instruments is used. This converter has a specification of throughout sampling rate up to 50 kHz, -5 to +5 volt input range, 12 bit digitizing resolution and the most important is ability of waveform scrolling so that one can monitor the waveform on screen in real time.

Since the biomedical signals concerned in our measurements (eg. EBI, ECG, PCG, respiration, etc.) are not of high frequency, a sampling rate of 100 samples-per-second is more than enough for each digitizing channel (the Niquist theorem satisfied). Signal from such equipments are usually in the range of -5 to 5 volt. The 12 bit digitizing resolution can

provide 4096 digitized levels or 2.5 mV resolution for the -5v to 5v input range and this is more than enough.

The signal processing and analyzing unit is designed for noise reduction and elimination (eg., removing respiratory artefact in EIR measurement). These processings can be performed in real time on a PC-486 based DAS for the purpose of on-line monitoring.

In this data acquisition system, not only the impedance signal can be acquired, any other physiological signals (ECG, RIP, PCG, etc.) can also be acquired and monitored simultaneously for the purpose of analysis (as time marker, etc.) and comparison.

2.3 ELECTRODE SYSTEMS[3]

It was found in the measurements that the impedance wave morphology closely related to the electrode placement and the electrode system used, which partly because the human body is not a homogeneous medium so that the current lines in the body can not be constrained in a defined region. Therefore for further analysis, it is very important to acquire the impedance signal of the interested region and eliminate interference of other origins.

2.3.1 TWO-/FOUR-ELECTRODE SYSTEMS

In impedance plethysmographic recordings, there have been two kinds of well known electrode systems called the "two-electrode" and "four-electrode" techniques. In the "two-electrode" techniques, the voltage measured and the current passing between the same two electrodes define the impedance (figure 2.6a). In the "four-electrode" method, separate electrode pairs are used for passing the current and for voltage measurement (figure 2.6b). The ratio of the voltage and current define the "mutual impedance".

Figure 2.6 is a schematic representation of the methodology and the conductivity-change sampling fields of the two impedance plethysmographic techniques. In each part of the figure, the upper left, portion illustrates the technique; the upper right portion is a sketch

[3] The description in this section is based on a review paper of Penney ([PENN 86]).

of the lead field (defined below) associated with the current electrodes; the lower left portion shows the lead field associated with voltage electrodes; and in the lower right portion the dot product between the lead fields is evaluated in selected locations.

2.3.2 GESELOWITZ LEAD FIELD THEORY

In 1971, Geselowitz published an electric field theory derivation which allows prediction of the impedance change caused by a known conductivity change at a specified location ([GESE 71]). An alternate derivation was given by Lehr in 1972 ([LEHR 72]). Stated mathematically, the Geselowitz-Lehr result is

$$\Delta Z = Z(t_1) - Z(t_0) = \int_v -[g(t_1) - g(t_0)][L_a(t_1) \cdot L_b(t_0)]dv \qquad (2.5)$$

where:

$Z(t)$ equals the measured impedance at time t;

$g(t)$ equals the conductivity at every point in space at time t;

$L_a(t_1)$ equals the "lead vector" (defined below) associated with electrode set "a" at time t_1;

$L_b(t_0)$ equals the "lead vector" associated with electrode set "b" at time t_0;

A lead vector is defined as the voltage gradient field produced by unit current passing between a given set of electrodes. With the definitions above, the lower right portion of each part (figure 2.6) can be explained by the equation (2.5). If the dot product is positive (+), a conductivity increase at that place will decrease the measured impedance. Otherwise if the dot product is negative (-), the opposite will occur and where it is zero (0), the conductivity change will not be sensed.

2.3.3 COMPARISONS BETWEEN THE TWO-/FOUR-ELECTRODE SYSTEMS

From the figure 2.6, we can see that the impedance measured with the two-electrode technique consists of several components in series: 1) the lead wires; 2) the polarization impedance between the metal electrode and the electrolyte-rich paste or gel used to couple

with the skin; 3) the skin impedance; 4) the impedance of the remaining tissue.

These components can be conceptually divided into two components termed the "near-field impedance" and the "far-field impedance". The "near-field impedance" is determined by the total current and the voltage drop in the region near an electrode where the current density is higher. The far field impedance is determined by the total current and the voltage drop across the tissue not in the "near-field". The near-field impedance is highly dependent on the size of the electrode used, whereas the far-field impedance depends more on the dimensions and make-up of the body segment being sampled.

The impedance change resulting from the near field will affect heavily the total measurement because of the higher current density in such places. Since only the impedance change resulting from the far field origins is identified as the useful signal, interference resulting from the near field should be eliminated. For this purpose, it is usual to employ a second or receiving pair of electrodes to measure the voltage. Provided the input impedance of the voltmeter is very much higher than the electrode impedance, then the voltage measured, per-unit current through the driving electrodes, is little affected by any of the four electrode impedances (or the skin impedance and fluctuations thereof for that matter).

2.4 HUMAN CARDIOVASCULAR SYSTEM [4]

2.4.1 SYSTEM OPERATION

The cardiovascular system is the main fluid transport system, through which the blood is transported and driven by the heart. Figure 2.7 shows a general sketch of the human cardiovascular system. The heart chambers are indicated, as well as the four valves, which impose unidirectional flow. The four valves of the heart lie in a plane which separates atria and ventricles, named in the direction of flow (indicated by the arrows), tricuspidal-valve (T) and pulmonary-valve (P), and mitral-valve (M) (or bicuspidal) and aortic-valve (A).

[4] Introduction in this section is based on two books ([DINN 81] [MILN 90]).

The circulation of blood in the human body can be separated into two major systems. The pulmonary circulation initiates at the right ventricle and transmits blood only to the lungs, where filtration of CO_2 and supply of fresh oxygen take place. The systemic circulation which initiates at the left ventricle is responsible for the supply of fresh blood to all the organs and tissues of the body, and thus can be considered as the feeding line of all the elements of the body.

The vascular system is regarded as a conducting system with many branches. The diameter of the lumen of the ascending aorta and main pulmonary artery in adult men and women is about 3 cm, giving a cross-section area of 7.1 cm^2. In the systemic circulation, the aorta branches into smaller vessels, the big arteries, which branch again. This prolific branching continues up to the smallest vessels, the capillaries, having normally a inner radius of 4 μm in a quantity of $5x10^9$ in man. With each branching, the total cross-section area increases, so that the area of the cross-section of the capillaries is 600 times the cross-section area of the aorta. Subsequently, after the capillary beds, the inverse occurs: small vessels combine to form the large ones. The blood vessels join from the capillaries to small veins, and keep joining until the number has been reduced to two that finally empty into the right atrium: the vena cava superior and the vena cava inferior.

In the pulmonary circulation as shown in figure 2.8, the main pulmonary artery branches into two main branches. This bifurcation is one of the few places where arterial cross section becomes smaller at a branch point which has a branching coefficient of about 0.8. The branching coefficient is defined as the ratio of the combined areas of the daughter vessels to that of the parent vessel. However, in the next branching, the coefficient increases to 1.08 and at subsequent junctions it gradually increases to 1.20. Similar to its counterpart of the systemic circulation, the branching continues up to capillary beds and then combine to form large pulmonary veins.

Hence in both circulatory systems, arteries are those blood vessels that carry blood from the heart (left and right ventricles) to the capillaries and that from the systemic and

pulmonary arteries system, respectively. The return transportation from the capillaries to the heart, i.e. the left and the right atrium, is provided by the venous system.

2.4.2 PULMONARY HEMODYNAMICS

Blood pressure and vascular resistance are much lower in the pulmonary than in the systemic circulation, and there are corresponding differences in vascular architecture. The large arteries and veins are shorter than their systemic counterparts, and the pulmonary vessels have thinner, more distensible walls containing less elastin and smooth muscle. In order to have a better knowledge of the pulmonary hemodynamics, several importance indices are introduced below.

A. Pressure

The basal mean pulmonary arterial pressure has been found to lie between 10 and 20 mm Hg in a variety of mammals and is not related to body size. Representative values in man are given in table 2.1, along with other relevant hemodynamic variables.

B. Pulmonary blood flow

As the right ventricle ejects blood into the main pulmonary artery, the rate of flow rises to a peak and then falls. Peak flow is slightly lower and more rounded than in the aorta, being proportional to stroke volume. The intermittent systolic ejections of the right ventricle are converted by distention and recoil of the pulmonary artery and its major branches into a pulsatile flow that extends through diastole, as the pulmonary venous flow recorded.

C. Pulmonary vascular resistance

Pulmonary vascular resistance is calculated from the standard resistance equation $R=(P_1-P_2)/Q$, which means that three variable must be measured: pulmonary arterial pressure, left atrial pressure, and pulmonary blood flow (cardiac output). Pulmonary arterial pressure alone is not sufficient, since that pressure may rise as a result of increased cardiac output or elevation of left atrial pressure. Studies of the approximate distribution of pulmonary vascular

resistance within the bed show that the capillaries and venous contribute a larger share than is the case in the systemic circulation.

D. Transmission of pressure and flow pulsations

Pulsations of pressure and flow are transmitted through the pulmonary bed, and the shape of the waves changes because of viscous attenuation and reflections, as in other parts of the circulation. The pulsations of pressure diminish in size as they travel; the pulse that reaches arterioles 100 μm in diameter is only 35 to 55% of the original wave in the main pulmonary artery. Some 25 to 50% of the initial arterial pulse is transmitted to the capillaries of the lung, compared to 5% or less in the systemic bed.

Pressure waves are transmitted all the way to the ends of the pulmonary veins, where their amplitude is 10 to 30% of the main arterial pulsation. Small retrograde waves of pressure and flow caused by the contractions of the left atrium appear in the distal veins, but most of the venous pulsation is transmitted from the right ventricle.

Flow pulsations diminish in amplitude as the move through the pulmonary vascular tree, but not as much as the pressure pulses. This difference is characteristic of a system that contains reflected waves, which augment flow pulsations in regions where they attenuate pressures.

Because of the relatively high distensibility of pulmonary arteries, pulse wave velocity is slower than in the systemic arterial tree. The average value in the main pulmonary artery is 180 cm/sec in man. The time required for waves to travel from the pulmonic valve to the end of the pulmonary veins is 130 to 230 msec in human lungs. Pulse waves move much more rapidly than the blood itself. The average transit time for a drop of blood or injected dye through the human pulmonary circulation is 3 to 7 sec in normal adults at rest.

E. Pulmonary blood volume

The volume of pulmonary vessels is distributed almost equally among arteries,

capillaries, and veins. The capillary bed accounts for some 60 ml/m^2, or 34%, of total pulmonary blood volume, while approximately 30% resides in the arteries and 36% in the veins. A large part of the total volume is thus in the capillary vessels, as might be expected in view of their respiratory function and the relatively short length of the arterial and venous trees.

2.5 PHYSIOLOGICAL BACKGROUND OF EIR WAVEFORM

The EIR waveform is usually analyzed within a cardiac cycle, thus its wave morphology has close relation with the cardiac activities. Each heartbeat, or cardiac cycle, is an intricate sequence of electrical and mechanical events. A comprehensive view of this sequence is given in figure 2.9, where pressure in the various chambers is shown in relation to valve actions and ventricular outflow. The deflections of the electrocardiogram are a useful time reference; the beginning of the *P* wave marks the first excitation of the atria, and the onset of the QRS complex shows the earliest activation of ventricular muscle.

Corresponding to the valve action shown in figure 2.9, a typical composite waveform in one cardiac cycle of the rheopneumogram of the right pulmonary vessels together with its arterial and venous components is shown in Figure 2.10. The composite waveform is characterised by three basic components often referred to as the a-wave, the Z-wave and the C-wave. The a-wave is a small leading wave whose position relation to the Z-wave may vary over a small finite range. The big Z-wave is the principal wave following the a-wave. Its shape may vary from a rather smooth, sinusoidal-looking one to that with a ripple-carrying leading edge and perhaps a somewhat rippling peak. The C-wave is located at the falling edge of Z-wave. It may stand out as a distinct peak or may merge with the Z-wave.

The arterial wave is basically a merged multi-peak wave contribution to the major part of the Z-wave and, to some extent, the C-wave. The leading component is the result of contraction of the right ventricle. Origin of the following peaks or ripples so far have not been truly identified but are strongly believed to be due to the generation of dicrotic wave and late reflections similar to those in the aorta or the setting-up of damped oscillations in the elastic

contraction and expansion of the pulmonary vessels.

The venous components are similar to those of the jugular vein. The a-wave is due to reverse flow as a result of contraction of the left atrium. Following this is another even smaller positive wave which is not always visible and is believed to be due to a small pressure reflux following the closure of the mitral valve. The x-wave in the trailing edge of the a-wave or c-wave has a concave profile and is due to the lowering in pressure as the left atrium relaxes. The V-wave and its long leading edge is the result of pressure build-up due to the inflow of venous blood from the lung in view of the lung-heart pressure differential. The Y-wave in the trailing edge of the VY-wave is due to the opening of the mitral valve which results in a sudden volume expansion and hence a pressure drop as the venous blood empties into the much larger volume of the left ventricle.

2.6 EIR WAVE MORPHOLOGY AND PATHOLOGICAL FACTORS [5]

Any abnormality occurring at the heart or the pulmonary vessels will cause the blood flow in the pulmonary circulation to change and hence resulting in variations in the EIR waveform. Moreover, since the pulmonary capillaries are enclosing the lung for gaseous exchange, lung diseases, such as pulmonary edema and pneumothorax, may also affect the pulmonary blood flow. In the late seventies, Li had observed some forty odd kinds of diseases via the EBI technique. He also showed that the EIR wave morphological variations could in some extent reflect the conditions of the pulmonary circulation and the lungs. According to Li's work, some major factors affecting the EIR wave morphology are given below.

2.6.1 VARIATIONS IN THE a-WAVE

The increase in the a-wave amplitude may be resulted from the following factors: 1) left heart insufficiency; 2) early stage of the mitral valve stenosis; 3) enlargement of the left atrium. In such cases, since there is much blood stored in the veins and the heart, it is easy

[5] Discussions in this section are based on Li, Heilongjiang Scientific & Tech. Press (1982).

for the a-wave to propagate.

However, in some other cases, the reverse may be the case. As the mitral valve stenosis becomes serious, the pressure increases in the venous system resulting in a big resistance for the transmission of a-wave so that the a-wave may be smaller or even disappeared. Moreover, the same phenomenon can be observed for the progressive stiffening of the blood vessels in the aged patient,

2.6.2 VARIATIONS IN THE Z-WAVE

The shape of the leading slope of the Z-wave has close relation with the conditions of the pulmonary trunk and the pulmonary valve. If the valve shows sign of relative stenosis, the Z-wave will result in a very sharp and concave leading edge. Besides, there are many other factors that can affect the morphology of the Z-wave, such cases include deformation of the blood vessels, pulmonary semilunar valve insufficiency, patent ductus arteriosus, primary dilatation of pulmonary artery, etc.

The increase in the Z-wave amplitude may be mainly due to the increase of the right ventricle output while there is no significant increase in the arterial pressure. On the other hand, a decrease of the ventricle output can reduce the Z-wave amplitude, such cases include all kinds of stenosis at the orifice of pulmonary artery, pulmonary artery hypertension, obstructive emphysema, etc.

2.6.3 VARIATIONS IN THE C-WAVE

This wave occurs in the descending slope of the Z-wave, mainly reflecting the blood flow of the pulmonary circulation when the heart is in the diastolic state. It may become significant relative to the Z-wave when blood volume in the venous system increases (eg. the mitral valve stenosis). However, when the vessel compliance is firmly decreased, ripples and other distortion can be observed in this wave. Moreover, in some cases such as the obstructive emphysema and chronic cor-pulmonale, this wave can even disappear resulting from the damage of the veins.

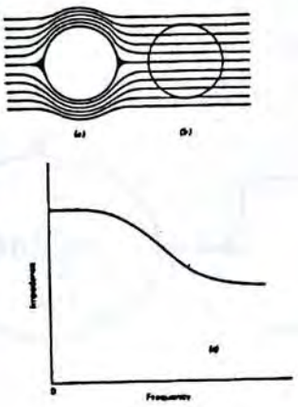

Figure 2.1 Pathways for (a) low-frequency current and (b) high-frequency current for a cell in an electrolyte; (c) the resulting idealized impedance-frequency characteristic. (Redrawn from L.A. Geddes, L.E. Baker, JOHN WILEY, pp560 [DEDD 90])

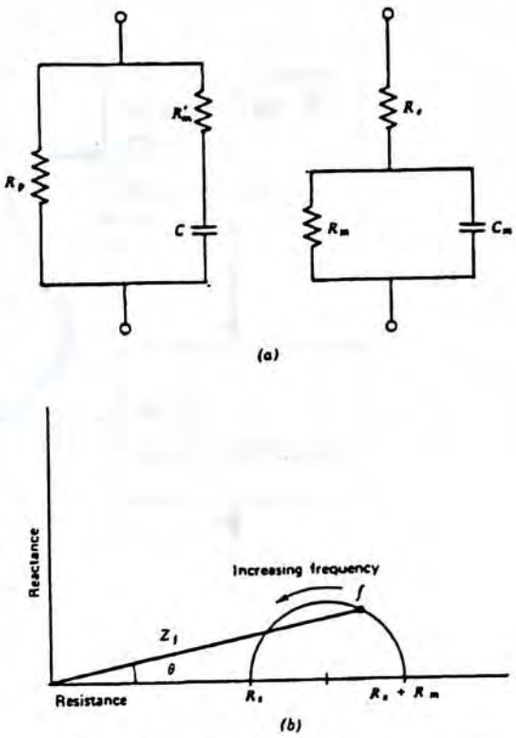

Figure 2.2 (a) Idealized equivalent circuits for living tissue; (b) the impedance-frequency characteristics. Z_f is the impedance at frequency f, and θ is the phase angle. (Redrawn from the same source as fig 2.1)

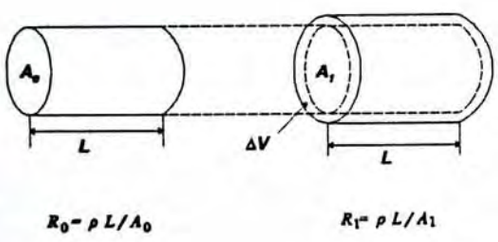

$R_0 = \rho L / A_0$ $R_1 = \rho L / A_1$

Figure 2.3 Volume change of a conducting cylinder.

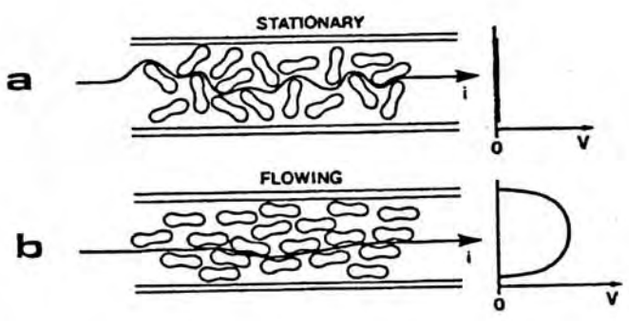

Figure 2.4 Graphic explanation why the conductivity of flowing blood is higher than that of stationary blood in the axial direction. (Redrawn from B.C. Penney, CRC Critical Reviews in Biomed. Eng. Vol 13, 3:pp227-81)

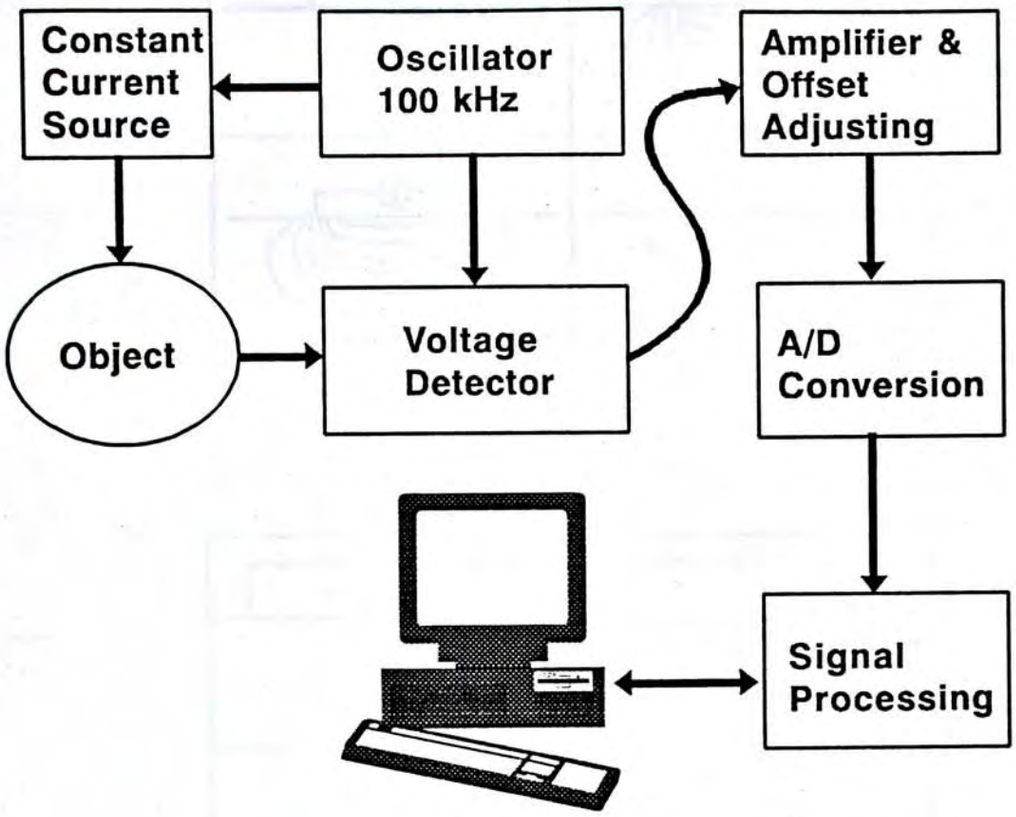

Figure 2.5 A diagram of the EBI data acquisition system.

(a)

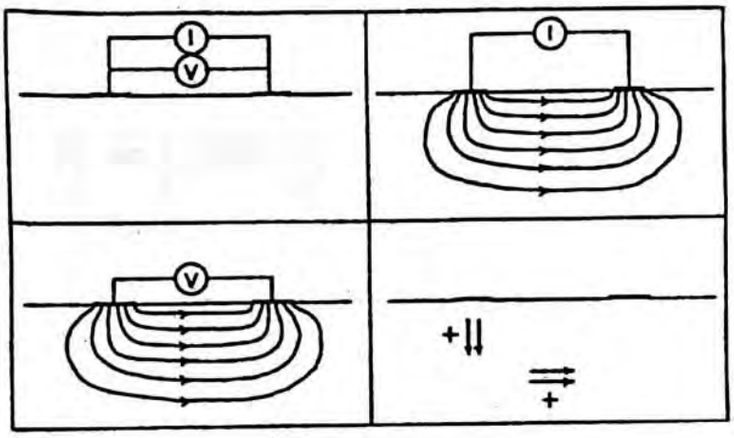

(b)

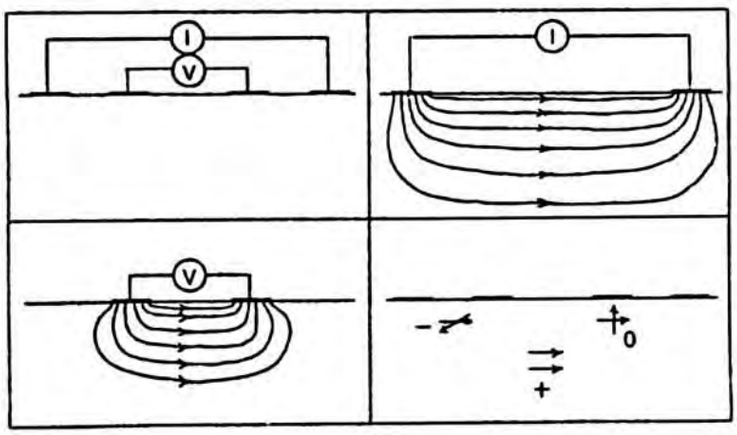

Figure 2.6 Schematic representation of the methodology and the conductivity-change sampling fields of two impedance plethysmographic techniques: (a) the two-electrode; (b) the four-electrode. In each part, the upper left, portion illustrates the technique; the upper right portion is a sketch of the lead field (see text for definition) associated with the current electrodes; the lower left portion shows the lead field associated with voltage electrodes; and in the lower right portion the dot product between the lead fields is evaluated in selected locations. Where the dot product is positive (+), a conductivity increase will decrease the measured impedance. Where it is negative (-), the opposite will occur and where it is zero, the conductivity change will not be sensed. (Redrawn from the same source as fig 2.4)

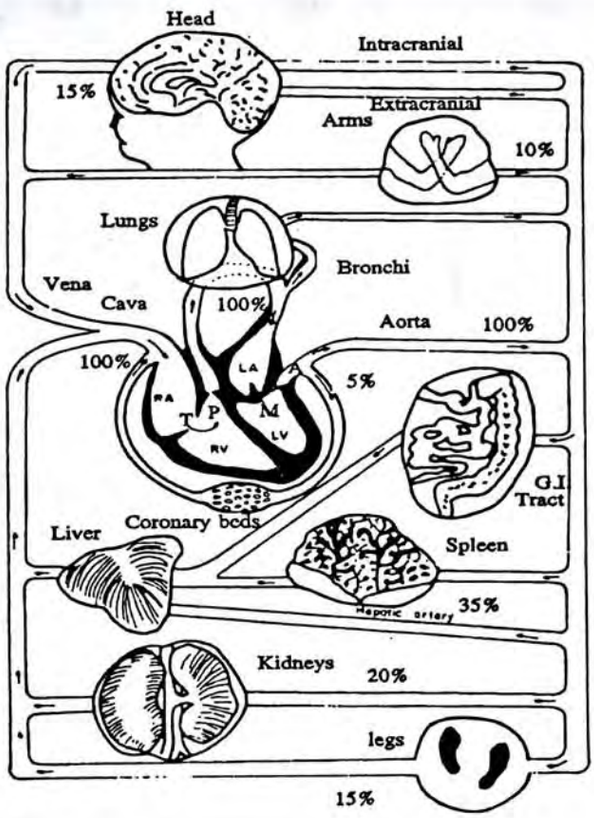

Figure 2.7 Major organs in the circulation system and blood flow distribution. The numbers indicate the approximate percentage of the total flow fed into each of the parallel vascular beds and organs. (Redrawn from U. Dinnar, CRC Press, [DINN 81])

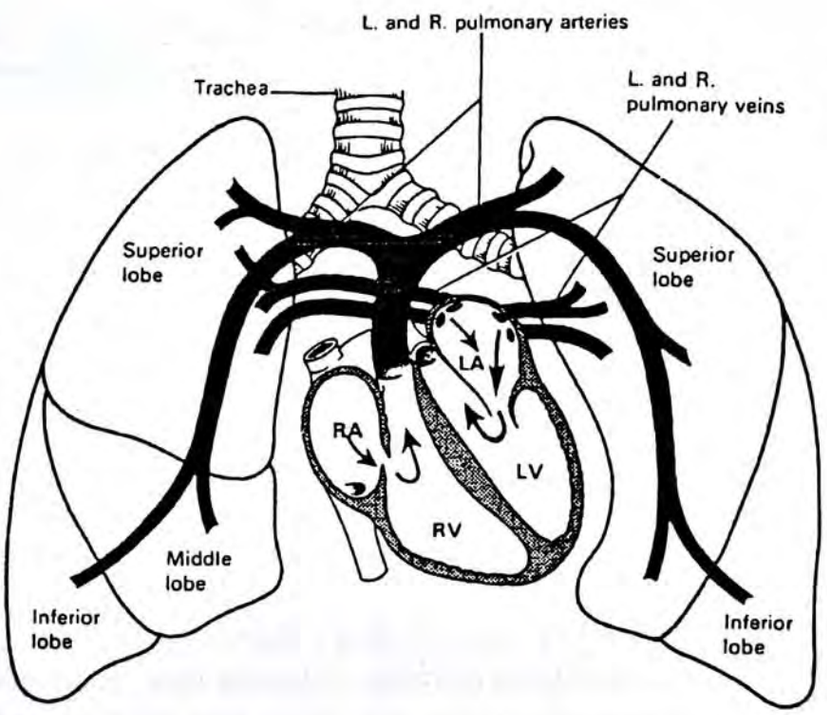

Figure 2.8 Diagram showing the flow of blood between the heart and the lungs. (Redrawn from Ross and Wilson, [ROSS 83])

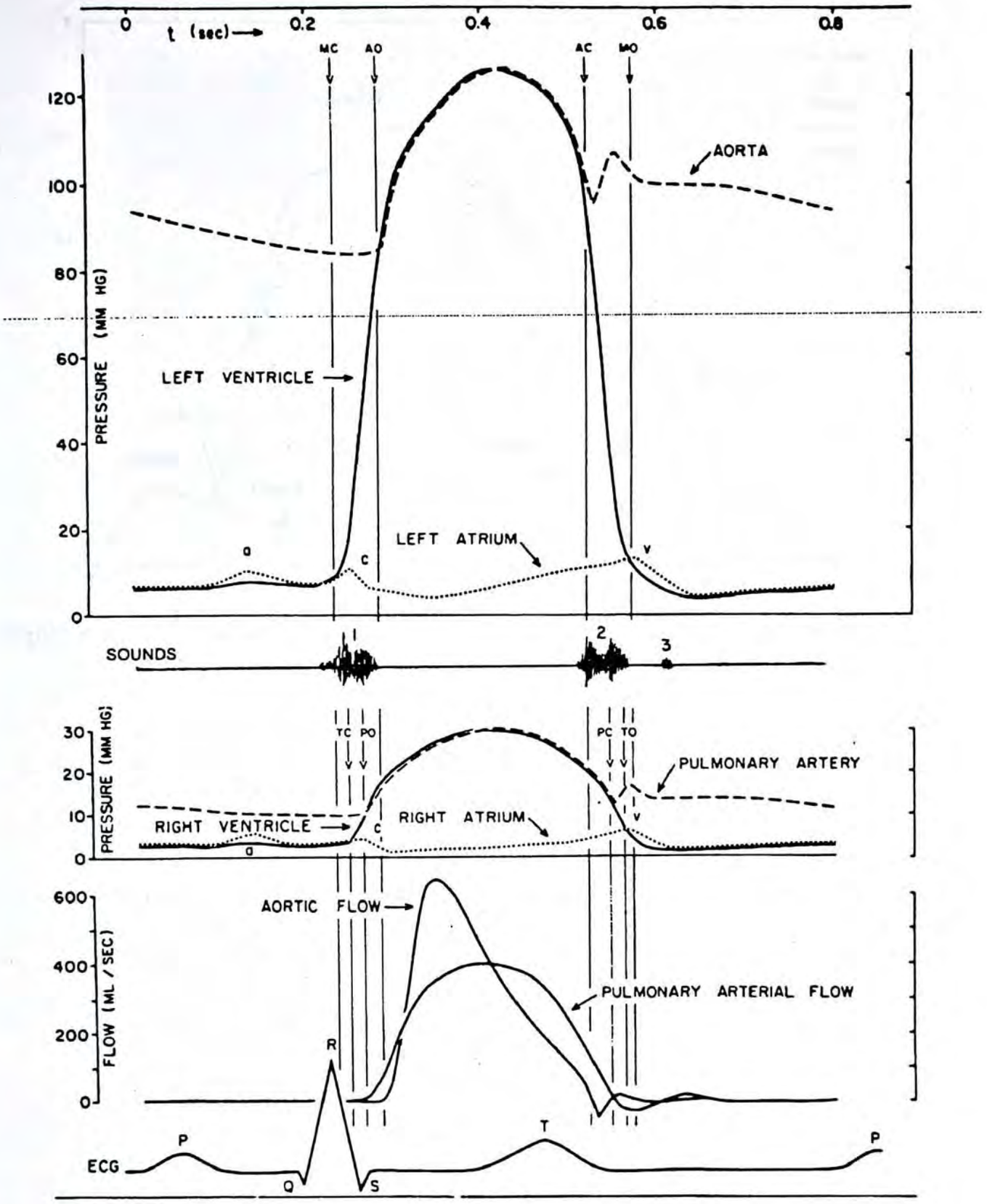

Figure 2.9 Events in cardiac cycle in man. *Top to bottom*; pressure in aorta, left ventricle, and left atrium; heart sounds; pressure in pulmonary artery, right ventricle, and right atrium; blood flow in aorta and pulmonary artery; electrocardiogram. Valve opening and closing indicated by *AO* and *AC*, respectively, for aortic valve; *MO* and *MC* for mitral valve; *PO* an *PC* for pulmonic valve; *TO* and *TC* for tricuspid valve. (Redrawn from W. R. Milnor, Oxford University Press, [MILN 90])

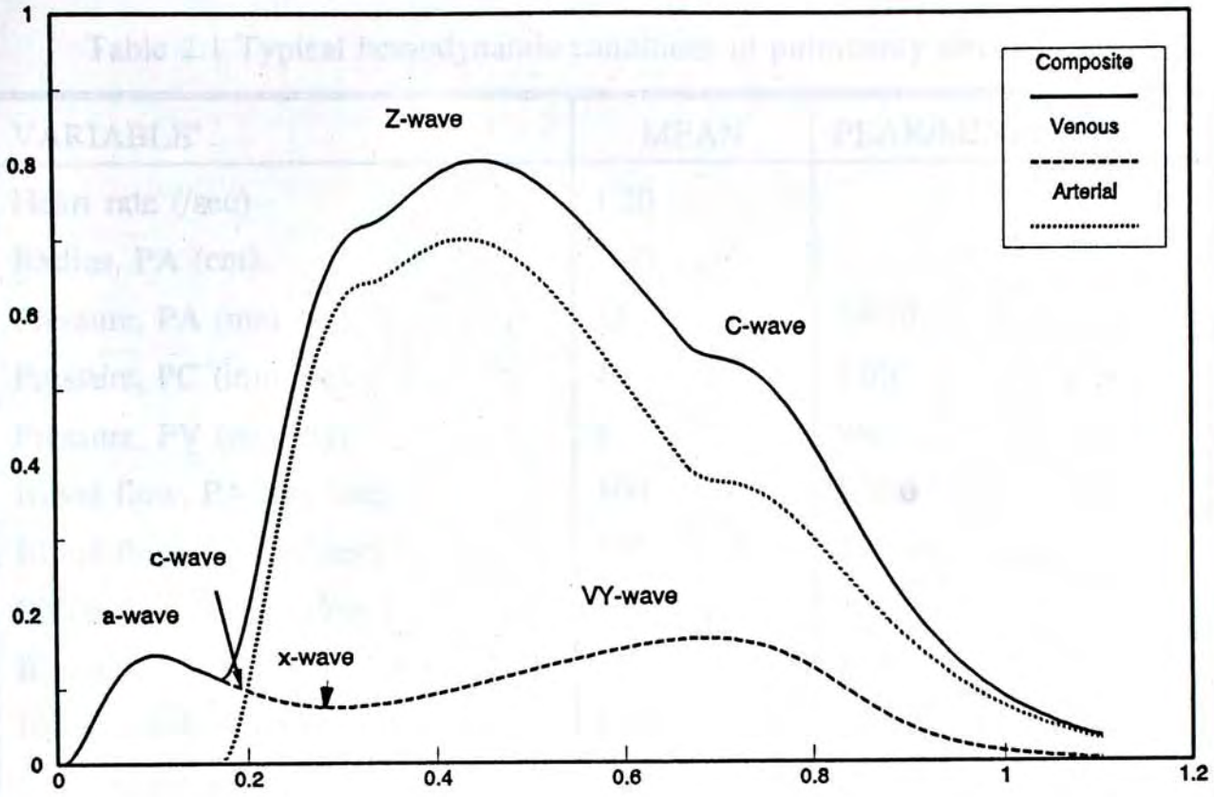

Figure 2.10 A typical rheopneumogram with its arterial and venous components.

Table 2.1 Typical hemodynamic conditions in pulmonary circulation[6]

VARIABLE[a]	MEAN	PEAK/MINIMUM
Heart rate (/sec)	1.20	
Radius, PA (cm)	1.40	
Pressure, PA (mm Hg)	15	24/10
Pressure, PC (mm Hg)	10	12/9
Pressure, PV (mm Hg)	8	9/6
Blood flow, PA (cm^3/sec)	100	500/0
Blood flow PC (cm^3/sec)	100	280/40
Blood flow, PV (cm^3/sec)	100	200/50
Blood velocity, PA (cm/sec)	16	80/0
Blood acceleration (max) (cm/sec^2)	1,010	
Wave velocity (cm/sec)	180	
Pulse transmission time		
PA - PC (sec)	0.120	
PA - PV (sec)	0.180	
Blood volumes		
Arterial (cm^3)	130	
Capillary (cm^3)	150	
Venous (cm^3)	160	
Total (cm^3)	440	

[a] PA, main pulmonary artery; PC, pulmonary capillaries; PV, pulmonary veins at venoatrial junction.

[6] Reprinted from W. R. Milnor, Oxford University Press, 1990 ([MILO 90])

CHAPTER 3 THE COMPOSITION OF IMPEDANCE SIGNAL

In this chapter, a computer simulation scheme via a numerical 2D model of a transthoracic section and the finite element method is proposed to study the composition of the transthoracic impedance signal (TIS) and to find the optimum electrode configuration for the impedance rheopneumographic measurement.

3.1 INTRODUCTION

3.1.1 ORIGINS OF THE TIS

The EBI technique is basically one of indirect extraction of physiological information via impedance measurement of the bio-system. Anything that produces a detectable change in the electrical or physical properties of the tissues in the current path can contribute towards the shaping of the impedance waveform measured. As such, the ability to obtain an impedance signal with sufficiently good signal-to-noise ratio (treating all unwanted sources as noise) is often questionable, partly because the current pathway between the current-injecting electrodes is virtually unknown.

The injected current flows through the extrathoracic and intrathoracic circulations. The former is smaller in extent but closer to the current-injecting electrodes. By applying the four-electrode system, the interference from the extrathoracic circulation can be minimized. Both circulations have pulsatile components; those of the intrathoracic circulation consist of the pulmonary arteries and veins, the vascular bed of the lungs, the unwanted sources for the EIR such as the aorta, the atria, the ventricles and the great veins. The aorta and the short pulmonary artery are deep within the thorax and pulsate with the cardiac activity. The four pulsating, blood-filled chambers of the heart also produce pulsatile impedance changes. The great veins expand and recoil when the heart beats. In summary, the injected current passes through the large vessels, vascular beds and heart chambers, all of which can contribute to a pulsatile impedance change. Moreover, these vessels and chambers carrying blood with a variable (pulsating) velocity also result in impedance changes.

There are many other factors involved that may affect the EIR impedance waveform and these include the respiratory process or any other body movement; extracorporeal factors such as EM coupling; size, configuration, preparation and attachment of electrode and of course instrumentation defects. Depending on the site of interest, some of these interferences can be so significant as to make the measurement result almost useless unless some means are available for their isolation, separation or suppression.

3.1.2 EIR MEASUREMENT AND ELECTRODE POSITION

For impedance rheopneumographic measurement, the electrodes are so positioned as to pick up mainly the pulsation from the right pulmonary arteries and veins. The existing electrode configuration adopted is based mainly on consideration of anatomical location of vessels of interest and convenience. However, the human body is not a homogenous medium. Current paths between injection electrodes, therefore, do not necessarily follow the simple path pattern of a uniform bipolar field. As a result, a purely anatomically based placement scheme can hardly guarantee a resulting signal that is optimised with respect to such interfering sources, particularly those coming from the major components of the systemic circulation for reasons as stated above.

One approach to this problem is to attempt to constrain the field lines to parallel paths with the object so that other origins may not be included. Electrode guarding has been suggested by many researchers as a mean of increasing the sensitivity of an impedance plethysmographic system to resistivity changes in a defined volume. Severinghaus et al proposed a method that surrounded the current injection electrode with a guard electrode held at a potential which minimised the radial potential gradient from the current injection electrode ([SEVE 72]). They claimed that by this means they could constrain current flow to only one lung. However, Plonsey and Collin gave a critique of electrode guarding as applied to impedance plethysmography ([PLON 77]). They concluded that ambiguities could arise since a perturbation of resistivity could give rise to either a positive or negative overall impedance change. These ambiguities arise when the resistivity changes occur close to the

electrodes and particularly in the region between the current drive and the guard electrode.

3.1.3 OPTIMAL EIR MEASUREMENT

As indicated, the impedance rheopneumographic waveform shaping depends on the electrode system which includes the electrode type, size and placement. Experimental determination of an optimal electrode configuration with respect to minimal systemic interference is difficult if not impossible. On the other hand, computer simulation, even on a somewhat simplified basis, can provide an insight of the situation and may even be possible to suggest the adoption of such an optimal electrode configuration. The advantage of trying out a computer simulation approach is obvious. Firstly, the anatomical layout can be simplified to whatever extent in the process, bearing in mind not to ignore major contributing factors. Secondly by considering small excitations to begin with, the entire system for simulation may be regarded as linear so that the method of superposition may be applied.

By analyzing the current density and potential distribution for a given configuration of current and potential electrodes and a numerical tissue conductivity distribution within the model, the impedance and hence its time-variation between any two potential electrodes can be obtained. Moreover, the potential difference between any two points on the periphery can be obtained as a function of the global or local tissue conductivity changes (normally as a result of temporal volumetric variations). In particular, an electrode configuration can be estimated from the simulation study such that the potential difference across the voltage electrode pair is the least possible as a result of the systemic (including the left ventricle) variations, but still sizable as far as response to origins of interest is concerned which in this case are the relevant parts of the pulmonary circulation.

A few studies had been carried out in the past using 2-D or 3-D numerical models to estimate the effect of electrode configurations and the origins of the impedance signal. Kim et al ([KIM 86] [KIM 88]) and Patterson ([PATT 85]) studied the origins of the impedance cardiography with 3D models of the thorax. Their results showed that the aorta expansion was the most significant contributor to the impedance signal. A few attempts had also been made

with 2D models by Bhattacharya ([BHAT 88]). However, they all ignored the possible interference between the two circulatory systems and concentrated only on the optimal acquisition of the cardiographic signal.

In this study, much attention has been paid to study the problem of wave morphological variation with different electrode configurations with a view to find an optimum configuration for impedance rheopneumographic measurement so as to obtain a "pure" rheopneumographic signal with as little interference as possible. A 2D numerical model of the human thoracic cross section was developed with 4882 eight-node trilinear cubic elements and 7073 nodes. The electrical potential distribution resulting from the current injection at the body surface was calculated via the finite element method (FEM).

In this chapter, we will first give an illustration to show the current path within the inhomogeneous medium between the current electrodes. Then descriptions of how to build a 2D numerical model of transthoracic section and how to calculate the internal potential and current density distributions are given. Finally, results of computer simulations and experiments will be presented and discussed.

3.2 CURRENT PATH IN AN INHOMOGENEOUS MEDIUM [1]

An appreciation of the sources of impedance changes accompanied by physiological activity and the requirements for recording these changes can be obtained by considering the measurement of the resistivity of biological materials in a rectangular conductivity cell, illustrated in two dimension in Figure. 3.1. In this cell, the material to be measured is constrained on four sides by a perfect insulator and contacted uniformly by end-plate electrodes, *C, D* (ideally perfect conductors). If the material is isotropic, the constant current, i_k, will be conducted in rectangular "tubes" of equal dimensions, and the current density will be the same everywhere.

But if inserting a conductor or an insulator into the material, the current path and

[1]Discussions in this section are based on the studies of Baker ([BAKE 89]).

potential distribution can be modified as illustrated in Figures 3.2 and 3.3.

If instead of contacting the material to be measured by large end-plate electrodes, small area electrodes are used, the current density becomes nonuniform as shown in Figure 3.4. In this situation, the potential gradient within the material and that measured along the surface of the cell will not be uniform. The value of resistance measured will not be easily related to the geometry of the material, and changes in resistivity introduced within the material will have a much greater effect on current and voltage relationships if placed in the regions of high current density, i.e., near the small electrodes.

3.3 NUMERICAL MODEL

3.3.1 2D MODEL

A cross section of the human thorax is selected for study ([ELLI 91]). This section lies at the level of the intervertebral disc between the sixth and seventh thoracic vertebrae and passes through the body of the sternum at the level of the 3th costal cartilage. Pulmonary arteries, aorta, and the superior vena cava can be seen in this section. These organs along with the lung tissue are identified as the major origins of the impedance rheopneumogram. The use of a 2D model is justified as a first approximation, because around the plane through the centres of the electrodes, the geometry of thorax is sufficiently uniform along the vertical axis for about 3cm.

While using this cross section to study the electrical potential distribution, a few structural simplifications have been made. First, the intricately interwoven structure of muscles and adipose tissues is replaced by a single homogeneous material. Second, the regions corresponding to the oesophagus are replaced by surrounding tissues and the pericardial sac has been removed. These assumptions are justified because only those having variations in dimension, conductivity or dielectric are concerned. Figure 3.5 shows the simplified model, in which the possible origins of impedance change include the pulmonary arteries, the aorta and the superior vena cava.

3.3.2 TISSUE RESISTIVITY

Precise assignment of tissue resistivity is difficult as they are not constant but depend on physiological events and subjects. There are many reported values on the electrical resistivity of biological material. An excellent, though rather old, review was given by Geddes and Baker ([GEDD 67]). After many years, Stuchly gave a more recent review ([STUC 84]). There are many discrepancies in the reported values but this is not surprising in view of the great difficulties in making *in vivo* measurements and the problems of preserving tissue for *in vitro* measurement.

Fairly reliable values exist for the resistivity of blood. Burger and van Donger ([BURG 61]) give a value of 1.55 Ωm. Brown quotes a range of 1.48-1.76 Ωm ([BROW 83b]). The relationship between haematocrit and resistivity is well established. The change in resistivity is from approximately 1.1 Ωm to 1.6 Ωm as the haematocrit is increased from 40 to 60 percents ([SHIM 81]). However, some caution is needed in utilising this relationship as there is also a well described increase in the resistivity of flowing blood with blood velocity. This change is of the order of 15 percent.

The average resistivity of the lungs depends on the extent of inflation and blood perfusion and many conflicting values have been reported in the past. In this study, a value of 12.0 Ωm adopted by Kim is used ([KIM 88]).

some assumptions have been made for the sake of simplification: 1) except for the blood, the tissues are isotropic; 2) tissues are essentially resistive at the operating frequency (i.e., 50-100 kHz). The displacement effect at this frequency is usually negligible (see chapter 2); 3) the resistivity variations of the tissues are simplified to take on either "systolic" or "diastolic" values only as shown in Table 3.1.

Table 3.1 The tissue resistivities (Ωm)

Tissue	Diastole	Systole
Skin	3	3
Tissue, adipose	5.99	5.99
Lung	12.0	11.0
Heart muscle	3.75	3.75
Blood	1.48	1.25
Spinal Cord	18.0	18.0
Bone	20.0	20.0

3.4 CALCULATION OF THE POTENTIAL DISTRIBUTION

In order to determine what sources are included in the impedance waveform and how the waveform is affected by each source, the current and potential density distributions in the body resulting from the current injection from the body surface electrodes are analyzed. With the current density distribution, the optimum current electrode configuration can be selected for which the internal area of the pulmonary artery should have a higher density so that the resistivity change in this area can produce larger impedance change on the body surface. Whereas with the potential distribution along the body surface, the optimum voltage electrode configuration can be obtained for which the impedance change due to the pulmonary artery should be picked up with less interference of other sources.

The following assumptions were made to simplify the computation: 1) the thorax is a source-free region, and 2) Current flux normal to the body surface is zero except under the electrodes. Under these assumptions, the field through which steady current flowing between the current electrodes is governed by the Laplace equation (in two dimension)

$$\frac{\partial}{\partial x}(\sigma_x \frac{\partial u}{\partial x}) + \frac{\partial}{\partial y}(\sigma_y \frac{\partial u}{\partial y}) = 0 \tag{3.1}$$

where u is potential and σ_x and σ_y are conductivities of the material in the x and y directions respectively. Although in practice alternating current is used rather than steady current, the assumption of steady current is reasonable in low frequencies (below 100 kHz) so that a quasi-static condition holds. With the above assumptions, the field is subject to Dirichlet and Neumann boundary conditions, which indicate that all points of the body surface in contact with an electrode have the same potential as the electrode and at all other surface points, the potential gradient normal to the surface is zero.

The Laplace equations are solved by finite element method ([HUGH 87] [ZIEN 89]), where the conductivity distribution being studied is divided into a set of discrete elements. Homogeneity is assumed within each element and the flow of current between element is described by discrete representations of equation 3.1.

It is well known from energy related arguments that satisfying the differential equations being solved in a region having Dirichlet and Neumann boundary conditions is equivalent to minimizing a functional that gives the total energy of the region of interest. Using the following functional

$$L = \int_{\Omega}\int \left[\frac{1}{2} \vec{\nabla} u \cdot \vec{\nabla} u \right] d\Omega \tag{3.2}$$

where Ω is the 2D domain of interest, the process of searching for the value of u that minimises the above functional was carried via the following method.

The functional can be expressed as $L=\Sigma L_e$, in which the trial function $\tilde{u}_e(x, y)$ for each element can be constructed as

$$\tilde{u}_e(x, y) = N(x, y)u_e \tag{3.3}$$

in which $N(x, y)$ is the approximate shape function which is dependent on the type of element

used and u_e is the vector containing the unknown value of the function at the nodes. Substituting $\tilde{u}_e(x, y)$ in L_e and minimizing with respect to u_e, viz

$$\frac{\partial L_e}{\partial u_e}=0 \tag{3.4}$$

yields $k_e u_e+f_e=0$, which is known as the element-matrix equations. The assembly of this equation in accordance with the summation results in $KU+F=0$, which is the complete-matrix equation for the entire domain. Here we can see that the another reason for using FEM is because it is easier to construct an admissible approximate function $\tilde{u}_e(x, y)$ in equation (3.3) for each type of geometrically well-defined element than for the entire domain.

3.5 RESULTS

3.5.1 COMPUTER SIMULATIONS

In the study, computer simulations were performed on a workstation (DEC 5200) via a FEM software of EMRC ([EMRC 91a] [EMRC 91b], [Appendix B]). Figures 3.6 and 3.7 show the typical calculated current density and potential distributions when the heart is in the state of diastole. As can be observed, the current densities are very high at positions of the current injecting electrodes. There are several other peaks of the current density in the inner regions where lie the right pulmonary artery, the aorta and the superior vena cava. Higher current density in a region means that bigger impedance change can be resulted from any change of resistivity or volume within that region.

The basal impedance between the injecting current electrodes can be calculated from

$$Z_0(i, j)=\frac{(u_i-u_j)}{I_0} \tag{3.5}$$

where u_i, u_j are potentials at positions i and j, and I_0 is the amplitude of injected current. With the electrode configuration as shown in figure 3.5 and the potential distribution shown in figure 3.7, the base impedance is about 4.2 kΩ in this case.

The "mutual" impedance change between the voltage pick-up electrodes resulting from diastole to systole of the heart is defined to be

$$\Delta Z(m, n) = \frac{(\Delta u_m - \Delta u_n)}{I_0} \tag{3.6}$$

where Δu_m and Δu_n are the differential potentials between the ends of diastolic and systolic states at positions m and n respectively.

While simulating the cardiac activity from the diastolic state to the systole state, the sizes of big blood vessels are increased 5 percent ([GEDD 89]), and the resistivities of blood and lung are also changed accordingly (table 3.1) within the model. In order to calculate the contribution of each possible origin, all origins are controlled to change together or individually so that their contributions to the TIS can be estimated.

The response due to activity of the right pulmonary circulation only is of interest in the rheopneumographic measurement. That due to other sources including the left pulmonary circulation is regarded as interference component. Thus separate impedance changes resulting jointly from the right lung and right pulmonary artery and jointly from the left lung, the heart and the aorta are calculated. As can be seen in equation (3.6), the value of impedance change $\Delta Z(m, n)$ depends on both the current and voltage electrode positions. Therefore, suitable selection of the electrode configuration is very important in picking up "pure" rheop-neumographic signal.

A ratio *RPTRC* is defined as the composite ratio of the Right Pulmonary circuit response $\Delta Z(m, n)|_{RP}$ to the Remaining Circulatory system response $\Delta Z(m, n)|_{RC}$. The latter is approximated by considering the left lung and aorta expansion only in view of the minimal contributions from the cardiac and left pulmonary expansions at this level. Therefore, at the pick-up positions m and n, we have the RPTRC value defined as

$$RPTRC(m, n)=\Delta Z(m, n)|_{RP} : \Delta Z(m, n)|_{RC} \quad (3.7)$$

With the above definitions, we have done several simulations to find the optimum electrode configuration and electrode size, the effect of blood resistivity change, etc.

(1) Optimal Electrode Configuration

Through analyzing the differential potential distribution along the model border, one can calculate the contribution (the mutual impedance change) of each origin and hence determine the optimum electrode configuration with which the rheopneumogram can be measured with the least interference from the remaining circulatory system.

Figures 3.8 and 3.9 show the differential potential distributions between the diastolic and systolic states, resulting from the right pulmonary circuit and the remaining circulatory system respectively when the current electrodes are placed at position No. 17 and 85. For the conventional electrode configuration, the voltage electrodes are usually placed at position No. 15 and 82 as shown in figure 3.5, and the ratio *RPTRC*(15, 82) is 120Ω:45Ω indicating that the interference from the aorta and left lung is quite substantial. However, if the voltage electrodes are placed at position No. 65 and 82 (eg., the two electrode are place on the equal potential line), the *RPTRC*(65, 82) increases to 50Ω:0Ω. Although the contribution from both of the right pulmonary artery and right lung decreases, but the interference from both of the left lung and aorta can be more or less ignored.

(2) Effect Of Electrode Size

The effect of electrode size has likewise been studied. Figures 3.10 and 3.11 show the differential potential distributions resulting from the two different group activities with electrode size six times larger than that of conventional size used (eg., Ag-AgCl snap electrode and 1 cm diameter). Results show that the *RPTRC*(65, 82) value increases to about 60Ω:0Ω for the optimum electrode configuration. Still larger electrode size, besides introducing problems such as electrode attachment, does not give better result. In fact the

RPTRC(65, 82) value begins to reduce (eg., reducing to 50Ω:0Ω) when the electrode size is 10 times larger than its conventional size.

Figure 3.12 shows the histograms of *RPTRC* values vs electrode size for both the conventional and optimum configurations. There is no significant variation in *RPTRC* value for the conventional configuration but for the optimum configuration there shows a slight variation. The optimal size is about four to eight times of the existing size (eg. 4-8 cm diameter) which has a *RPTRC*(65, 82) value of about 60Ω:0Ω for the optimum configuration.

(3) Impedance Change Resulting From All Origins

The total effect resulting from all the two group activities together has also been calculated and the differential potential distribution is shown in figure 3.13. Comparing this figure with figure 3.14, which is the sum of figures 3.8 and 3.9 resulting from the two group activities acting separately, there is about 10 percent difference between the two results. The reason of this difference may lie in that the tissue is not quite linear even for the small perturbation considered and all origins are not geometric point sources so that the superposition theorem can not be applied without expecting appreciable distortion or inaccuracy.

(4) Effect Of Blood Resistivity Change

Besides the volumetric change, the tissue resistivity change can also result in the impedance change. As introduced in chapter 2, we know that the blood resistivity changes with its velocity, eg., from 1.48 Ωm at diastole to 1.25 Ωm at systole. In order to estimate the contribution due to this resistivity change, the differential potential distribution has been calculated as shown in figure 3.15. The impedance change $\Delta Z(15, 82)$ so obtained is 13Ω for the conventional configuration and 8Ω ($\Delta Z(65, 82)$) for the optimum configuration. These results indicate that the contribution due to blood resistivity change during systole is less than 10 percent of the total impedance change with the conventional configuration ($\Delta Z(15, 82)$=140Ω, see figure 3.13) and less than 20% of the total impedance change with the

optimum configuration ($\Delta Z(65, 82)$=35Ω, also see figure 3.13).

3.5.2 EXPERIMENTAL RESULTS

For the purpose of verifying the results of computer simulations, several experiments were carried out and their results were compared with those of computer simulations. These experiments include:

(1) Comparing the impedance waveforms measured with the optimum electrode configration (eg., with the best RPTRC value at position No. 65 and 82 involving the least interference from other origins) and with the worst electrode configuration (eg., with the worst RPTRC value at position No. 28 and 65 involving the largest interference from the other origins);

(2) Studying the variation of impedance waveforms measured at different places along the thoracic surface.

Figure 3.17 shows the impedance waveforms measured at the optimum and worst RPTRC positions. The significant morphological variation between these two waveforms may be due to the different contributions from both of the pulmonary and systemic circulations. In view of the blood flow speed difference between the two circulatory systems (blood flowing faster in the systemic circulation than in the pulmonary circulation), the time lag of the ascending edge of Z-wave measured at the optimum configuration is a significant indication of involving less systemic component.

Impedance waveforms measured along the thoracic surface at position labels P0 and P1, P0 and P2, ..., P0 and P13 (see figure 3.13 for the electrode positions) are shown in figure 3.19. The significant wave morphological variation is of course due to the different contributions from the pulmonary and systemic circulations.

The amplitude response of the Z-waves and that calculated from the total effect (eg., calculated from the differential potential distribution shown in figure 3.13) are plotted in

figure 3.18. The two amplitude responses match quite well with a correlation coefficient of 0.9251, providing a verification to the computer simulations therefrom.

3.6 DISCUSSIONS

In this study, the computer simulations were carried out on a transthoracic section with a simplified 2D numerical model. Several assumptions and apprximations have been made. These include, 1) using the 2D model and ignoring effect of other layers, such as the contribution from the heart chambers; 2) in finding the optimum electrode configuration, the optimal current electrode positions were assumed to be at the convention ones; 3) ignoring the resistivity variation of the lung due to different respiratory states; 4) not considering anatomical difference among differnet subjects. In order to investigate how these may inflence the accuracy of results obtained, we have performed several computer simulations.

(1) Effect Of Volumetric Change In Heart Chambers

In order to observe the effect of impedance change resulting from the volumetric change of the heart chambers during the heart systole, computer simulations have been carried out in another 2D section of the thorax which lies at the level of the intervertebral disc between the seventh and eighth thoracic vertebrae and passes through the body of the sternum at the level of the fourth costal cartilage. All of the four cardiac chambers can be seen in this section. Figure 3.16 shows the 2D model of this section along with the electrode positions. When the heart is in the state of end systole, the volumes of heart chambers are reduced about 30 percent and the sizes of big blood vessels increased 5 percent of their values in the diastolic state ([GEDD 89]). The simulated results are shown in table 3.2 which indicates that the heart chamber contractions produce a negative impedance change and the contribution to the total impedance change is about 30 percent.

Table 3.2 Impedance changes simulated at transthoracic section (T7-T8)

Events	$\Delta Z(V_1, V_2)$ (Ω)
Lung & Pulmonary artery	120
Aorta	15
Heart Chambers	-35
Total Effect	100

(2) The Optimum Current ELectrode Positions

In the last section, all computer simulations were carried out with the current electrodes fixed at position No. 17 and 85 which is the conventional current electrode position. However, the optimum current electrode position should be so determined to make the current densities higher in the region of right pulmonary artery and lower in other regions. In order to search the optimal current electrode position, a simulation was carried out, in which one current electrode was fixed at position 85, another moved around position 17. Figure 3.20 shows the current densities at the places of the possible origins vs the current electrode position. The optimal current electrode position may be at position No. 14 and 85. With such a placement, the current density of the right pulmonary artery is the highest in either absolute value or comparative value respective to those of other origins.

(3) Effect Of Respiration

Moreover, as mentioned in section 3.3.1, it is difficult to assign a resistivity value for the lungs because of the extent of inflation and blood perfusion. To investigate how the resistivity variation of the lung can affect the simulation result, a simulation was performed in which the resistivity of the lung increased 10 times simulating more air filled into the lungs. Results of impedance change resulting from the right pulmonary circuit and remaining circulatory system are shown in figures 3.21 and 3.22 respectively. The *RPTRC* value changes to 90Ω:200Ω for the conventional configuration and 30Ω:0Ω for the optimum configuration.

The right pulmonary components are decreased in both configurations. However, it is interesting that the component of remaining circulatory system increases significantly only for the conventional configuration. This shows good agreements with the apneic measurements at deep inspiration and deep expiration as shown in figure 5.21, which indicates an increase of the systemic component at deep inspiration in view of the morphological variation and time lead of the ascending edge of the Z-wave.

(4) Sensitivity Of The ELectrode Positioning

An optimum electrode configuration (eg., at position No. 65 and 82 on the equal potential line) was suggested in previous section. With this configuration, the interference from other origins can be the least. A problem arises that if the electrodes can not be placed precisely on the equal potential line as shown in figure 3.9, how large the interference will be resulted from the other origins? In figure 3.9, it shows if the electrode position displaces 1 unit from the optimum position, about 1Ω of impedance difference will be resulted in.

(5) Effect Of Anatamic Difference

In view of the anatomic difference exsisting in different subjects, a simulation was carried out to estimate the sensitivity of the potential distribution aganist to the anatomicl variation. Figure 3.23 shows a sketch of the 2D model with a position variation of the asending aorta. The resulted potential distribution difference between the original and anatomically changed is calculated and shown in figure 3.24. The potential distribution shows no significantly variation along the model border, indicating a very low sensitivity.

3.7 CONCLUSION

In this chapter, a computer simulation scheme has been presented for the purpose of finding optimum electrode configuration for the electrical impedance rheopneumographic measurement. An optimum electrode configuration has been suggested. Results of computer simulations and subsequent measurements indicate reasonably good agreements. The study also points to the fact that for impedance technique of this kind, ignorance of the possible

contribution of other (unintentional) sources can be a matter of concerned and in the worst case can introduce error in interpretation and hence the subsequent clinical diagnosis. In particular, for the conventional electrode configuration presently adopted in China, the measured EIR waveform is very likely to include substantial contributions from sources other than the relevant part of the pulmonary circulation.

3.8 NOTES ON PUBLICATIONS

A paper entitled "Search of optimal electrode configuration for impedance rheopneumographic measurements by finite element method" was presented at CMBES'93, Canada. Another paper entitled "Analysis of electrical field in the human thorax via a numerical model and finite element method" has been accepted and will be presented in FECMBE'93, Beijing. All these papers were jointly authored with Thomas T. C. Choy.

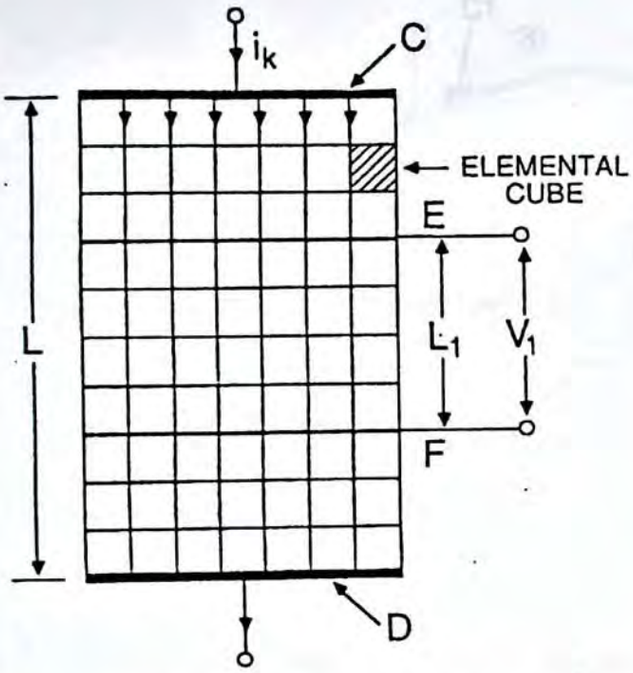

Figure 3.1 Current and potential distribution in an isotropic material cell. (figures 3.1 to 3.4 are redrawn from L E Baker, [BAKE 89])

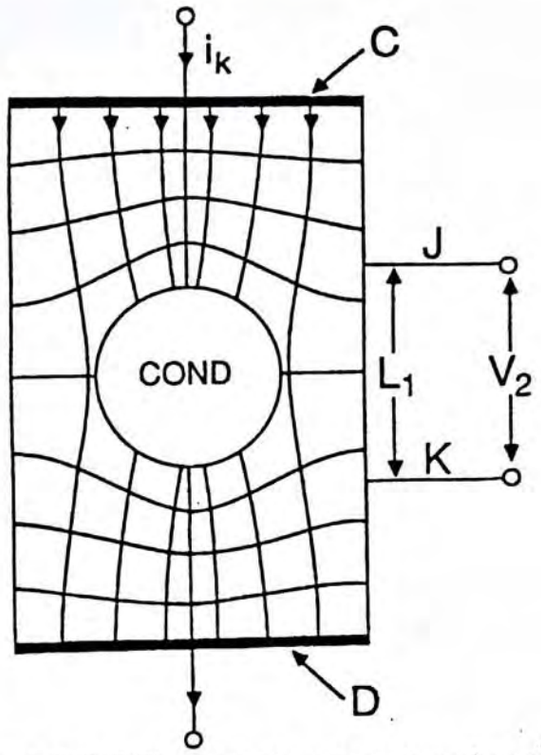

Figure 3.2 Effect on the current and potential distribution of inserting a sphere of high conductivity into the conductivity cell

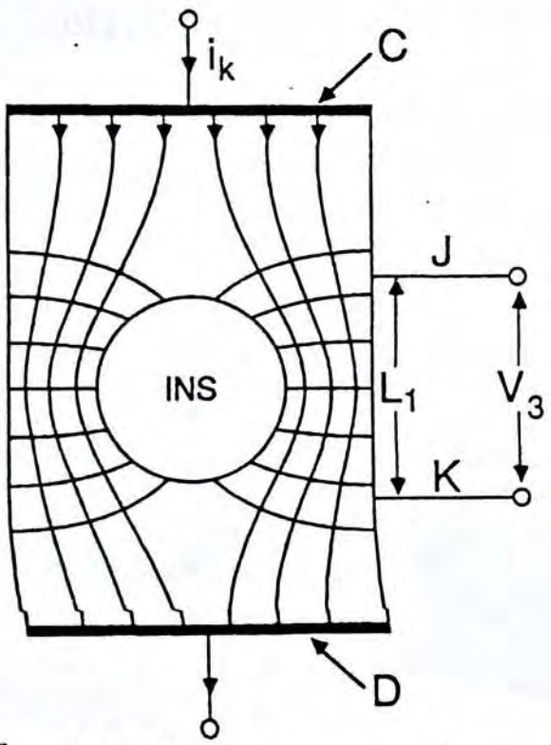

Figure 3.3 Effect on current and potential distribution of inserting a sphere of low conductivity into the conductivity cell

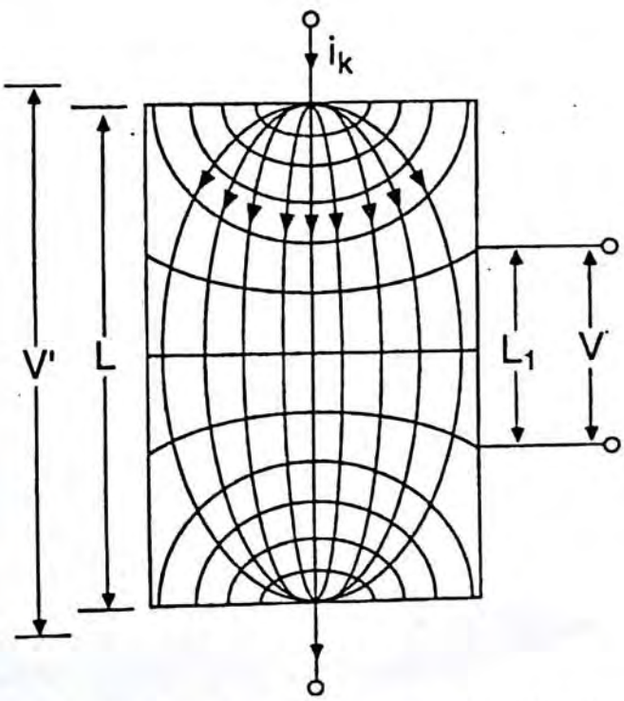

Figure 3.4 Current and potential distribution if the current is injected into the cell using small electrodes.

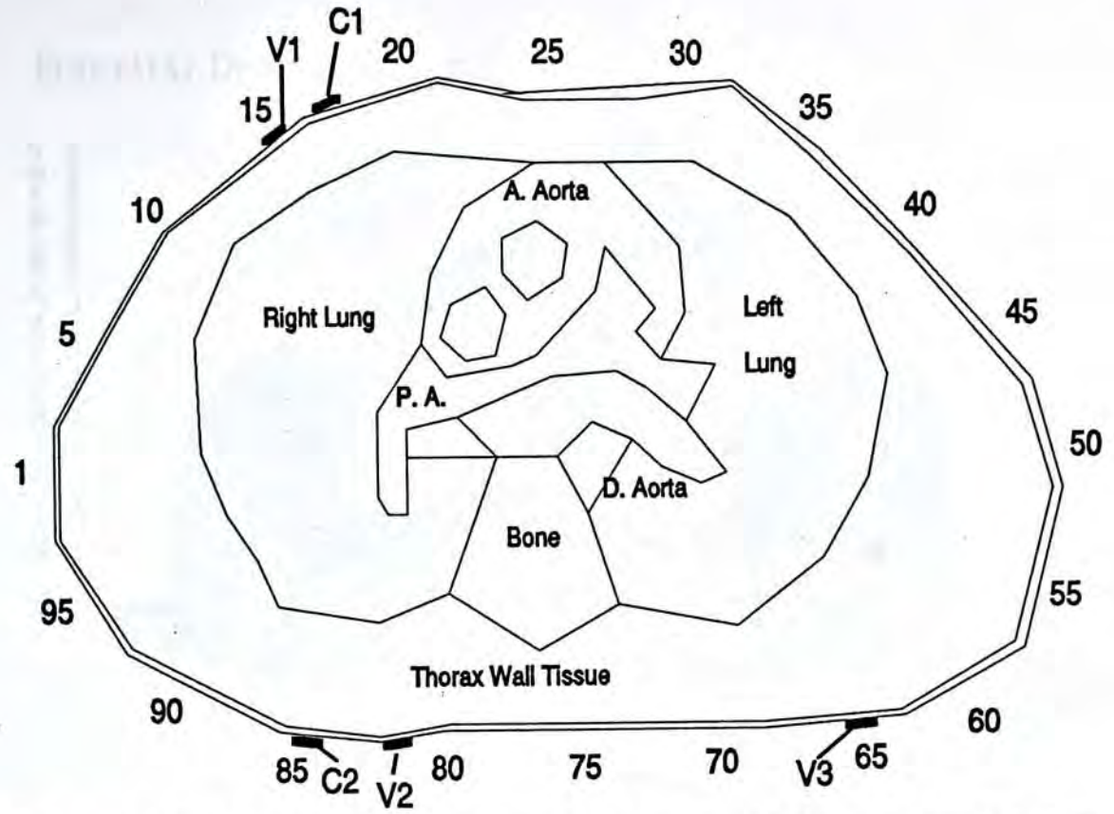

Figure 3.5 A simplified model of the thoracic cross section at the position T6 along with position labels from 1 to 100 and electrode positions.

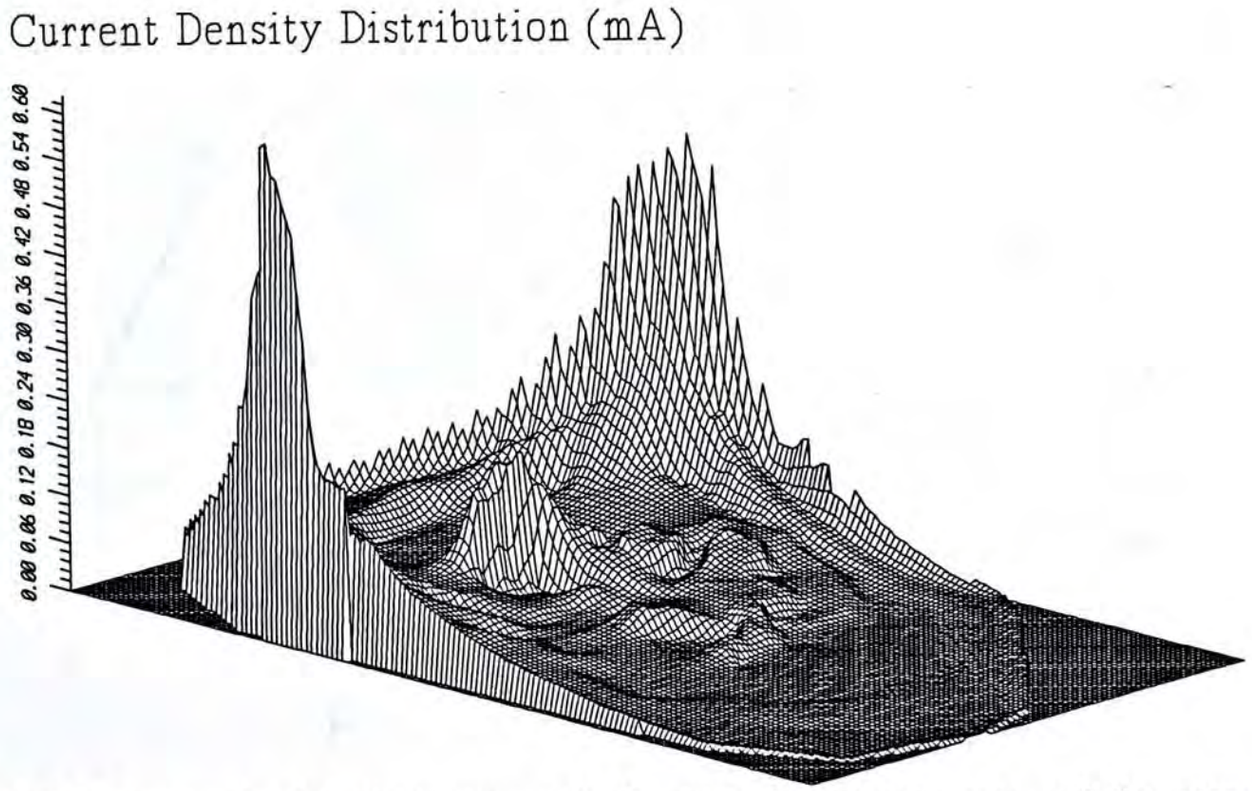

Figure 3.6 Current density distribution with the heart in diastolic state and the current electrode at the position 18 and 85 (see figure 3.5).

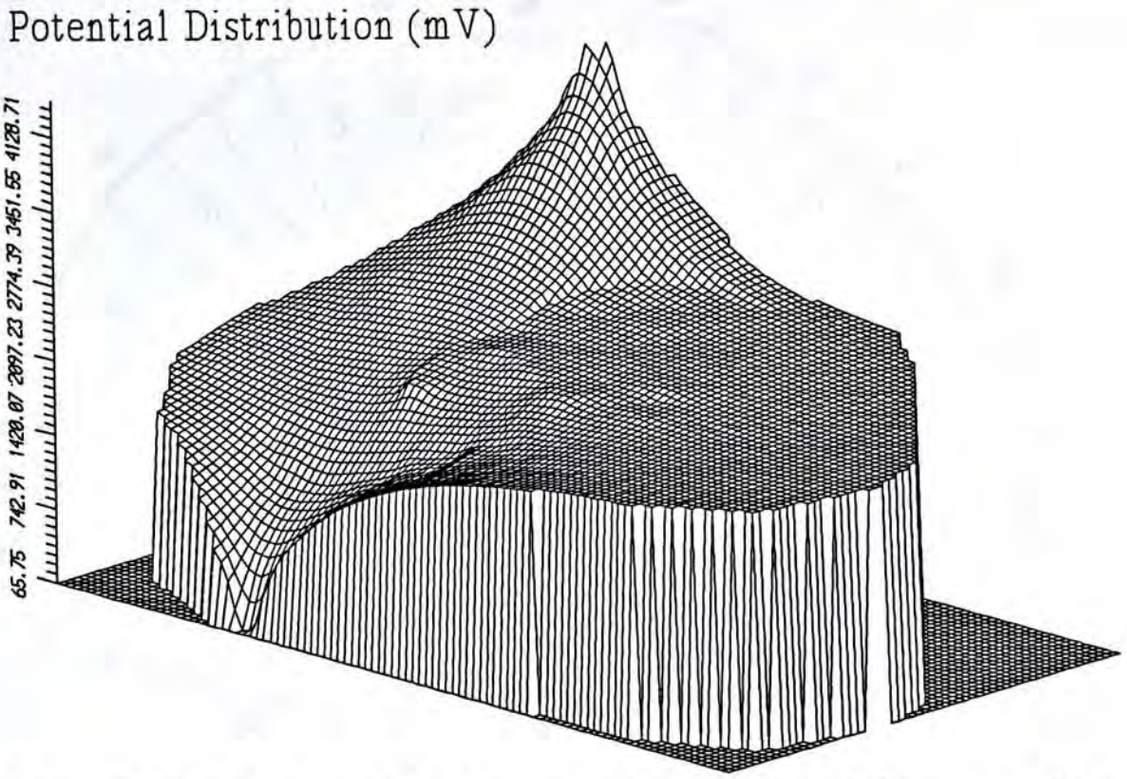

Figure 3.7 Potential distribution with the heart in diastolic state and the current electrode at the positions 18 and 85 (see figure 3.5).

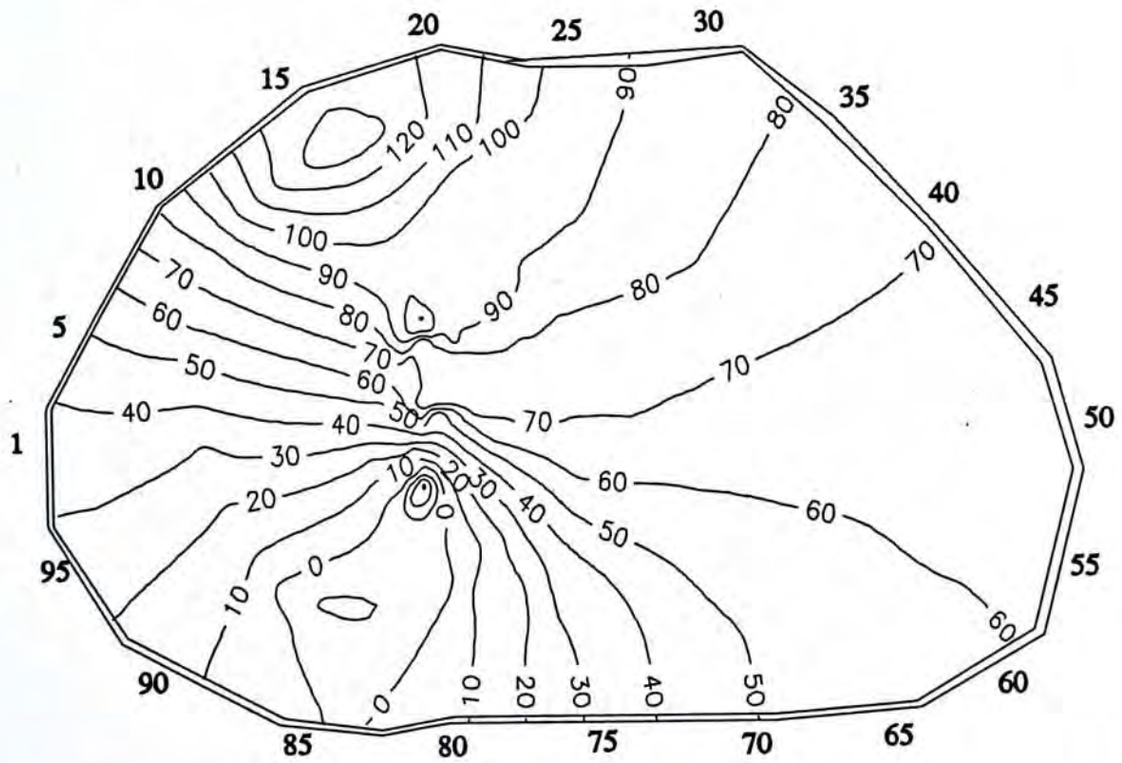

Figure 3.8 The differential potential distribution resulting from the right lung and the pulmonary artery expansion.

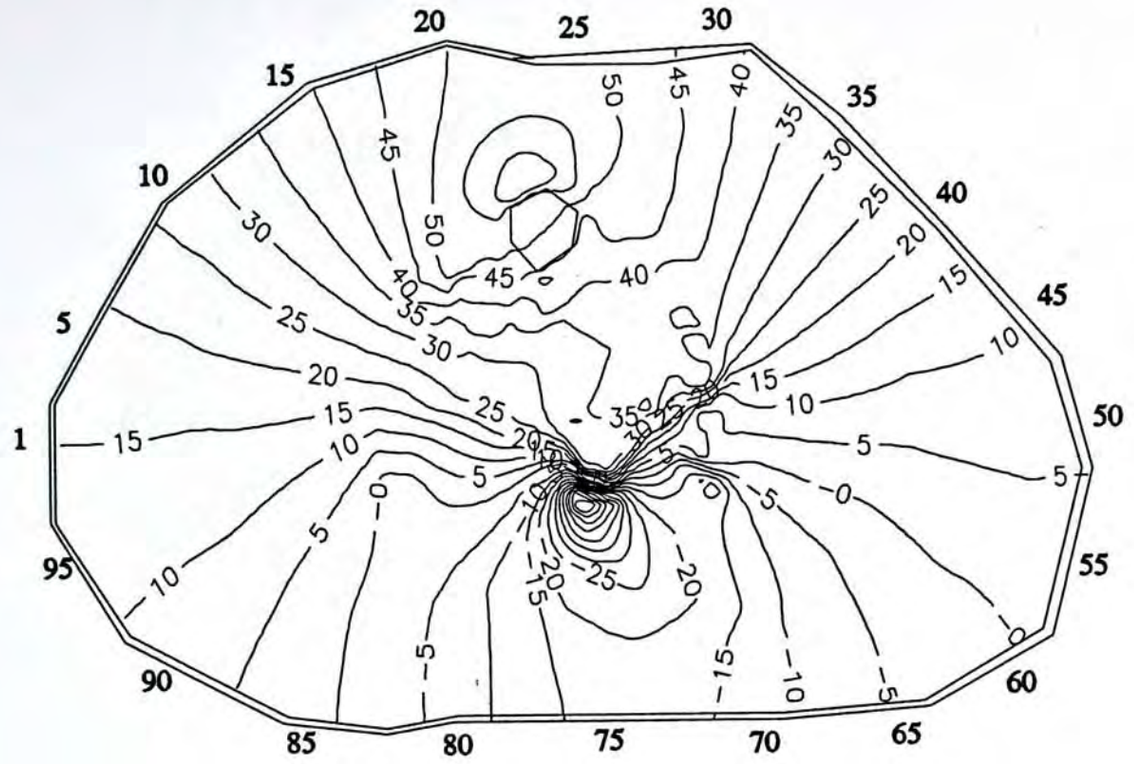

Figure 3.9. The differential potential distribution resulting from other origins.

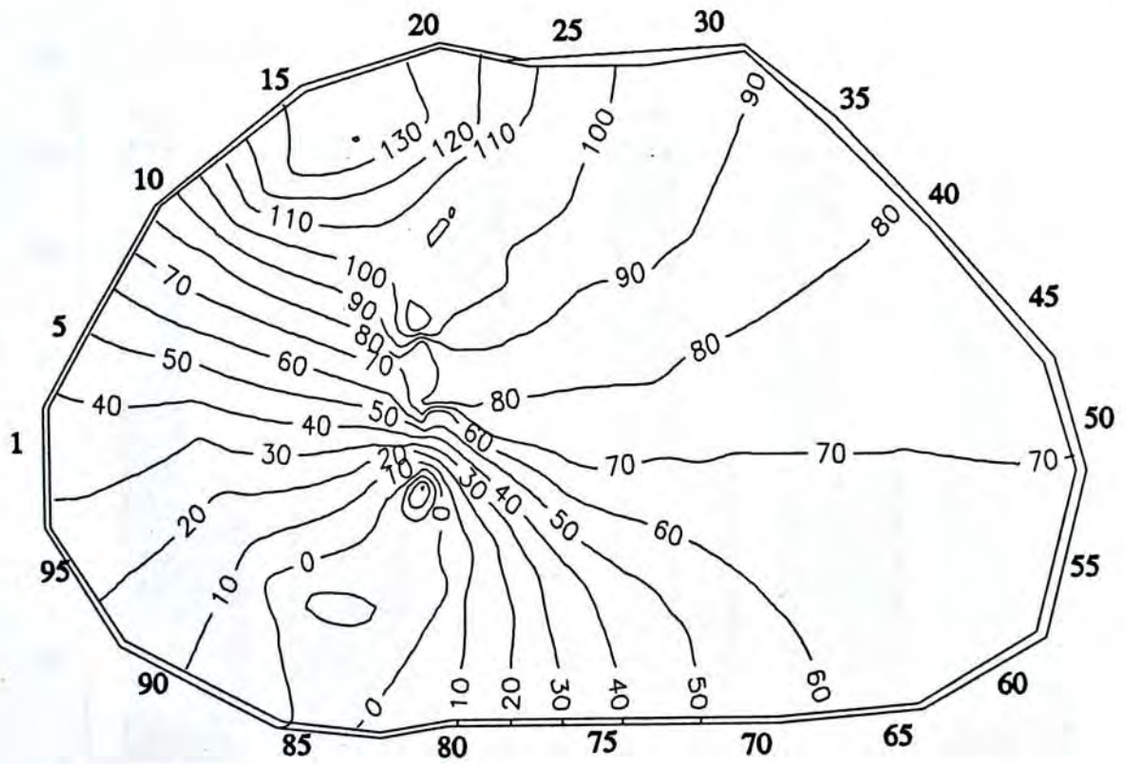

Figure 3.10 The differential potential distribution resulting from the right pulmonary artery and right lung with electrode size six times larger than the existing one.

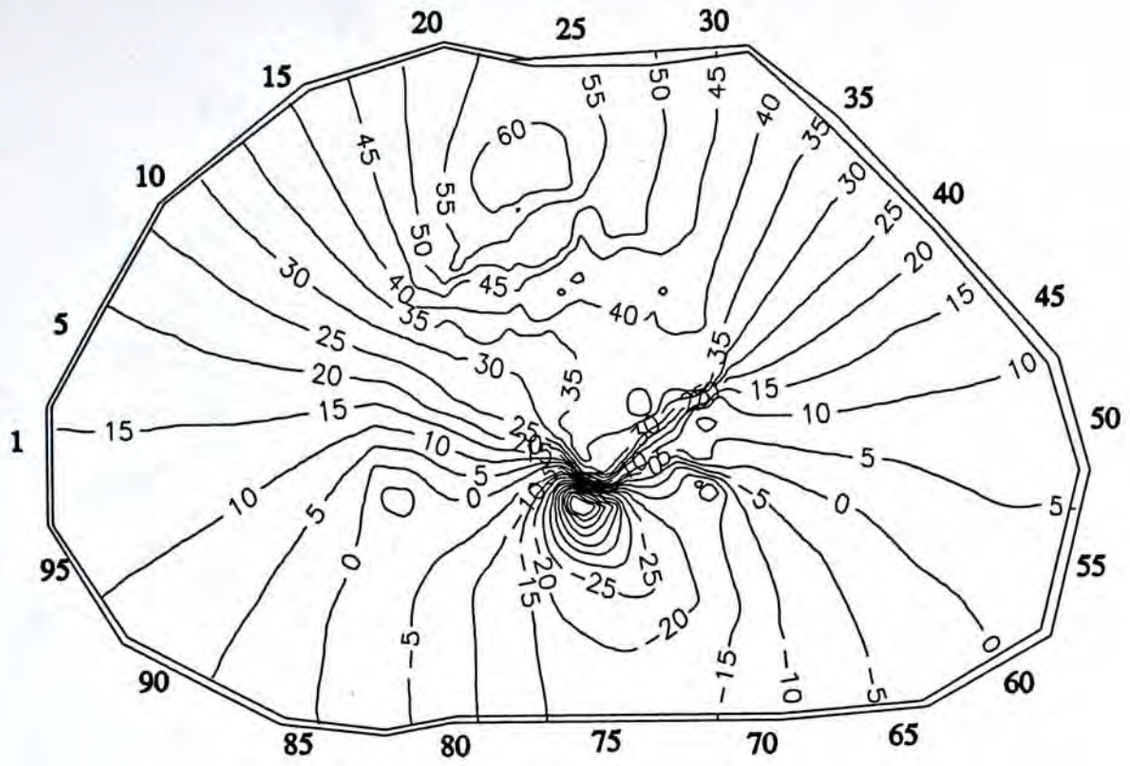

Figure 3.11 The differential potential distribution resulting from other origins with electrode size six times larger than the existing one.

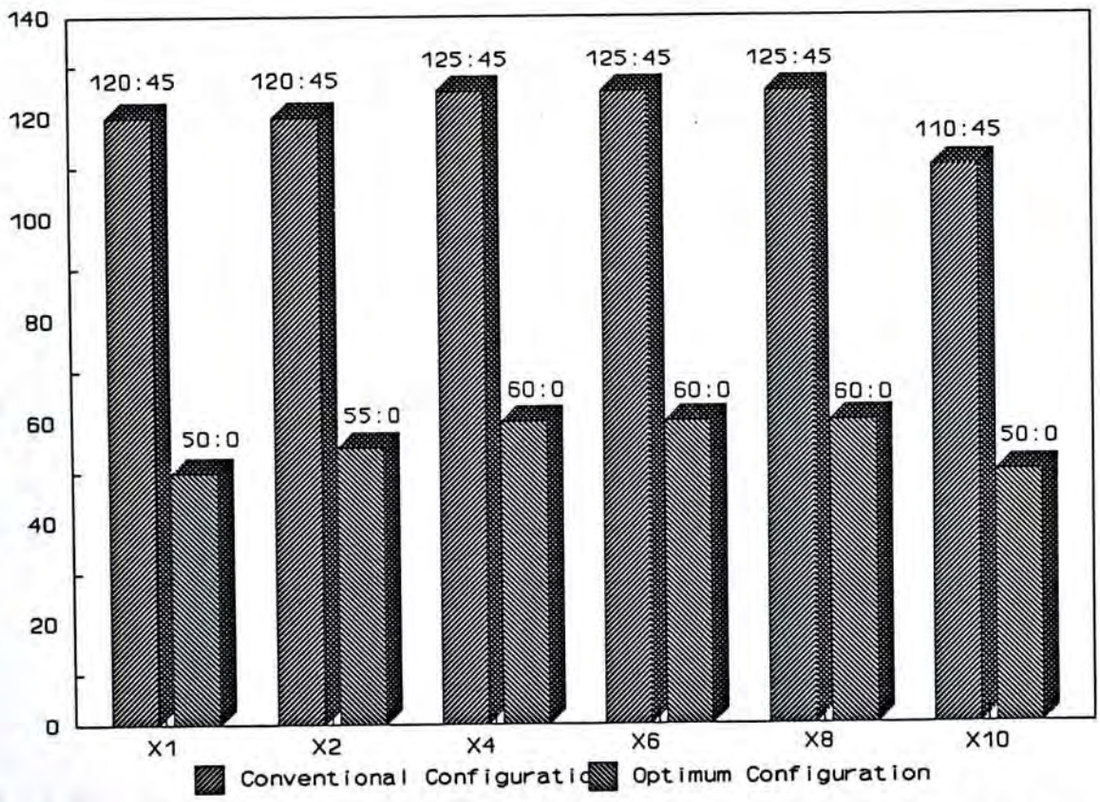

Figure 3.12 The plots of RPTRC values against the electrode size for both the conventional and optimum electrode configurations.

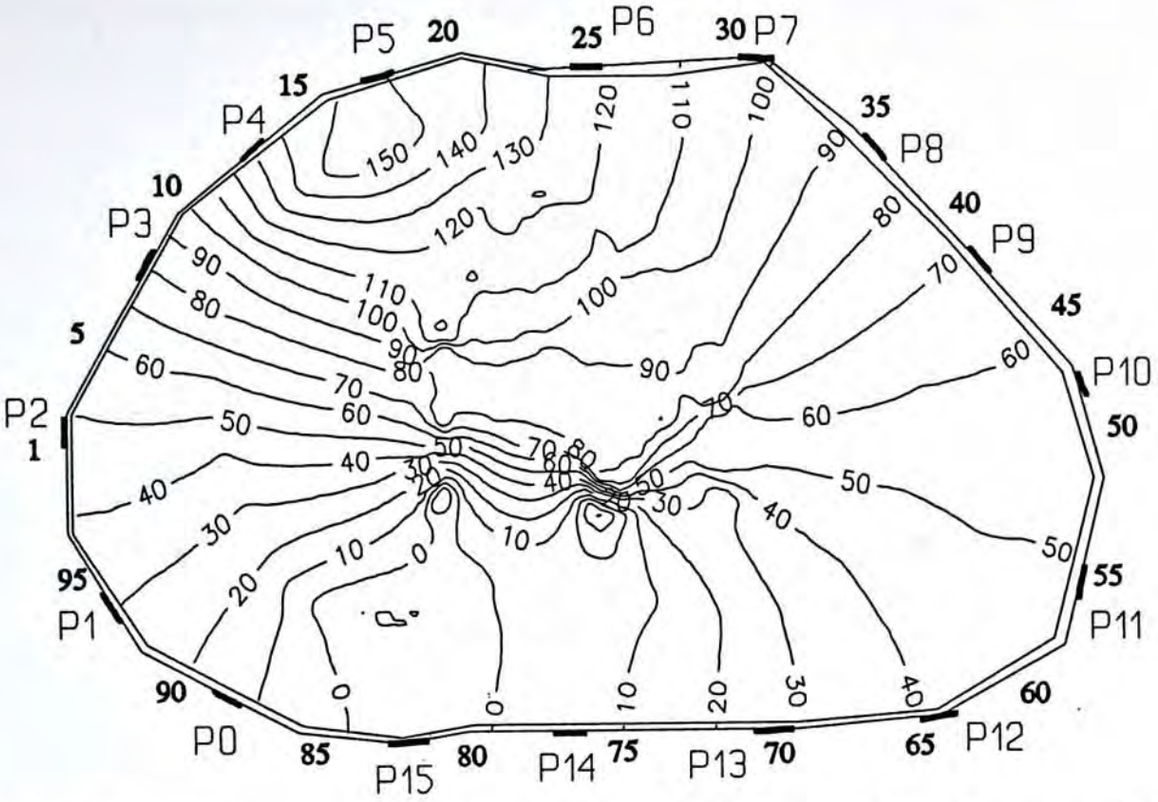

Figure 3.13 The differential potential distribution resulting from the total effect of all origins.

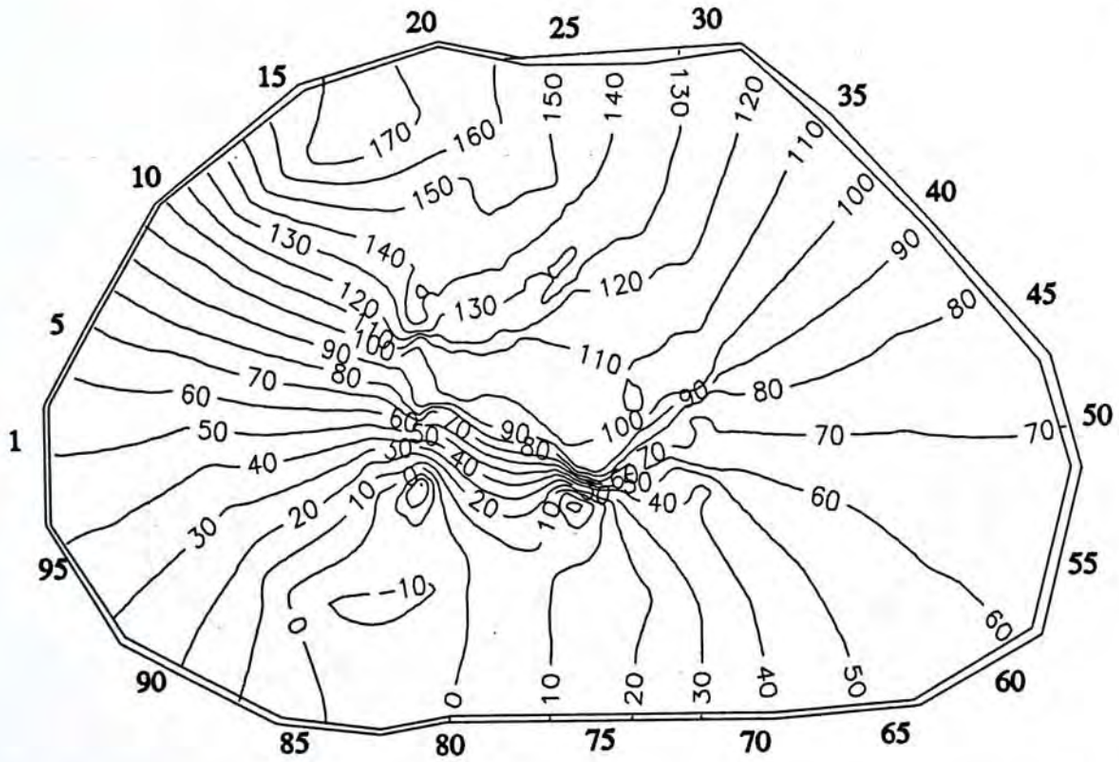

Figure 3.14 The differential potential distribution calculated via the summation of those of figures 3.8 and 3.9.

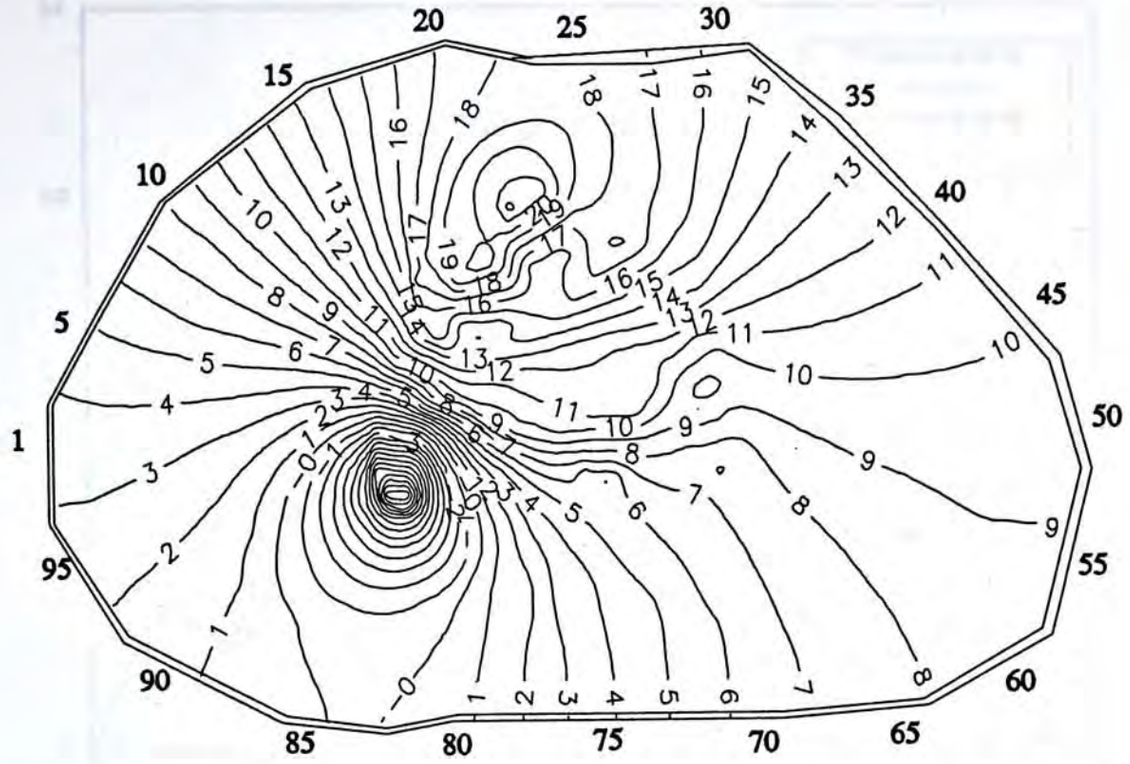

Figure 3.15 The differential potential distribution resulting from the blood resistivity decrease during the heart systole.

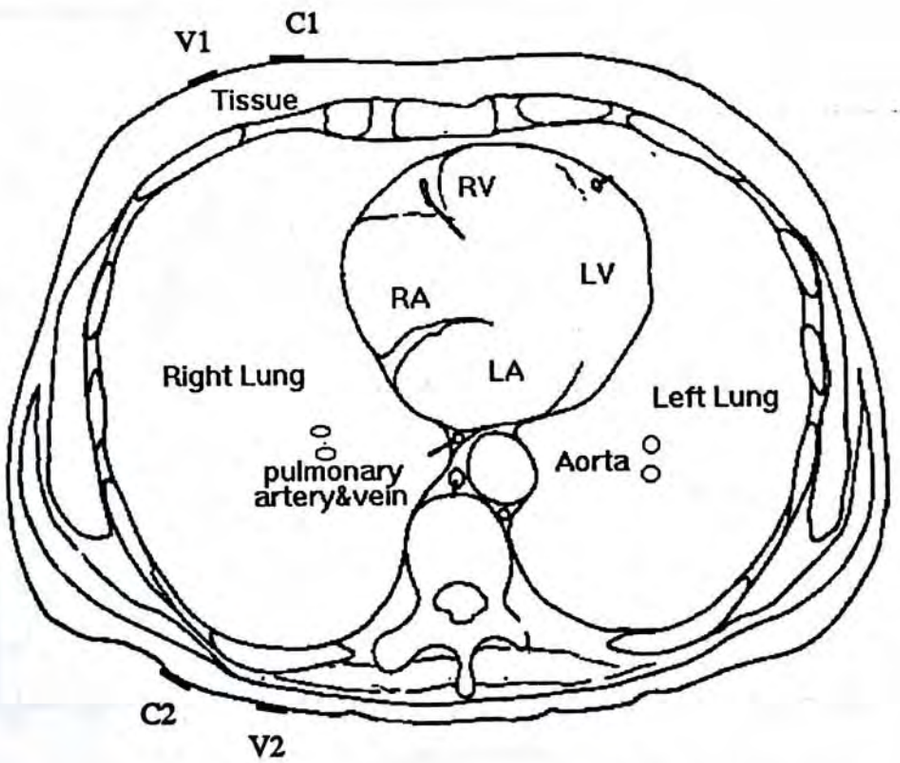

Figure 3.16 A transthoracic cross-section at level T7 and T8. The current electrodes are placed at C1-C2, and the voltage picked-up electrodes at V1-V2.

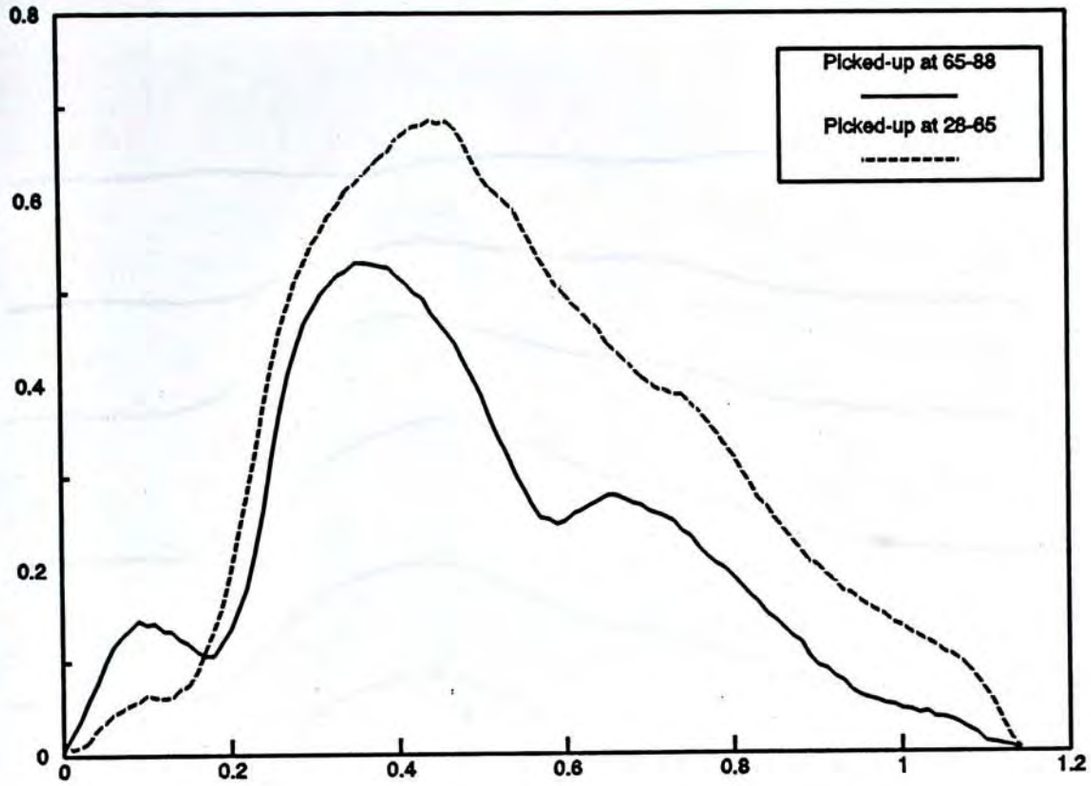

Figure 3.17 Rheographic waveforms picked up at positions with the optimum and worst RPTRC values.

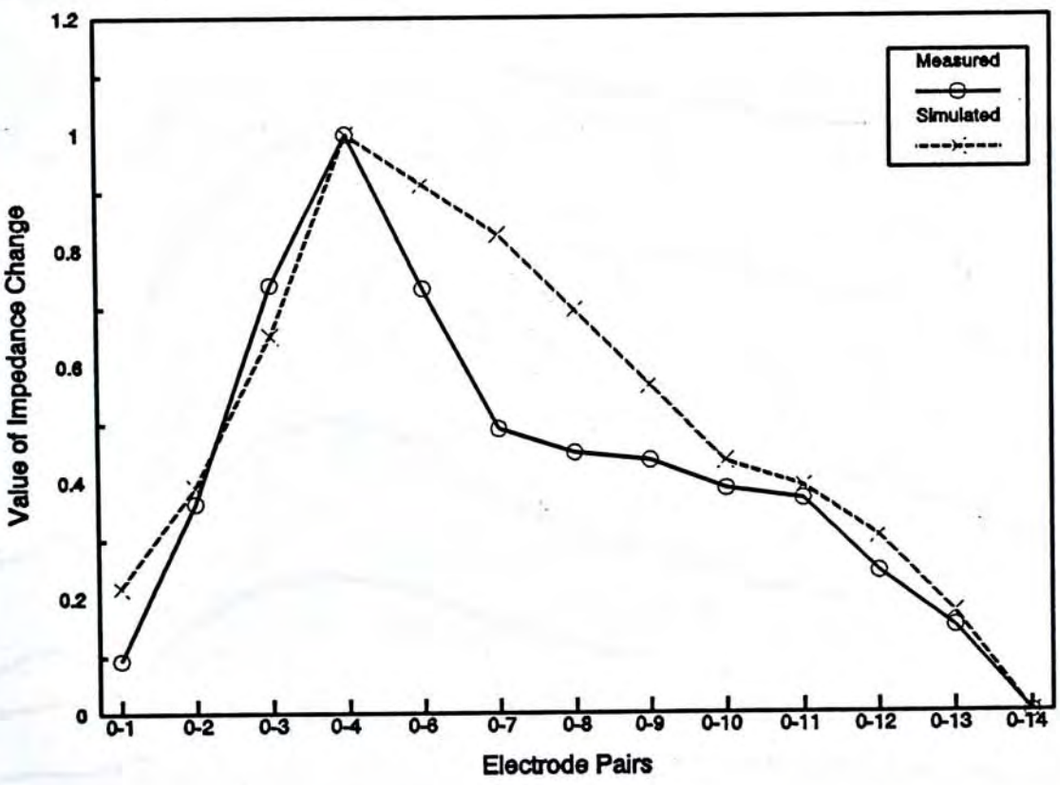

Figure 3.18. Plots of amplitude values of measured and simulated data along the thoracic surface.

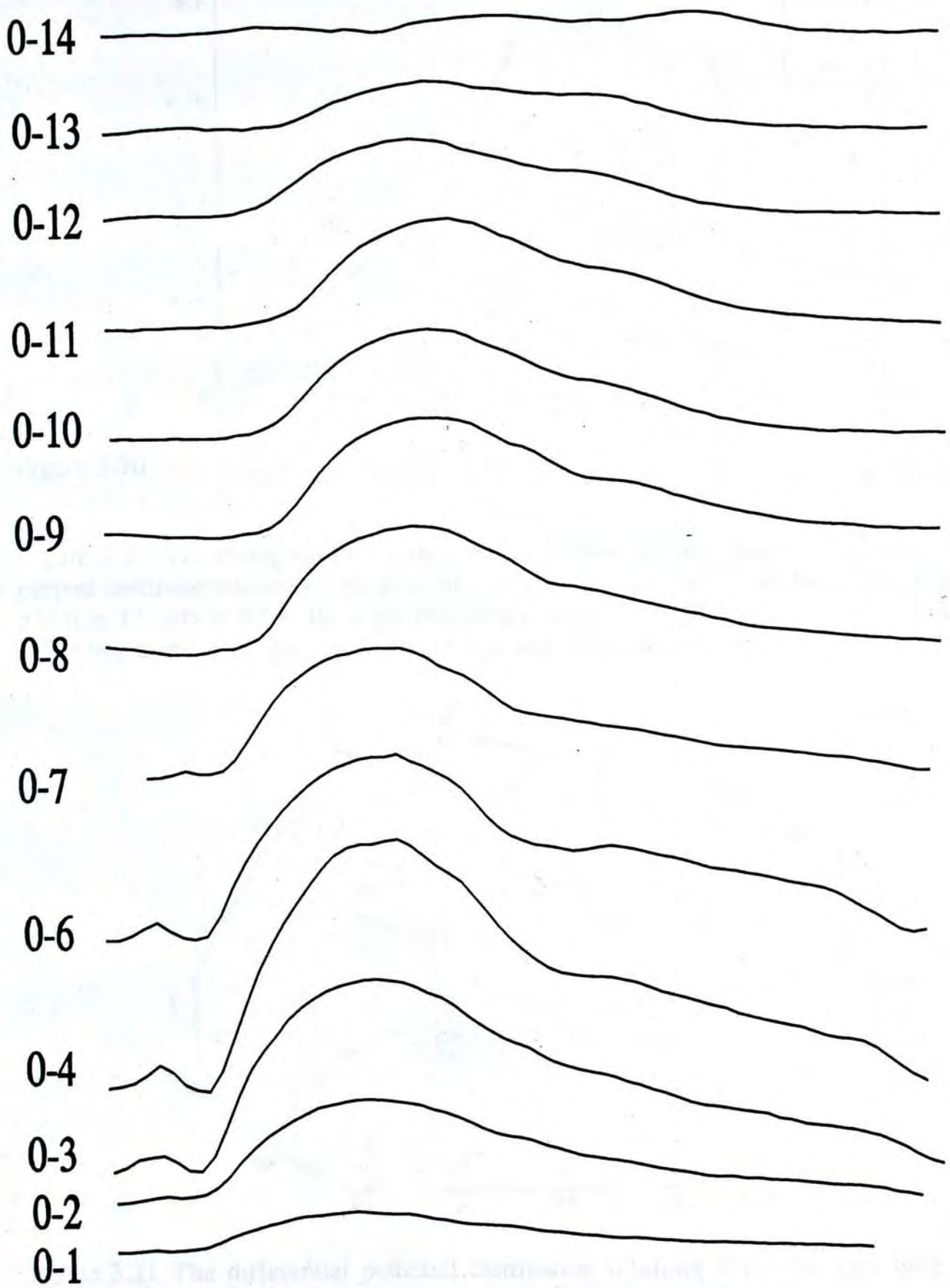

Figure 3.19 Waveforms picked up along the thoracic surface at labels P0 and P1, P0 and P2, ..., P0 and P13.

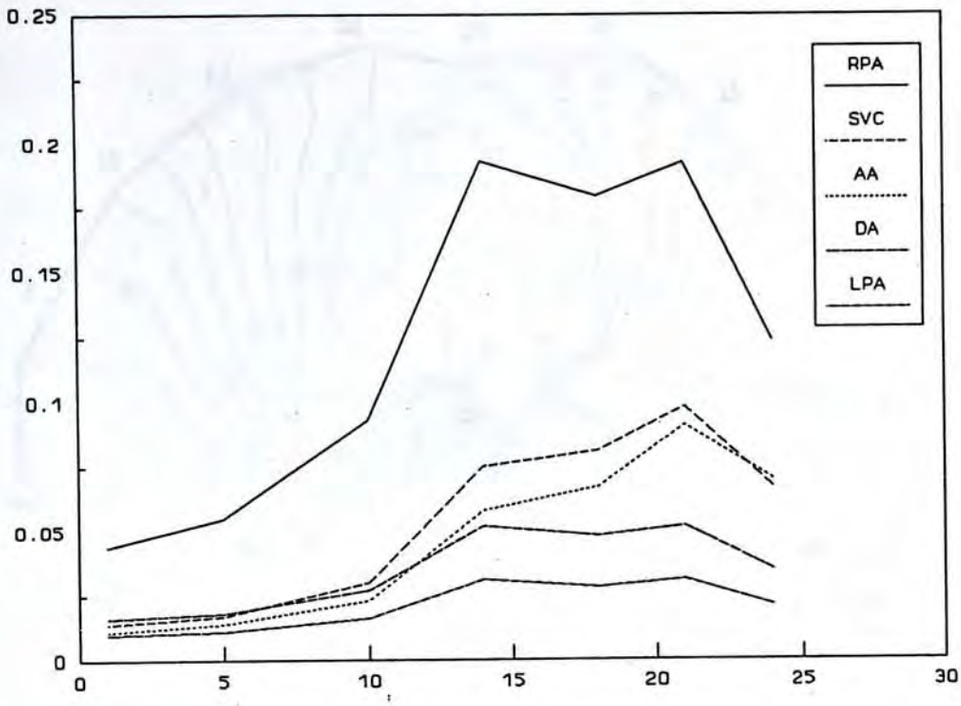

Figure 3.20

Figure 3.20 The changing trends of current densities at the places of possible origins vs current electrode positions. One electrode fixed at the position 85, another changes around the position 17, where RPA, the right pulmonary artery; SVC, the superior vena cava; AA, the ascending aorta; DA, the descending Aorta and LPA, the left pulmonary artery.

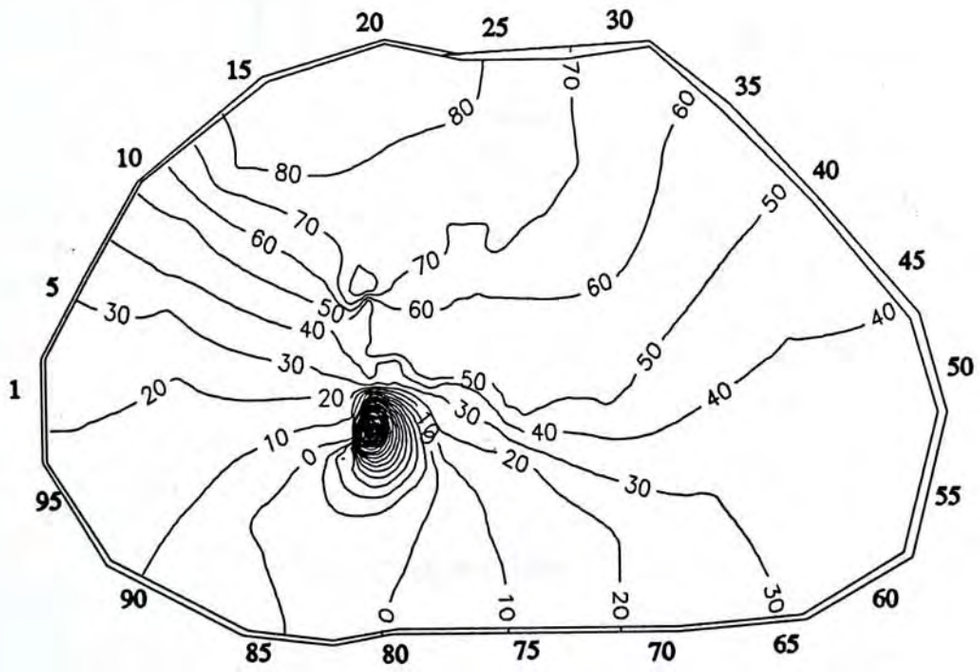

Figure 3.21 The differential potential distribution resulting from the right lung and right pulmonary artery with the resistivity of the lungs increased 10 times.

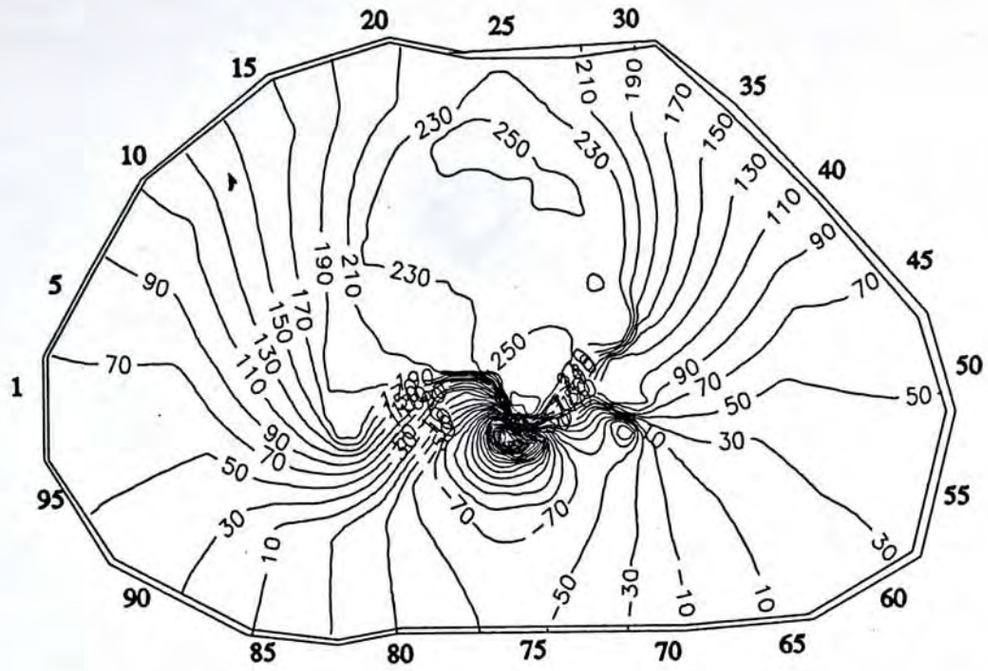

Figure 3.22 The differential potential distribution resulting from other origins with the resistivity of the lungs increased 10 times.

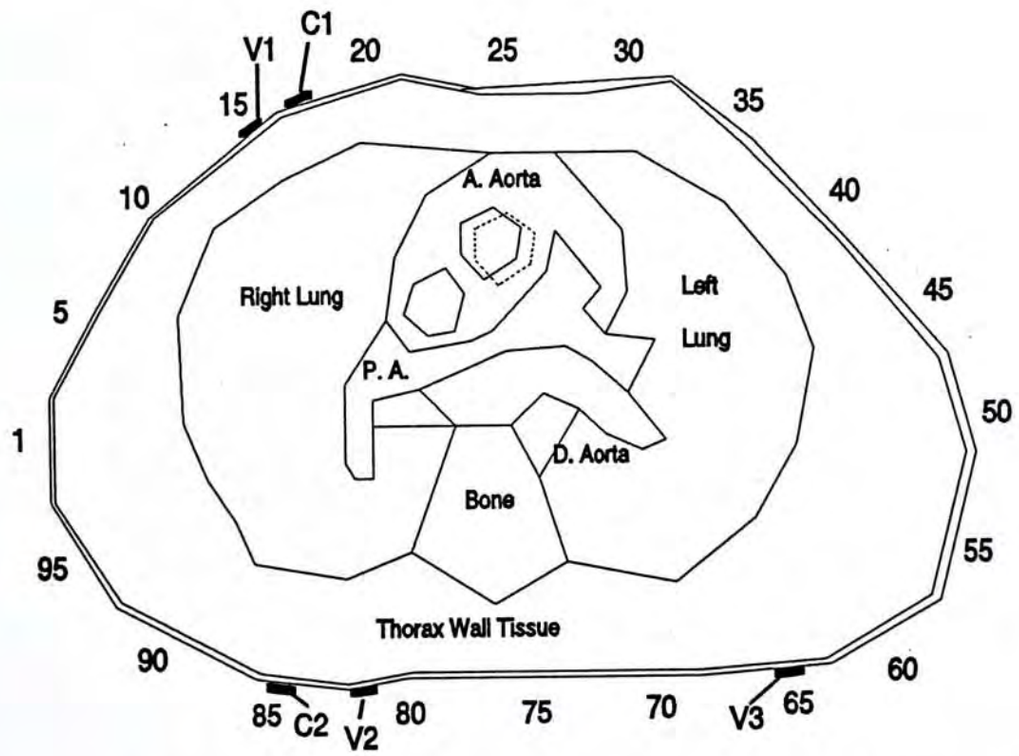

Figure 3.23 A sketch of the 2D model indicating the position variation of the ascending aorta.

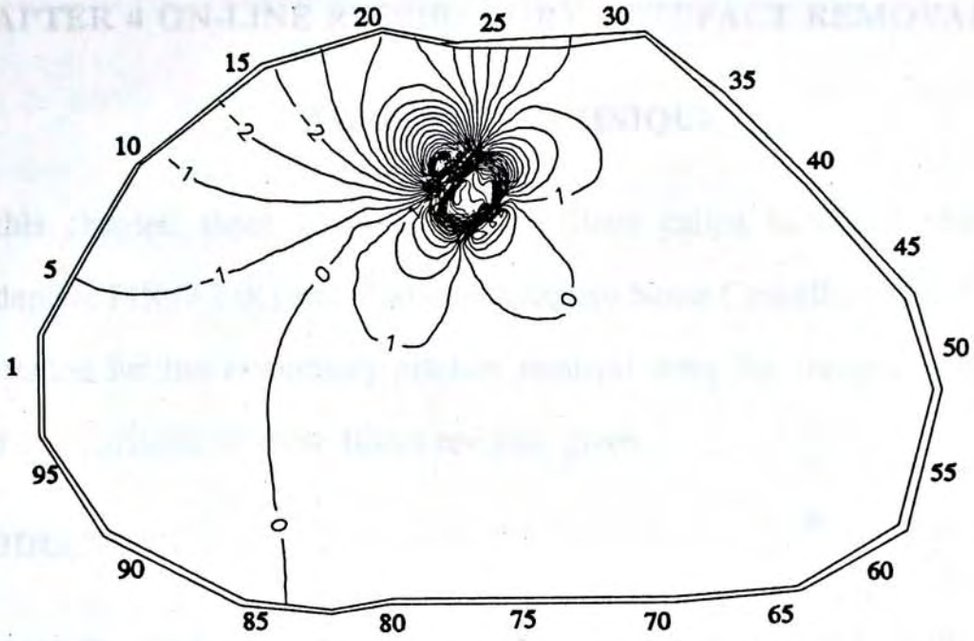

Figure 3.24 Differential potential distribution resulting from the acending aorta position change.

CHAPTER 4 ON-LINE RESPIRATORY ARTEFACT REMOVAL VIA ADAPTIVE TECHNIQUE

In this chapter, three adaptive on-line filters called Modified Moving Averager (MMA), Adaptive FIR (AFIR) and Modified Adaptive Noise Canceller (MANC) are proposed and implemented for the respiratory artefact removal from the rheopneumographic signal. Results and comparisons of these filters are also given.

4.1 INTRODUCTION

Because the electrical impedance rheopneumogram is detected via the EBI technique which is an indirect measurement method, its accuracy and resolution depend on, among other factors. In the ideal case, the transthoracic impedance signal (TIS) should reflect the pulsatile picture of the relevant pulmonary circulation only. However, in view of the mostly electrically conductive but inhomogeneous structures of the tissues within the thorax, the current lines between the current electrodes spread out and may follow very unpredictable paths. This means that besides the blood flow in the pulmonary circulation, activities of other organs such as the heart, the systemic circulation and the lungs, may be reflected in the TIS waveform. Studies on the composition of TIS (chapter 3) show that there exist an optimum electrode configuration such that the interference from the heart and systemic circulation can be made insignificant. The respiratory artefact, however, because of its extensive coverage over the whole lung and its large amplitude, can not be avoided by simply adjusting the electrode configuration. In addition, artefact resulting from the electrode motion and the 50 Hz interference can also complicate the rheopneumographic measurement ([QU 86]).

Conventional fixed filters can not be efficiently applied to eliminate such artifacts. Because like other biomedical signals, the rheopneumographic and respiratory signals are time varying and different from subject to subject. In frequency domain, one can observe the near inbanding nature of the rheopneumogram and the respirogram and variation of these spectra from time to time with the cardiac activities. With a consideration about these, adaptive

techniques are necessary to eliminate the respiratory artefact.

Earlier attempts in respiratory artefact removal from impedance rheopneumogram using Adaptive Noise Cancellation (ANC) ([CHUN 88] [CHOY 92a]) were successful to some extent. In these works, the respiratory reference signal was obtained from a weighted sum of the ribcage and diaphragm components of the Respiratory Inductance Plethysmogram (RIP) ([WATS 80] [SPIE 83]). However, the ANC can adapt successfully only for time-stationary or at best very slowly time-varying signals in view of the finite convergent time. As the respiratory pattern of most patients often changes from cycle to cycle, the phase lag in adapting to this short-term variations can cause significant distortion in the resultant waveform.

On the other hand, the averaging methods were also reported in previous publications ([PATT 78] [MUZI 85] [MIYA 81]). Although averaging can smooth out such short-term respiratory irregularities, it also loses track of short-term rheopneumographic changes. It is, therefore, useful only for analysis purposes when cycle-to-cycle intrinsic variations can be ignored.

In this study, several improvement approaches to the previous works were proposed and implemented. Among these, there are a modified scheme of the ANC method (MANC), a modified moving averager (MMA) and an adaptive FIR filter (AFIR). The MANC applies moving averaging method to obtain the respiratory reference signal instead of using the RIP signal. As a result, a more correlated respiratory reference signal can be obtained so that the performance of the MANC is improved in terms of the signal to noise ratio and the signal distortion ratio. For the conventional moving averaging and FIR filtering techniques, short time DFT technique is applied to analyzing the TIS in real time so that the optimal cutoff frequency can be determined adaptively for the filter at any time. Since the cutoff frequency of a moving averager is determined by its window span, therefore, adaptively changing its window span and hence its cutoff frequency can result in optimum filtering result. For the FIR filter, a Coefficient Lookup Table (CLT) is applied so that it needs not to re-calculate

the coefficients when the cutoff frequency changes. Its coefficients can be obtained just by looking up in the CLT.

4.2 ANALYSIS OF THE TIS

The components of the transthoracic plethysmographic signal may include the useful component of rheopneumogram and other artifacts such as the respiratory signal, motion artefact and 50 Hz interference as shown in figures 4.1 and 4.2.

Figure 4.1 shows a typical TIS waveform (ΔZ) and its power spectrum along with simultaneous ECG waveform. There are two spectral distributions located at about 0.6 Hz and 1.4 Hz. The left one is the band frequencies of the respiratory signal, and right one the band frequencies of the rheogram. Because of subject-to-subject variations in wave morphology and the heart-beat rate the two spectral distributions may have different spread and peak locations, as a result that even slight overlap is possible.

In order to have a better understanding of the nature and possible extent of those spectral variations, the plethysmographic spectra of some 40 odd subjects had been statistically analyzed and the respiratory and rheopneumographic peak distributions are shown in figure 4.3. The results indicate that the respiratory peak has a Gaussian-like distribution centering about 0.4 Hz and spreading over a range of 0.1 to 0.9 Hz. On the other hand, the rheographic signal covers the range of 0.7 to 1.8 Hz with a Gaussian distribution centring about 1.3 Hz. *This result suggests that the two kind of signals may be separated by conventional lowpass or highpass filter* ***with suitable selection of cutoff frequency*** *because statically there is a frequency gap of 0.9 Hz between these two signals.*

However, in some odd cases, the highpass filter or lowpass filter may not be useful because of the inbanding in frequency of the two signals. For some people who can breath very smoothly so that his respiratory waveform is more like a sine wave and results a narrow band in frequency. But for some people who can not breath smoothly, his respiratory waveform pattern may change from time to time so that a broader frequency band results

which may overlap with that of rheopneumogram as shown in figure 4.4. This introduces the difficulty of setting a suitable cutoff frequency for any high pass or low pass filter to separate these two components. If the overlap is serious, the conventional high pass or low pass filter fails. In such cases, an adaptive noise canceller with a noise reference signal may be tried.

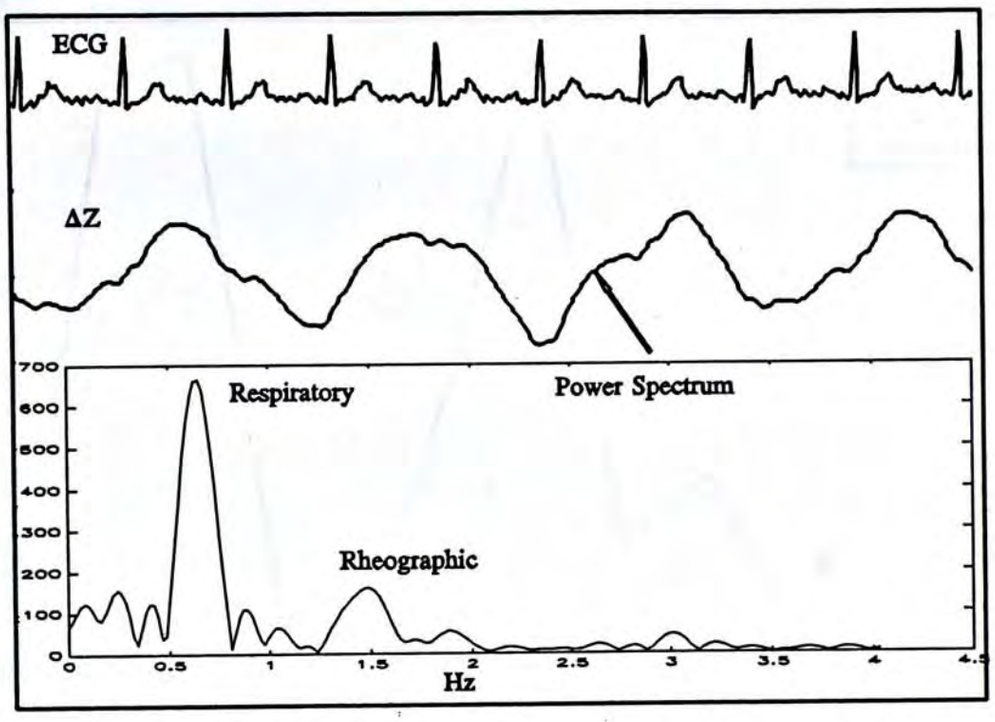

Figure 4.1. A typical TIS waveform (ΔZ) recorded along with ECG; Power spectrum of ΔZ is also shown.

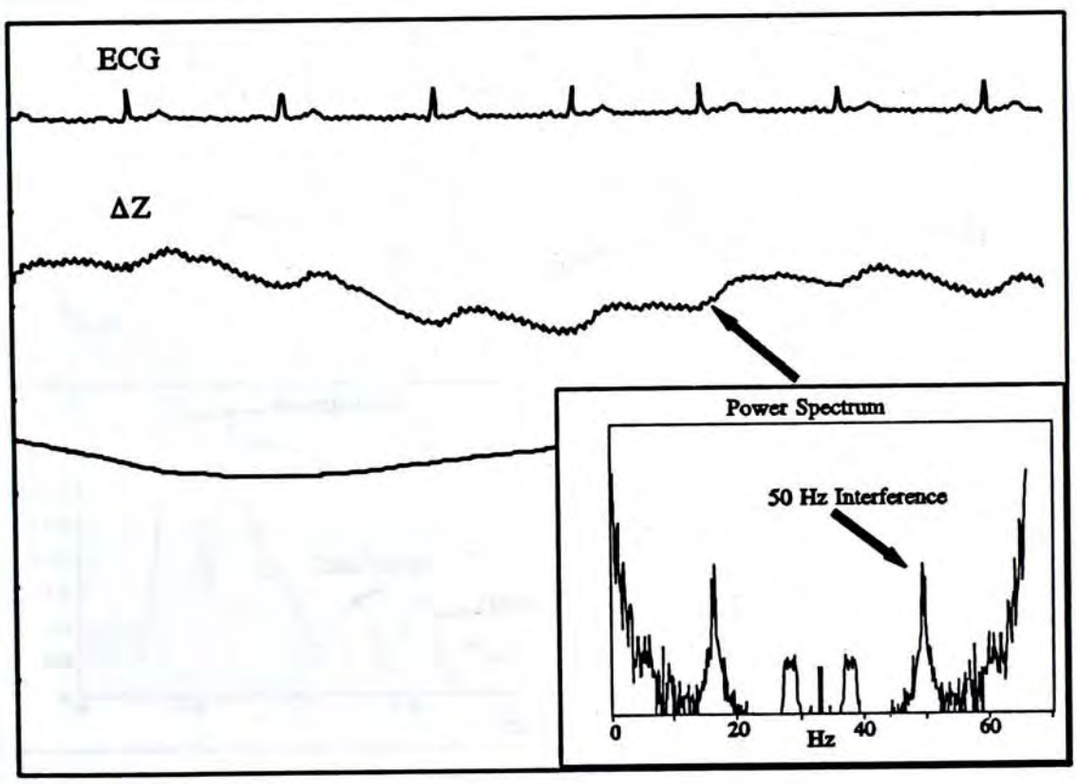

Figure 4.2 An example of TIS waveform interfered by the 50 Hz interference. Power spectrum of ΔZ wave is shown in insert. (Sampling rate 67 samples/sec)

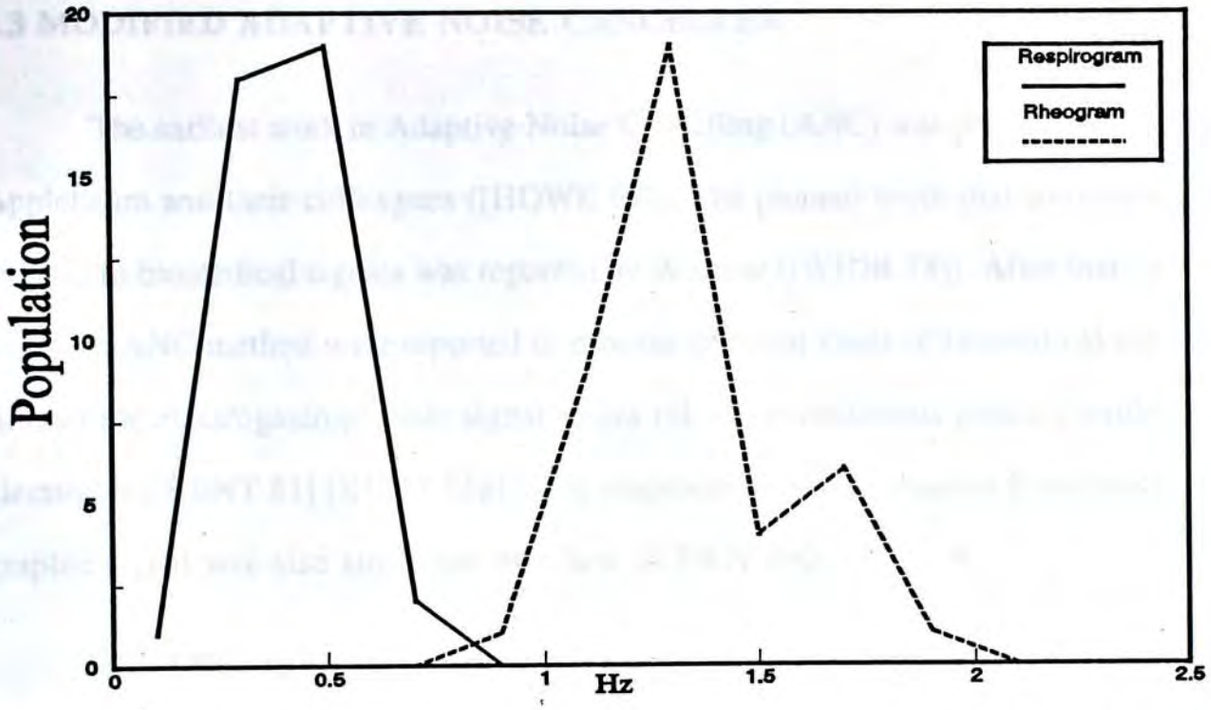

Figure 4.3. Distribution of most significant frequency peaks of respirogram and rheopneumogram statistically calculated from 40 subjects.

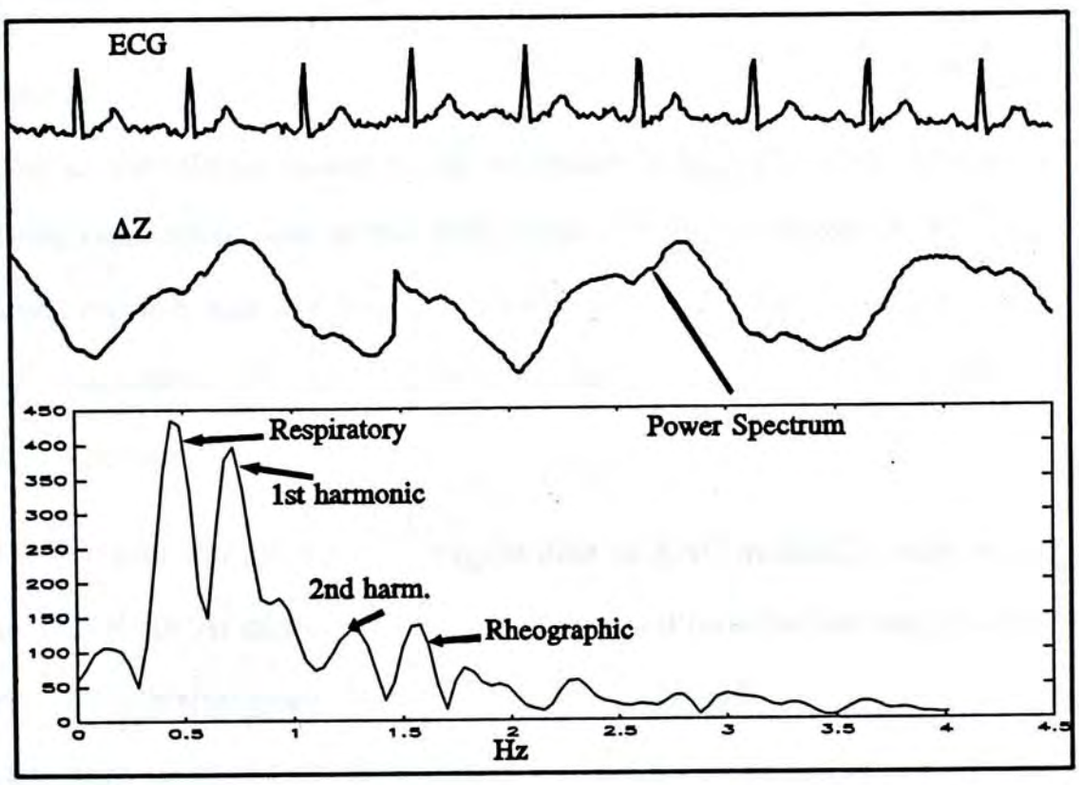

Figure 4.4 An example of TIS recorded with overlapping respiratory pattern along with the ECG. The power spectrum of ΔZ is also shown.

4.3 MODIFIED ADAPTIVE NOISE CANCELLER

The earliest work in Adaptive Noise Cancelling (ANC) was performed by Howells and Applebaum and their colleagues ([HOWE 65]). The pioneer work that introducing the ANC method to biomedical signals was reported by Widrow ([WIDR 75]). After that, several works based on ANC method were reported to process different kinds of biomedical signals. Kentie filtered the electrogastrographic signal to get rid of the cutaneous artefact resulting from the electrodes ([KENT 81] [KENT 81a]). The respiratory artefact removal from the electrogastrographic signal was also attempted by Chen ([CHEN 89]).

The ANC method has long been studied and used to remove the respiratory artefact in our laboratory. It can be successful if the following conditions can be satisfied, 1) the noise signals in the primary and reference inputs are time-stationary; 2) there is no cardiac components in the noise reference input. The RIP signal may be a good respiratory reference because it had been proved to correlates well with the respiratory signal acquired by spirometer ([COHN 78] [WATS 80] [SINT 88]). However, results given by the ANC&RIP method are still not so satisfactory as there is still wave fluctuations shown in the filter output. The reasons for the failure of this method may be explained by the following aspects: 1) The finite convergent time of the ANC method results it always in the converging status and can not reach a true convergence; 2) the RIP signal may not correlate well with the respiratory component of TIS even though it correlates well with the overall respiratory signal acquired by spirometer.

For the problem of finite convergent time of ANC method, it may be possibly solved with fast algorithms. At this present stage, we have not found a fast enough algorithm to track variations of the respirogram. But to the latter, however, a modified scheme of the ANC method has been proposed which applied a moving averager to the TIS signal resulting in a very closely correlated respiratory reference. The TIS respiratory signal is detected with another pair of pick-up electrodes, which contains more respiratory component and less rheopneumographic component. *Since the RIP is not used in the measurement, therefore, this*

modified scheme has advantages of simplified measurement setup and so obtained EBI respiratory may correlate better to the respiratory component in the input TIS than that obtained from RIP.

4.3.1 PRINCIPLE OF THE ANC METHOD

Figure 4.5 shows the basic noise cancelling problem and the ANC solution to it. The notations follow that of Widrow et al. [WIDR 75]. The primary input composes of signal s and noise n_0. The reference input is noise n_1 which is uncorrelated with the signal but correlated with n_0 in some unknown way. A filter is used to generate y from n_1 such that y should be as close to n_0 as possible. The filter is found by some adaptive algorithms based on the time varying input signal properties.

From figure 4.5, the output signal z is

$$z = s + n_0 - y \tag{4.1}$$

Squaring both sides,

$$z^2 = s^2 + (n_0 - y)^2 + 2s(n_0 - y) \tag{4.2}$$

Taking expectations on both sides and considering that s is uncorrelated with n_0 and y, equation (4.2) becomes

$$E[z^2] = E[s^2] + E[(n_0 - y)^2] \tag{4.3}$$

If the filter is adjusted so that it minimizes power at the canceller output, $E[(n_0 - y)^2]$ is minimized and the signal power is not affected. Meanwhile, the filter output y becomes the best least mean square estimate of n_0.

4.3.2 LMS ALGORITHM

ANC normally use FIR filters in the reference paths. Use of IIR adaptive filters reduces filter order but they usually require complex adaptive algorithms and stability must

be checked after every adaptation. This FIR filter can be implemented via the well known LMS algorithm which is derived according to the stochastic gradient method (Appendix C). It can be illustrated with the equation,

$$w_k(n+1) = w_k(n) + 2\mu e(n)x_k(n) \tag{4.4}$$

where

$w_k(n)$ is the kth weight after n samples

$x_k(n)$ is the reference signal at the kth delay after n samples

$e(n)$ is the error signal after n samples

μ is the convergence factor.

Starting with any initial values, the wight vector is adaptively adjusted by the LMS algorithm. After a sufficient number of adaptations, the wight vector reaches its optimal value. The converging speed is determined by the convergence factor μ; large μ means that a big step is used in searching for the optimal weights and resulting in fast convergence but on the other hand generating more gradient noise in the steady state. The optimal values of μ is a compromise between small gradient noise but slower convergence (small μ) and more gradient noise but a fast convergence (large μ). In practice, μ is chosen empirically (eg., 10^{-9}).

4.3.3 MANC METHOD

A modified adaptive noise canceller which combines the simple moving averager (SMA) and ANC method, called MANC method is proposed. Figure 4.6 shows the diagram of the MANC method. This filter is similar to the noise canceller described by Widrow as shown in figure 4.7, in which the artefact reference input may contain the signal component.

In order to show the usefulness of the MANC method, the output signal-to-noise density ratio (SNDR) and signal distortion ratio (SDR) introduced by Widrow ([WIDR 75]) are repeated here. The SNDR is defined as the ratio of signal power density to noise power density, and the SDR is defined as a dimensionless ratio of the spectrum of the output signal

component propagated through the adaptive filter to the spectrum of the signal component at the primary input. Thus the SNDR and SDR can be given as

$$SNDR_{out}(z)=\frac{\delta_{nn}(z)|H(z)|^2}{\delta_{ss}(z)|L(z)|^2} \qquad (4.5)$$

$$SDR(z)=\frac{|L(z)|^2}{|H(z)|^2}$$

where δ_{nn} and δ_{ss} are the power spectra of noise and signal respectively, $H(z)$ and $L(z)$ are the transfer functions for the noise and signal to propagate to the reference input. With careful study of equation (4.5), one can see that if L(z) is much smaller than H(z) over the whole frequency range, the better SNDR and SDR values can be obtained.

In the previous studies on searching of optimal electrode positions, it was found that if the voltage pick-up electrodes were placed between the ribs 3 and 4, the biggest Rheo-pneumographic component to respiratory Artefact component ratio (RTA) could be obtained. On the other hand, the smaller RTA could be obtained at the position of ribs 5-6.

Figure 4.6 shows the electrode placements for the MANC scheme, in which the primary input of the MANC is picked up at the position between ribs 3 and 4 (of large RTA value). Another pair of electrodes are used and placed at the position of ribs 5 and 6 to pick up the respiratory signal (of small RTA value). After processing by a simple moving averager (as a result, the rheopneumographic component picked up at ribs 5-6 is reduced resulting in much smaller RTA value), the TIS respiratory signal is then used as reference input of the MANC. Much smaller RTA value in the reference input corresponds to L(z) to be much decreased, therefore, the SNDR and SDR can be much improved as shown in equation (4.5).

4.3.4 RESULTS

Results of ANC&RIP and MANC along with the raw data, the TIS respiratory signal obtained from the output of the SMA and two RIP signals are shown in figure 4.8. The result of MANC is smoother than that of ANC&RIP which indicates that the respiratory artefact is

suppressed greatly. From the power spectra as shown in figure 4.9, the same result can be observed.

In order to compare the output signal distortion of these two methods, their output signals are correlated to the rheopneumographic signal recorded in apnea. The correlation coefficients of MANC and ANC&RIP to the rheopneumogram of apnea are 0.5703 and 0.4407 respectively indicating the MANC method performs slightly better than the ANC&RIP method.

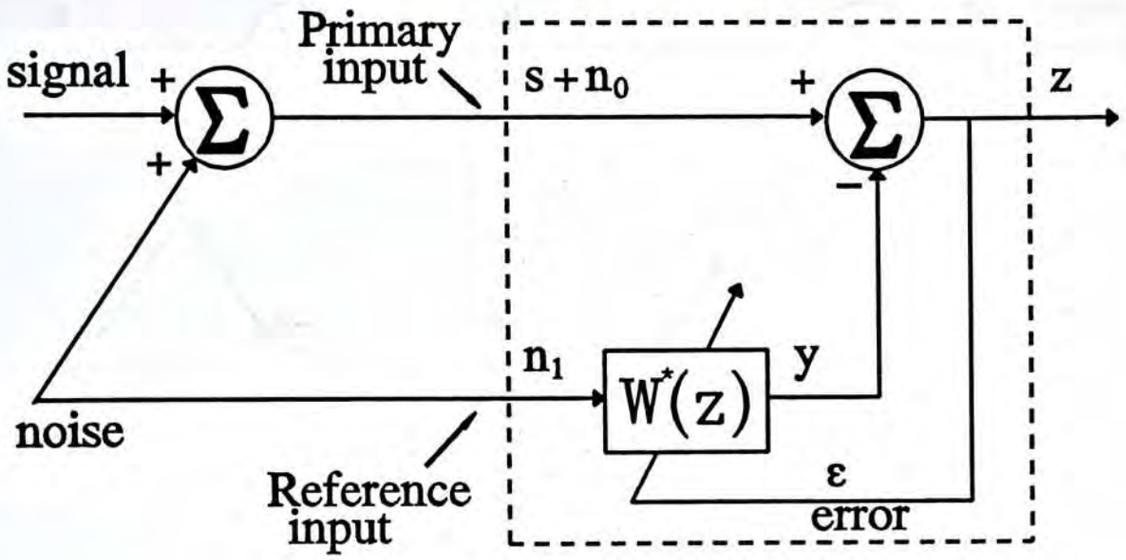

Figure 4.5 Diagram of ANC solution.

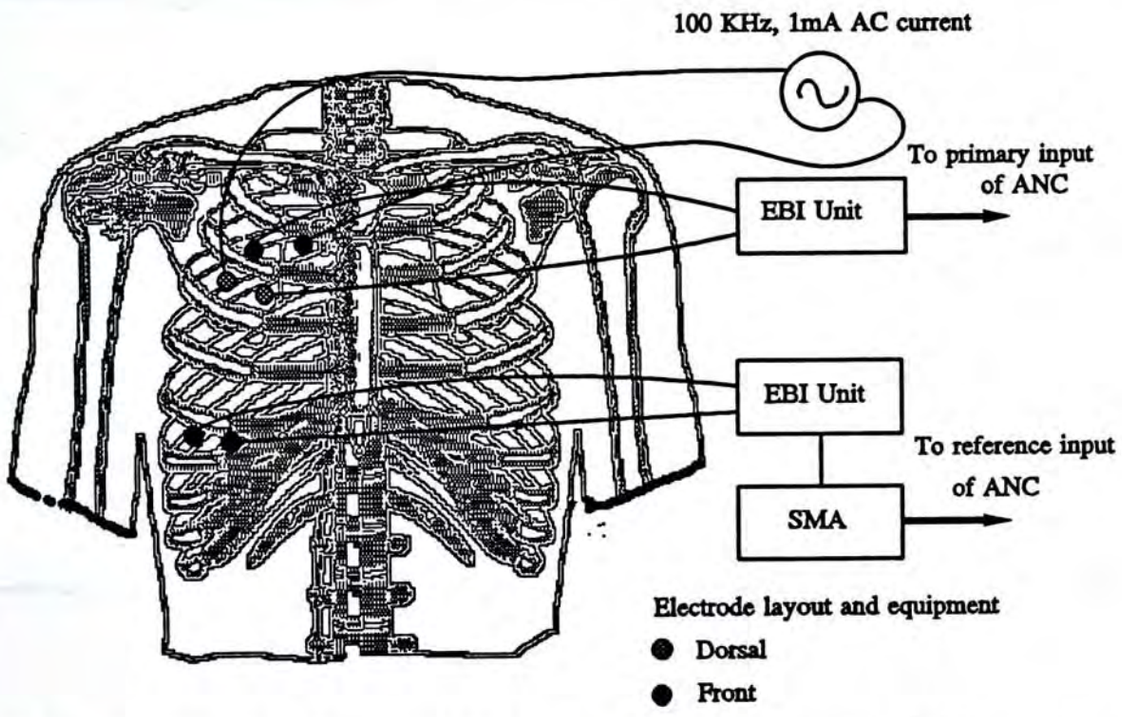

Figure 4.6 Diagram of the modified ANC measurement setup and the electrode placement.

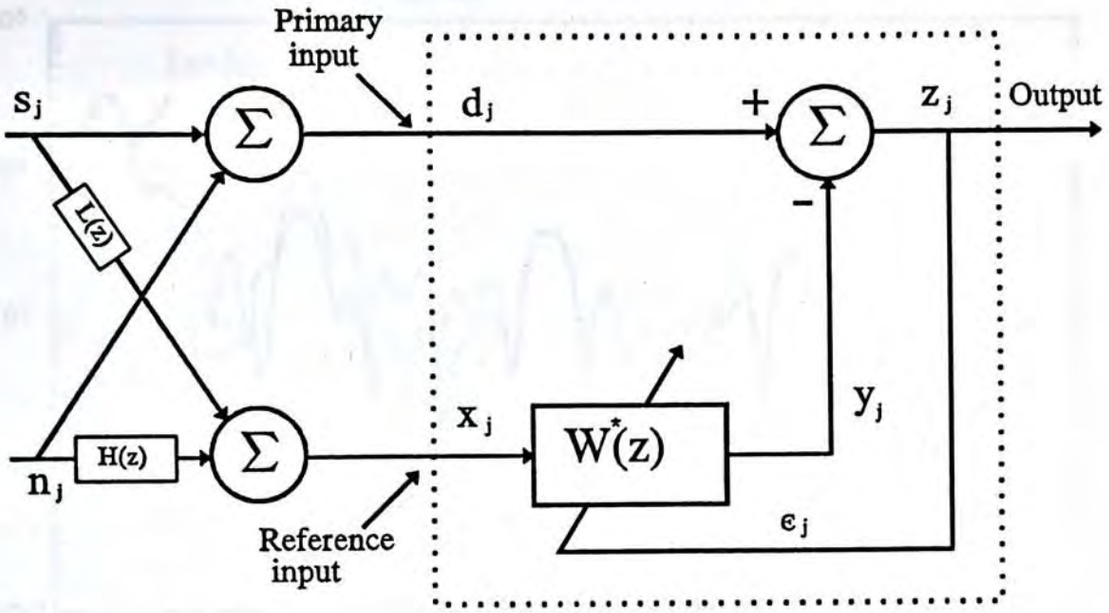

Figure 4.7 Diagram of MANC method when the reference input may contain signal. component.

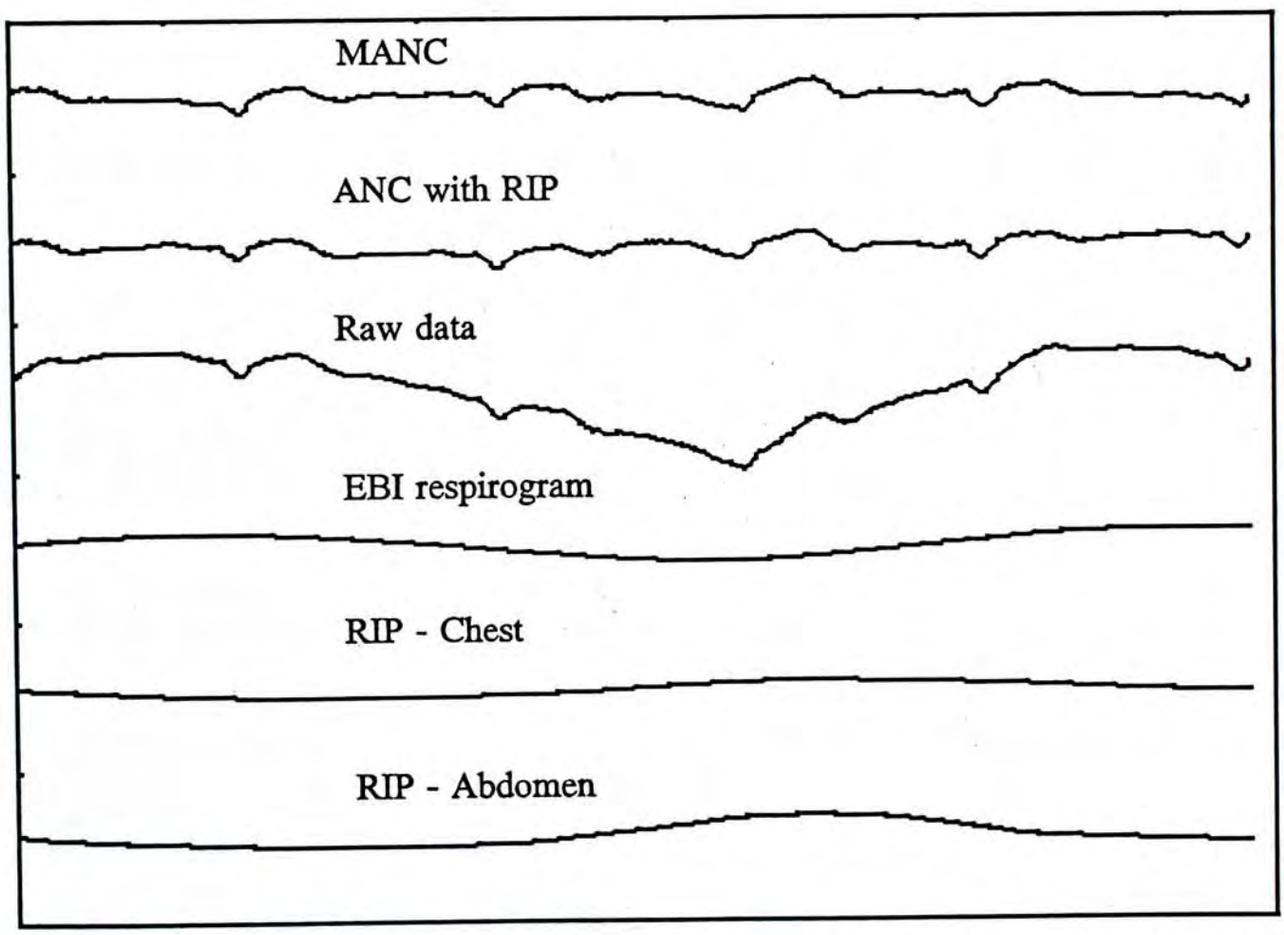

Figure 4.8 Processed results of ANC&RIP and MANC methods along with raw data and RIP waveforms.

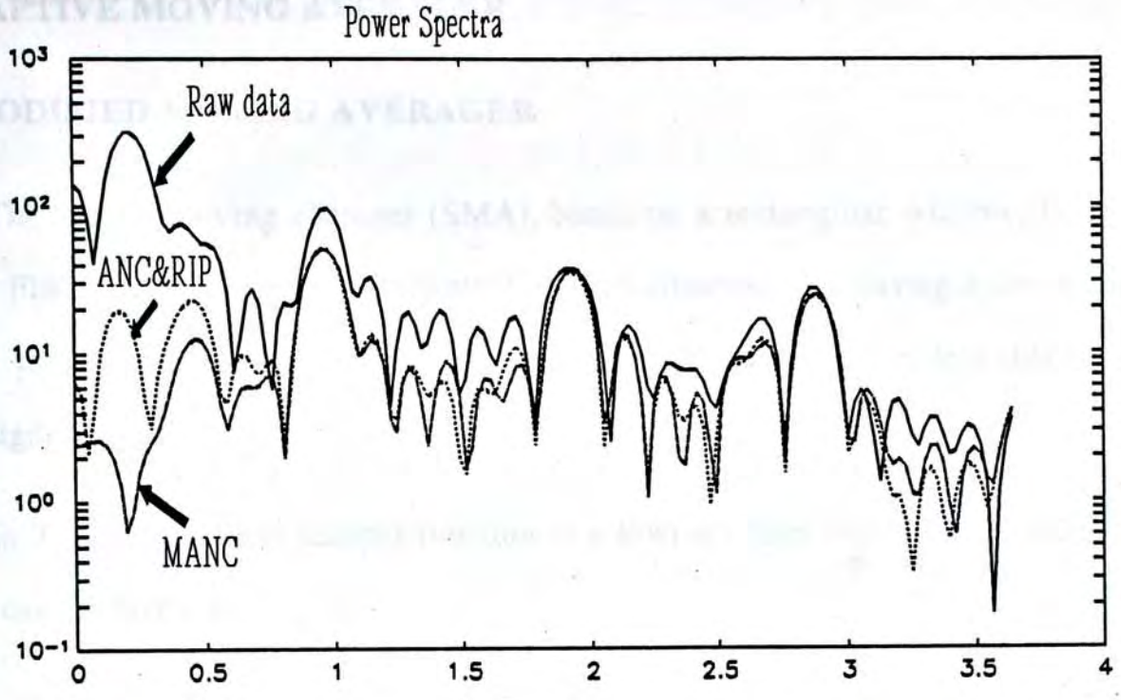

Figure 4.9 Results in power spectrum plots. The MANC method demonstrates larger artefact reduction than the ANC&RIP method within the frequency range of the respiratory component (0.1-0,6 Hz).

4.4 ADAPTIVE MOVING AVERAGER

4.4.1 MODIFIED MOVING AVERAGER

The simple moving averager (SMA), based on a rectangular window, is one of the simplest FIR filter with equal coefficients. It has the advantages of having a simple algorithm and fast processing time. Moreover, its zero phase response provide less distortion in its output signal.

In Z-Transform, the transfer function of a lowpass filter implemented with the SMA method can be given as

$$H(z)=\frac{1}{N}\frac{z^{(N/2-1)}-z^{-N/2}}{1-z^{-1}} \tag{4.6}$$

The corresponding frequency response is

$$H(e^{jw})=\frac{\sin(\omega N/2)}{\sin(\omega/2)} \tag{4.7}$$

where N is the moving window length. The adjacent sidelobe of the window transform is only a weak function of N and corresponds to about -13dB, regardless of how large N is. This is the drawback of the moving averaging method which has rather significant stopband ripples.

Recursive use of the SMA can decrease the amplitude of the stopband ripples but at the same time, amplitude of the passband ripples increases. In this study, a modified moving average (MMA) lowpass filter based on multiple use of SMA is proposed. This modified scheme, introduced by Kaiser and Hamming, has the transfer function

$$G(z)=H^2(z)(3-2H(z)) \tag{4.8}$$

Let δ_1 and δ_2 be the peak passband and stopband ripples of the SMA, it can be shown that $G(z)$ has peak passband error of about $3\delta_1^2$ and peak stopband error of about $3\delta_2^2$(=-30dB). *So the ripples of both the passband and stopband of the modified moving average*

filter are reduced in a squared scale compared to that of the SMA and are smaller than those of triply recursive SMA which has passband and stopband ripples of $3\delta_1$ and δ_2^3 respectively. The improvement can be observed in the filter's characteristic frequency response shown in figure 4.10.

4.4.2 RESPIRATORY ARTEFACT ELIMINATION WITH ADAPTIVE MMA

To remove the respiratory artefact, a highpass filter based on the MMA is developed by subtracting the output of the lowpass filter from the original signal, which has a transfer function of $F(z)=1-G(z)$ as shown in figure 4.11. Its cutoff frequency is determined by the moving window length N, i.e., a small N will produce a higher cutoff frequency and vice versa.

The selection of a moving window length N is based on the following deduction. The original signal $x(n)$ is composed of a respiratory artefact signal $a(n)$ and a rheopneumographic signal $r(n)$, i.e., $x(n)=a(n)+r(n)$. If the rheopneumographic signal $r(n)$ is a truly periodic signal, then averaging $x(n)$ over the range of one cardiac cycle gives an output signal free of the rheopneumogram (zero mean assumed) so that an approximated respiratory signal is obtained.

However, the human cardiac cycle has a somewhat varying harmonic content over cycles. The variation can be up to about 5 percent for normals under unexcited condition and 10 percent or even higher for certain cardiac patients. An improvement scheme to reduce the signal distortion proposed is to vary the moving window length N dynamically over the cycles from the knowledge of the spectral information calculated continuously in realtime via the short time DFT technique so that the modified moving-averaging filter can continuously adjust its cutoff frequency for optimal residual distortion. Figure 4.11 shows the structure of the adaptive MMA filter.

4.4.3 PERFORMANCE OF THE ADAPTIVE MMA FILTER

The performance of the filter can be evaluated more generally in terms of the signal-to-noise ratio improvement (*SNRI(z)*) and the signal distortion ratio (*SDR(z)*) of the output signal spectrum. Let the rheopneumographic signal $r(n)$ be the sum of a periodic component $p(n)$ and an irregular one $i(n)$, i.e., $r(n)=p(n)+i(n)$. At the filter input, the spectrum of signal to noise ratio $SNR_{input}(z)$ is defined as

$$SNR_{input}(z) = \frac{power\ spectrum\ of\ rheopneumogram}{power\ spectrum\ of\ respirogram} = \frac{\delta_{rr}(z)}{\delta_{aa}(z)} = \frac{\delta_{pp}(z) + \delta_{ii}(z)}{\delta_{aa}(z)} \qquad (4.9)$$

and at the output, the $SNR_{output}(z)$ is

$$SNR_{output}(z) = \frac{\delta_{signal\ output}(z)}{\delta_{noise\ output}(z)} = \frac{\delta_{pp}(z)+\delta_{ii}(z)|F(z)|^2}{\delta_{aa}(z)|F(z)|^2} \qquad (4.10)$$

So the *SNRI(z)* can be obtained as

$$SNRI(z) = \frac{SNR_{output}(z)}{SNR_{input}(z)} = \frac{\delta_{pp}(z)+\delta_{ii}(z)|F(z)|^2}{(\delta_{pp}(z) + \delta_{ii}(z))|F(z)|^2} \qquad (4.11)$$

If the output of the filter $G(z)$ is thoroughly free of the rheopneumogram, there is no distortion at all in the output of the filter. But if there still exists some residual rheopneumographic component in the output of $G(z)$, signal distortion may result. The amount of distortion depends on the amount of residual rheopneumographic components propagated through $G(z)$. Let *SDR(z)* be defined as a dimensionless ratio of the spectrum of the rheopneumographic output propagated through $G(z)$ to the spectrum of the input rheopneumographic signal. Thus

$$SDR(z) = \frac{\delta_{ii}(z)|G(z)|^2}{\delta_{pp}(z) + \delta_{ii}(z)} \qquad (4.12)$$

To assess the performance of the SMA and MMA, we assume that the rheopneumographic signal has a definite irregularity, i.e., $\delta_{pp}=R\delta_{ii}$, where R is an attenuation factor.

Figure 4.12 shows the simulated SNRIs of the SMA and the MMA filters with R equivalent to 5. The MMA method demonstrate a larger SNRI value in the frequency range of the respirogram (eg., usually in the range of 0.1-0.6 Hz) which means a better suppression of the artefact. Figure 4.13 shows the SDRs with R equivalent to 5 and 10 of the SMA and adaptive MMA filters. The SDR of the MMA in the frequency range of the artefact is a little larger than that of the SMA, but smaller in the frequency range of the rheopneumogram (eg., usually in the range of 0.6-1.5 Hz).

4.4.4 RESULTS AND DISCUSSIONS

To test the performance of the adaptive MMA filter, it was implemented in C language on a 486 PC-based data acquisition system. As the significant spectral components of the TIS do not extend beyond 10 Hz in general, an adopted sampling rate of 100 samples/second is more than sufficient for the A/D conversion. With this sampling rate, the speed of the 486 is fast enough to process the signal in realtime since the 486 can do multiplications of no less than 10^6 times per second and the calculations required for the adaptive MMA is only of the order of N with fast algorithms. For multi-channel applications or when dealing simultaneously with signals of higher spectral content, the filter can be implemented via DSP accelerators such as TMS32010.

Figure 4.14 gives an example of the raw and processed data. To compare the reduction of the artefact and the rheopneumographic signal distortion, the power spectra of the raw data and processed data of the SMA and adaptive MMA are calculated and shown in figure 4.15. In both the time and frequency domains, the performance of the adaptive MMA method is superior to that of the SMA method.

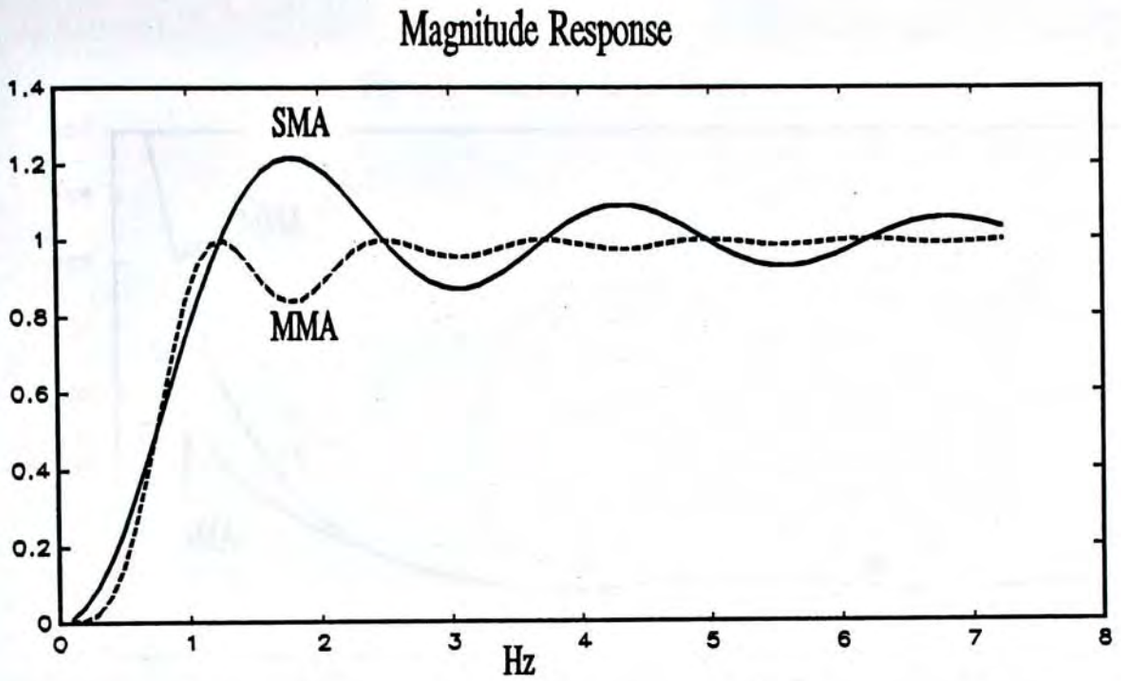

Figure 4.10. The frequency responses of MA and MMA filters

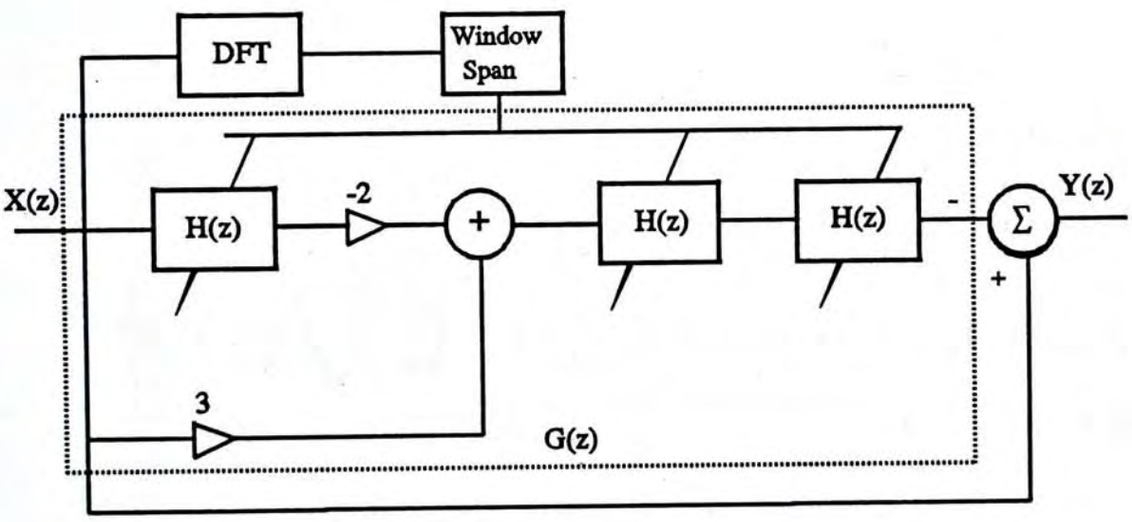

Figure 4.11. The structure of MMA filter where H(z) is the transfer function of SMA.

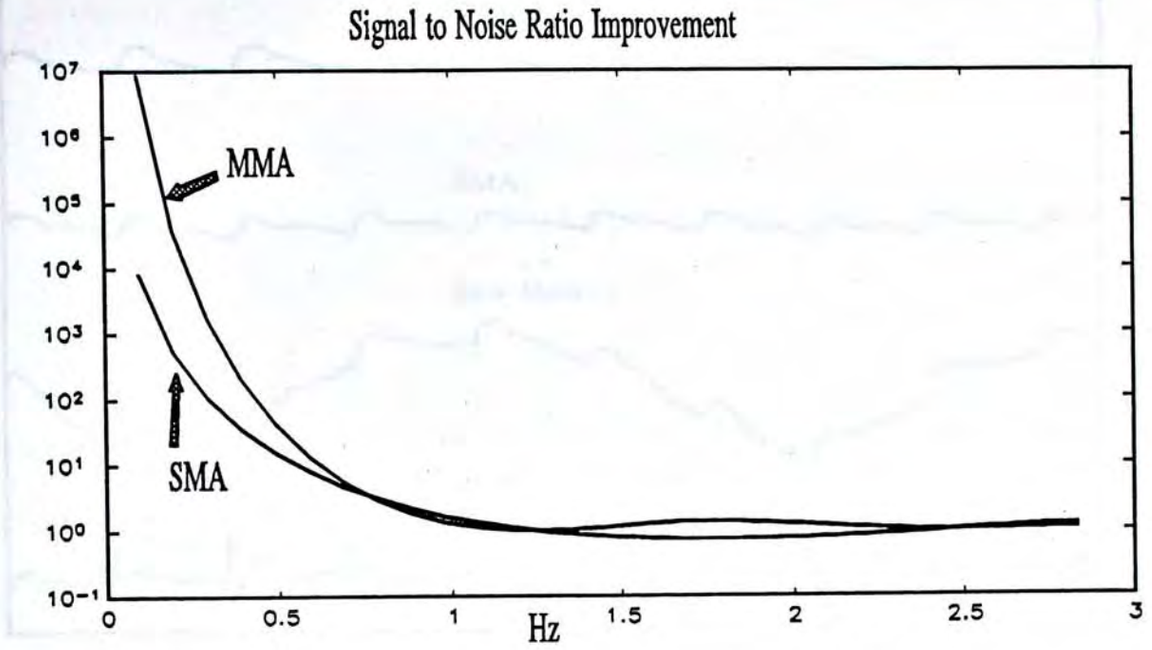

Figure 4.12. Plots of SNRIs with R=5.

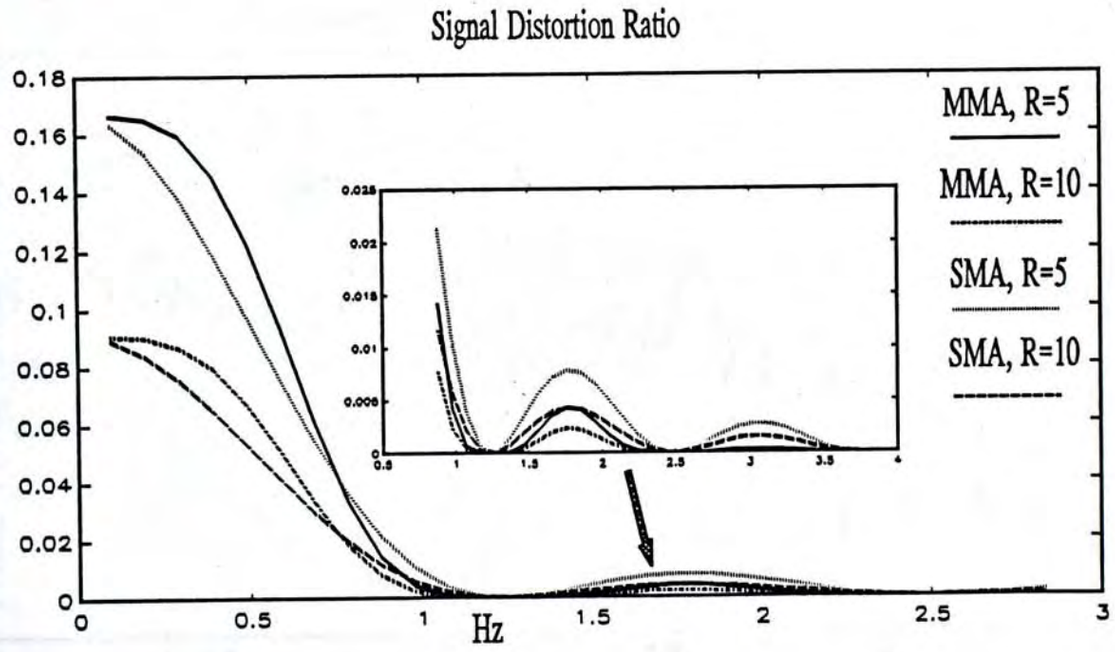

Figure 4.13. Plots of SDRs

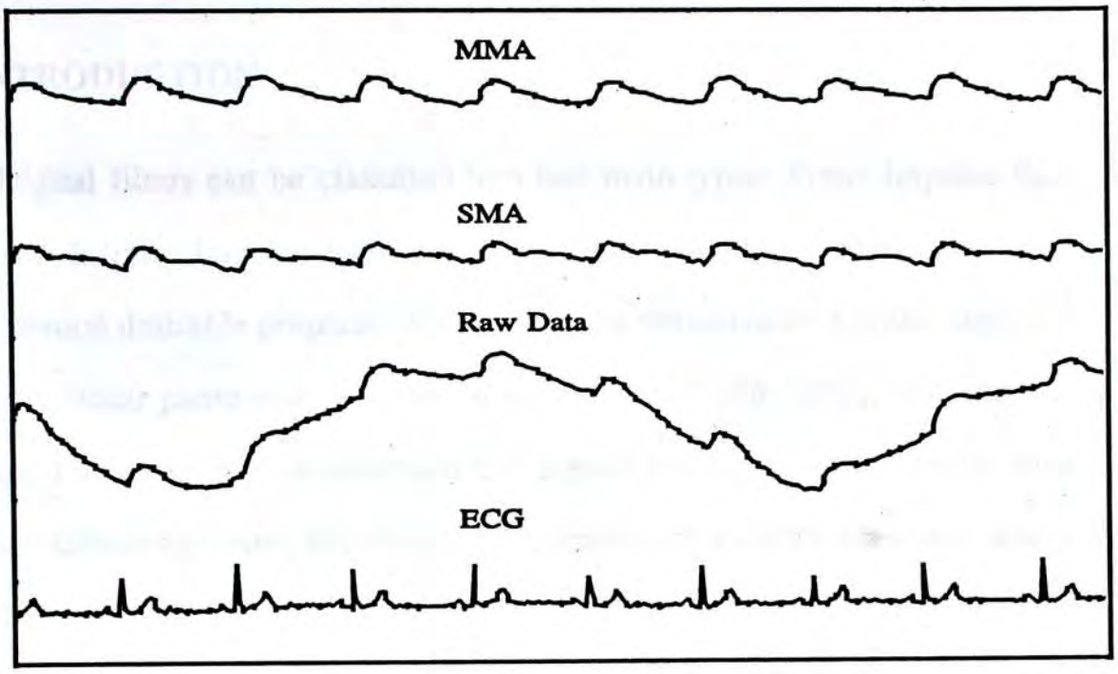

Figure 4.14. Raw and processed data of MMA and SMA along with the ECG waveform as the time maker.

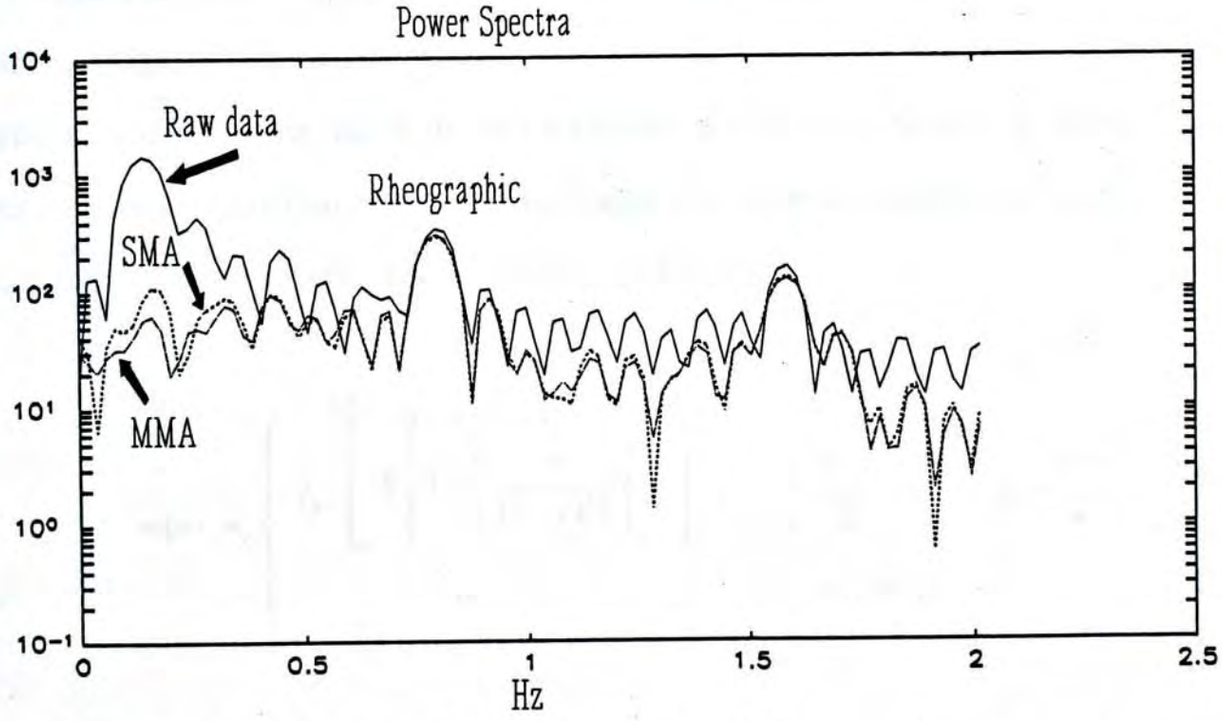

Figure 4.15. The power spectra of raw and processed data

4.5 ADAPTIVE FIR FILTER DESIGN

4.5.1 INTRODUCTION

Digital filters can be classified into two main types: Finite Impulse Response (FIR) filters, and Infinite Impulse Response (IIR) filters. Finite impulse response digital filters possess several desirable properties that make them attractive for a wide range of applications. An exactly linear phase-response can be achieved with FIR filters, with the result that they can be used in the faithful reconstruction of signals without phase distortion. In addition, FIR filters are inherently state, and hence the question of stability does not arise either in the design or in the implementation of these filters. This is very attractive in such applications as to biomedical signals, which require the filter coefficients to be varying with time. Moreover, even though FIR filter typically requires higher order, it can usually be realized by implementing the convolution sum efficiently with Fast Fourier Transform (FFT) algorithms. Furthermore, recent publications show that under most practical situations FIR filters of high orders can be implemented efficiently by indirect design approaches.

The FIR filter was chosen as the heart of this adaptive filter design together with a Kaiser window[1]. This window, based on discrete time approximations of the prolate spheroidal wave function, has a flexible parameter β which can be readily chosen to meet a given stopband attenuation and a window length N to meet the requirement specified by the transition bandwidth Δf. The Kaiser window is defined as

$$w(n) = \begin{cases} I_0\left[\beta\sqrt{1-\left[\dfrac{n}{(N-1)/2}\right]^2}\right], & -\dfrac{N-1}{2} \le n \le \dfrac{N-1}{2} \\ 0 & \textit{otherwise} \end{cases} \qquad (4.13)$$

[1] The introduction of FIR filter design is based on Elliott D. F., *Handbook of Digital Signal Processing*, ([ELLI 87]).

where $I_0(x)$ is the modified zeroth-order Bessel function, which can be computed easily as

$$I_0(x) = 1+\sum_{k=1}^{\infty}\left[\frac{(x/2)^2}{k!}\right]^2 \tag{4.14}$$

A lowpass filter with equal passband and stopband peak ripples A_r can then be designed by choosing

$$\beta = \begin{cases} 0.1102(A_r-8.7) & \text{if } A_r > 50\ dB \\ 0.5842(A_r-21)^{0.4}+0.07886(A_r-21) & \text{if } 21 < A_r < 50\ dB \\ 0 & \text{if } A_r < 21\ dB \end{cases} \tag{4.15}$$

The window length N (i.e., the filter order) can be estimated in terms of the desired specifications for Δf and A_r, viz

$$N = \frac{A_r-7.95}{14.36\Delta f}+1 \tag{4.16}$$

both of which can be readily computed. Thus, given the specifications in terms of A_r, ω_c (cutoff frequency), and Δf, the filter coefficients can be computed as follows:

(1) β and N from Equations (4.15) and (4.16)

(2) window coefficients $w(n)$ from Equation (4.13)

(3) filter coefficients from $h(n)=h_d(n)w(n)$, where $h_d(n)$ is

$$h_d(n) = \frac{\omega_c}{\pi}\left[\frac{\sin\omega_c n}{\omega_c n}\right], \quad -\infty \le n \le \infty \tag{4.17}$$

4.5.2 ADAPTIVE FIR FILTER

For the adaptive FIR filter design, a filter structure as shown in figure 4.16 was used. Short time DFT is applied to the raw data to obtain the instantaneous spectrum. The cutoff frequency is determined by analyzing the spectrum to select a frequency which can better separate the rheopneumogram and the respirogram. Instead of computing each time the values

for β, N and $h(n)$, a look-up table provides the suitable values with which the various tap weightings are set, thus achieving a tremendous saving in computation time. This fast processing speed via the use of a lookup table for the coefficient settings enables the whole design to operate in realtime mode which makes realtime monitoring of the artefact-free rheographic signal possible.

If a filter has a specified passband peak ripple of -39db and a transition bandwidth of less than 0.01 Hz, the corresponding β and filter order are 3.178 and 210 respectively and these, together with the cutoff frequencies ω_c (which will be determined from a local minimum preceding the rheographic peak in real time processing) and formula (4.13) and (4.17), enable the filter coefficients to be computed. If a still narrower transition bandwidth is required, a filter order of 256, with a corresponding transition bandwidth of 0.008 Hz which is more than sufficient for most situations, can be used. The CLT structure of such a filter is presented in table 4.1.

4.5.3 RESULTS AND DISCUSSIONS

The raw and processed impedance signals of a typical normal subject are shown in figure 4.17, and their power spectra in figure 4.18. Closer examination of the spectral amplitudes at around 0.9 Hz, where the rheographic fundamental is located, and beyond shows the effects of the filter order and ripples in the passband. The performance of the AFIR filter can be improved accordingly by increasing the parameter β and the filter order N as shown in figure 4.19. However, in so doing the computation time will be increased. A given processing speed of the computing system involved hence determines the ultimate tolerable distortion. In general, a distortion ratio of 10 percents or less is acceptable for realtime monitoring purposes. A guaranteed completely undistortive resulting rheographic signal is very unlikely since even for a normal ratio of 1 to 4 for the respiratory rate to cardiac rate, the fourth and higher harmonics of the respiratory signal are inbanded in the rheographic signal.

To investigate how much the rheographic waveform may be distorted, we had

analyzed the power spectra of the impedance signals of more than 30 subjects. A RIP signal was used as a reference of the respiratory wave and the attenuation factor (Respiratory Attenuation Factor) of its higher harmonic in the vicinity and beyond the rheographic fundamental was calculated. With the attenuation factor, the ratio of the respiratory component to the rheographic component (Respiratory/Rheographic Ratio) in the TIS at and beyond the rheographic fundamental can be obtained as an estimate of the filtering effect. Results of this statistical analysis as shown in figure 4.20 shows that the Respiratory Attenuation Factor in the frequency range of the rheographic signal is below 1 percent in most cases. Similarly, apart from a few cases, the Respiratory/Rheographic Ratio is confined also to about 10 percent.

For respiratory attenuation ratio exceeding 10 percent, result of using the AFIR filter has no appreciable improvement. This happens when a steady breathing pattern cannot be maintained and as a result the respiratory spectrum becomes very much richer in the higher harmonic contents. As this often appears in very short term modes, fast tracking and separation of the inbanded components become an impossibility. Figures 4.21 and 4.22 show a typical example of such a case in which the signal belongs to a rather serious pneumonic patient. In this case, the filtered result is less than marginally satisfactory over a small portion of the recorded strip. Result with the ANC method is even worst.

Table 4.1. The Coefficient Look Table (CLT) (100 Hz sampling Rate)

Cutoff Freq.	C_1	C_2	C_3...	C_{128}	C_{129}...	C_{256}
0.4	0.031	0.021	0.011...	992.0	992.0...	0.031
0.5	.	.	.	.	.	.
0.6	.	.	.	.	.	.
0.7	.	.	.	.	.	.
0.8	.	.	.	.	.	.
0.9	-0.331	-0.333	-0.333...	982.0	982.0...	-0.331
1.0	.	.	.	.	.	.
1.1	.	.	.	.	.	.
1.2	.	.	.	.	.	.
1.3	.	.	.	.	.	.
1.4	.	.	.	.	.	.
1.5	0.195	0.239	0.285...	970.0	970.0...	0.195

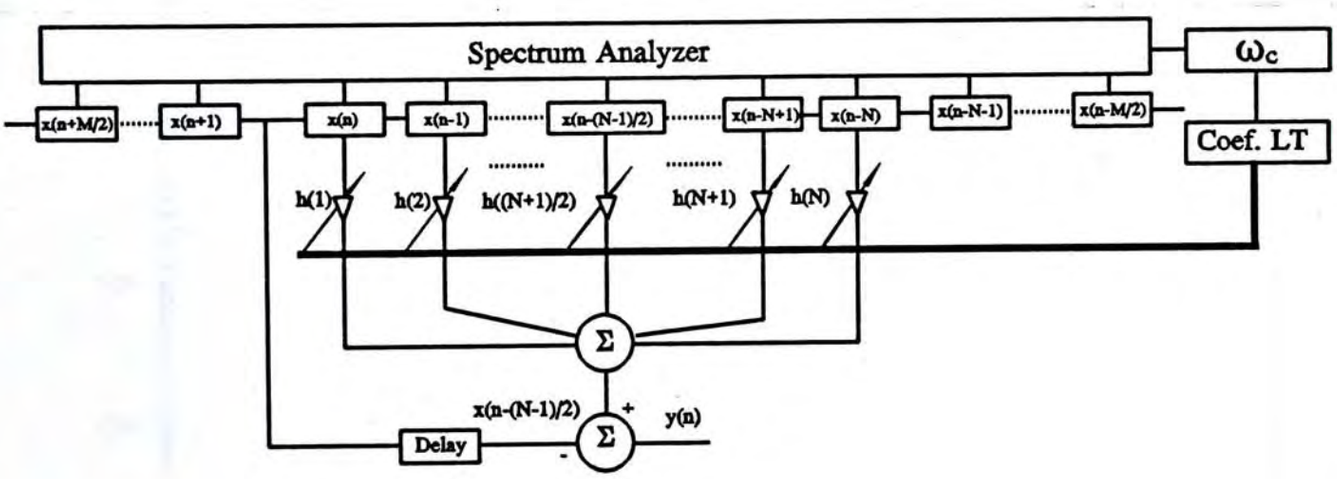

Figure 4.16. Structure of the adaptive FIR filter.

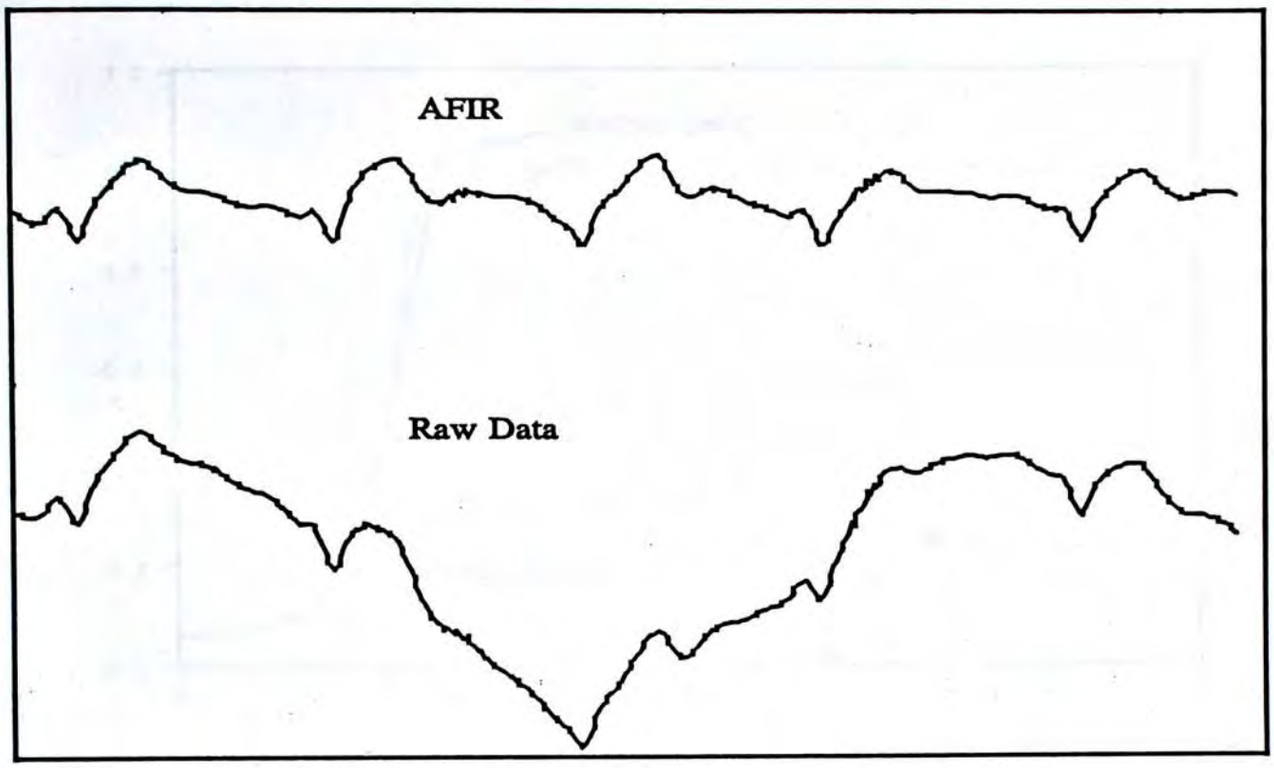

Figure 4.17. Raw and processed data of a normal subject.

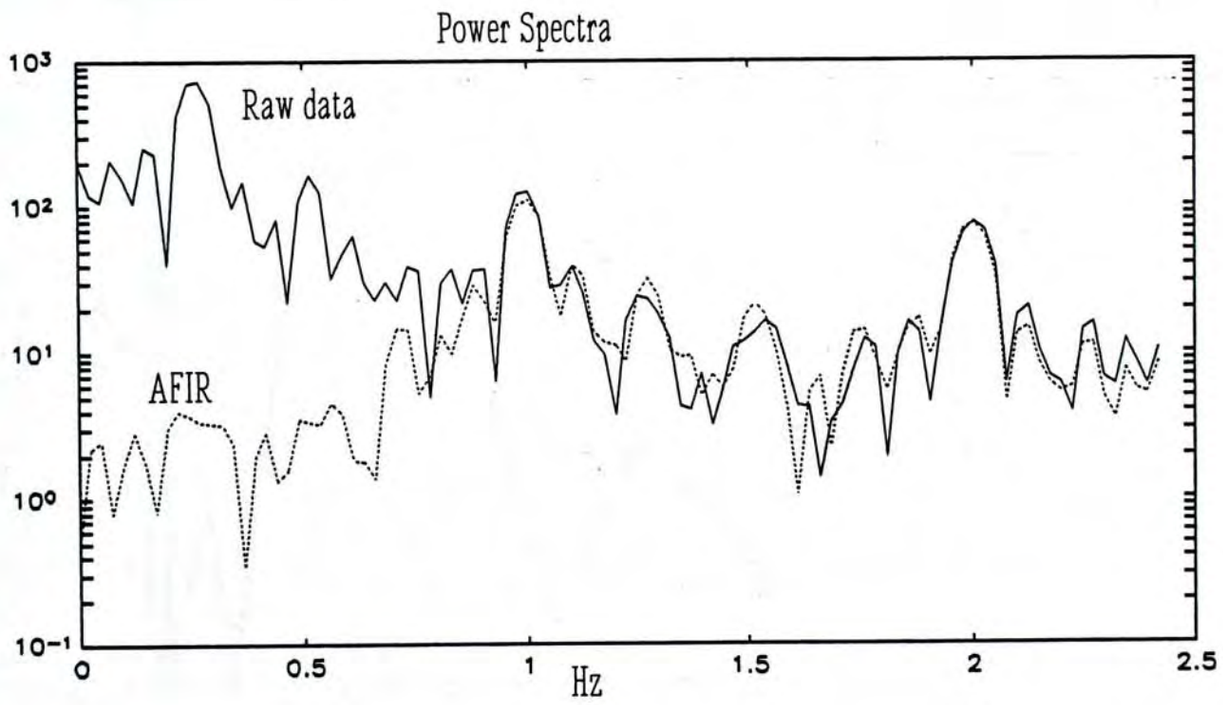

Figure 4.18. Power spectra of raw and processed data.

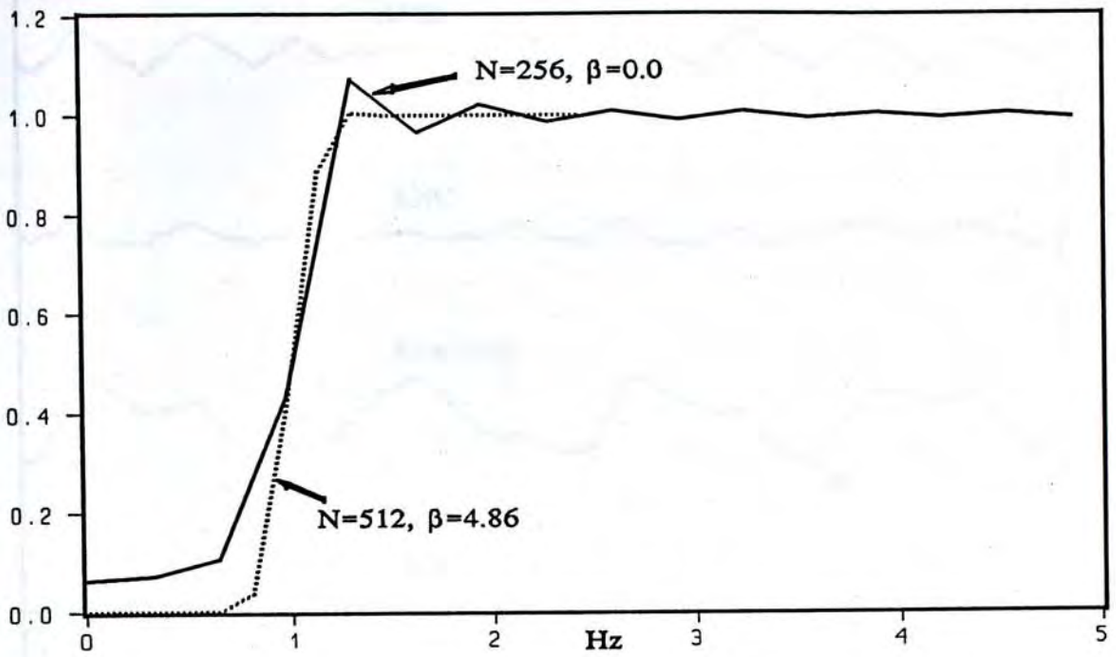

Figure 4.19. Frequency response of the FIR filter with different filter orders and β values.

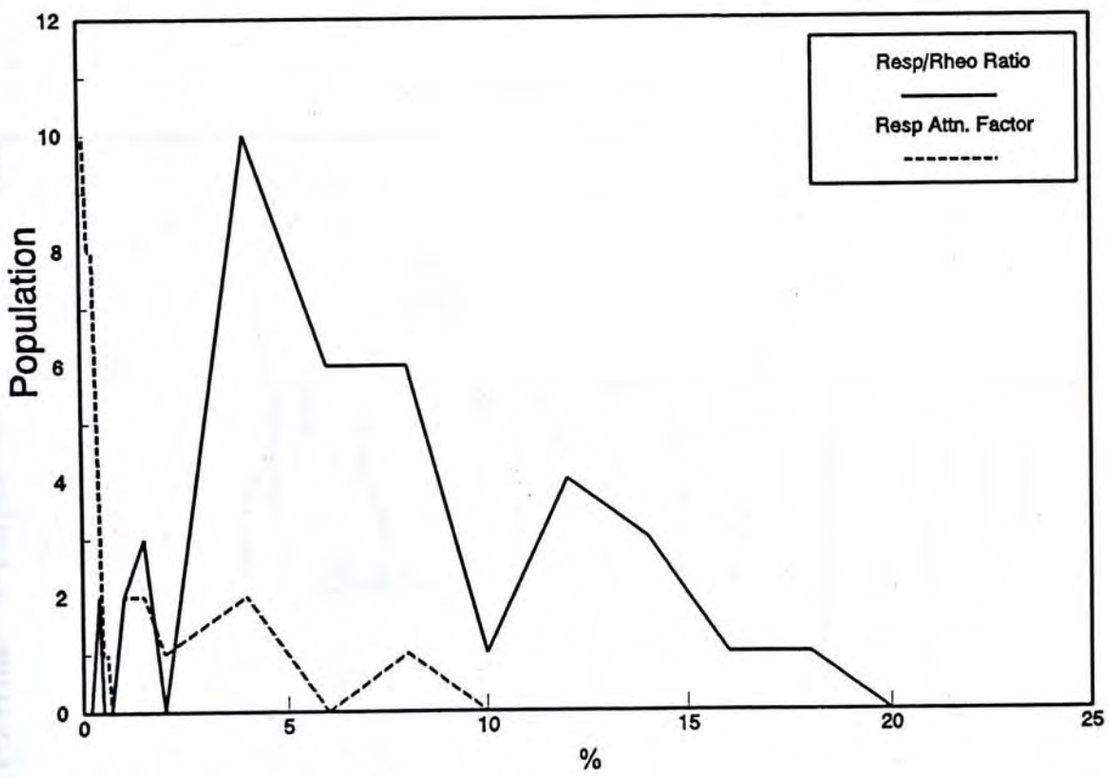

Figure 4.20. Distributions of Respiratory/Rheopneumographic ratio and Respiratory Attenuation Factor in the rheopneumographic frequency range (0.7-1.6 Hz) statistically analyzed from 30 subjects.

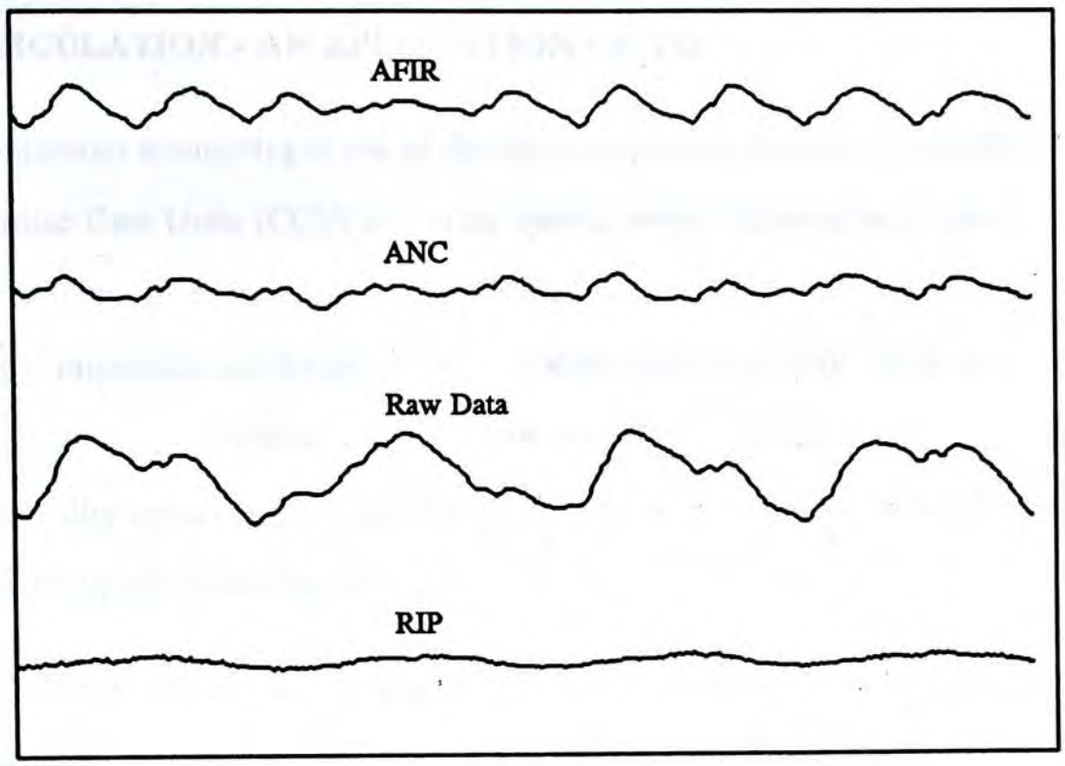

Figure 4.21. Example of a difficult case - serious pneumonic patient. Raw signal is shown along with processed (by AFIR and ANC) data and respiratory reference (RIP).

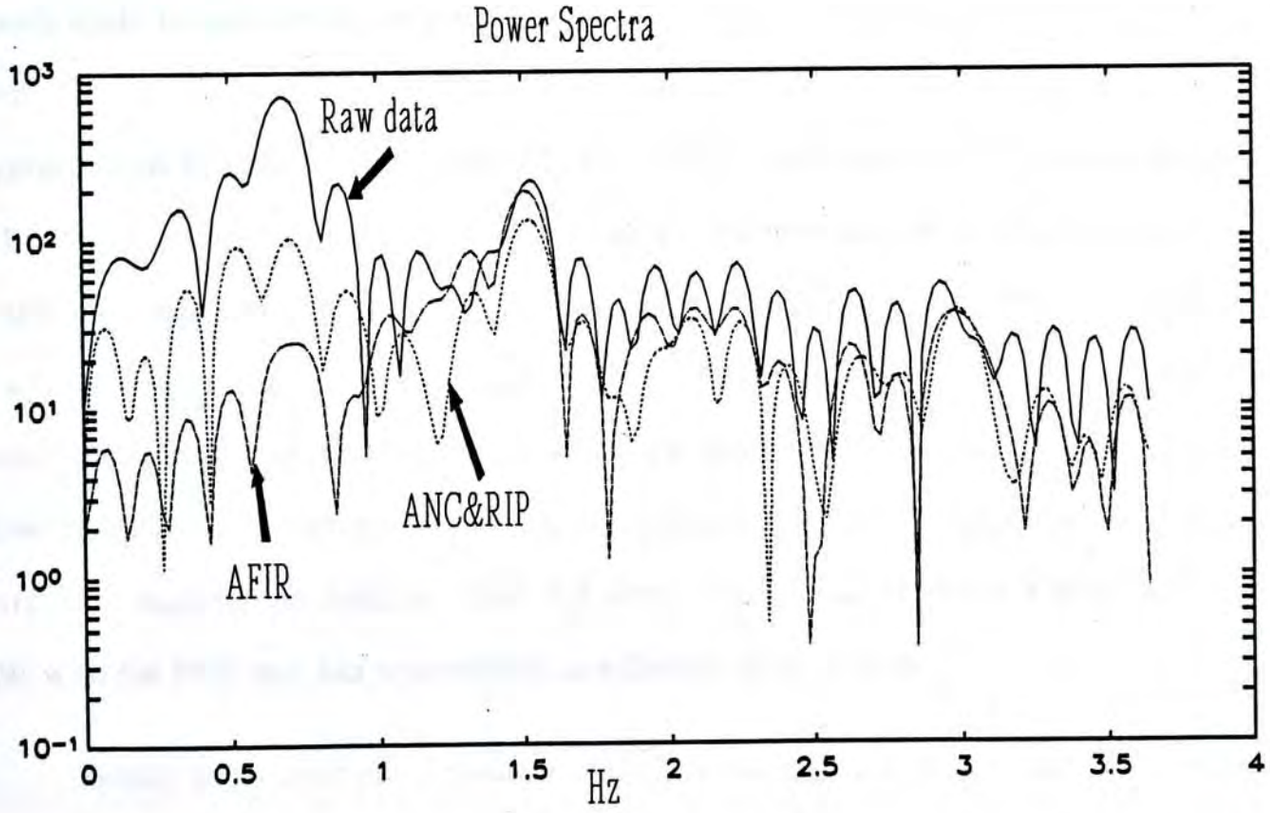

Figure 4.22. Power spectra of raw and processed data of the same patient (of figure 4.21).

4.6 SIMULTANEOUSLY MONITORING RESPIRATION AND PULMONARY CIRCULATION - AN APPLICATION OF TIS

Continuous monitoring is one of the common practice adopted in Intensive Care Units (ICU), Cardiac Care Units (CCU) and other special wards. Respiration monitoring, a typical example of such, is carried out via different methods, eg., thermistor sensor, bilateral transthoracic impedance plethysmograph or ribcage/abdominal RIP. Such methods all have one common feature or limitation viz a single-modality monitoring capability. The concept of multi-modality monitoring is desirable in clinical monitoring but difficult in view of the complexity of signal processing involved.

By applying the respiratory artefact removal techniques discussed in previous sections, a multi-modality physiological monitoring scheme via the EBI technique is presented which enables one to achieve the respiratory and the pulmonary circulatory signals (ie., the rheopneumogram) simultaneously. Figure 4.23 shows the scheme and the electrode placement.

In order to investigate whether the respiratory signal (Resp_TIS) detected by the transthoracic impedance technique can reflect the respiration or not, we have correlated the Resp_TIS to the respiratory signals measured by other techniques such as the rib-cage/abdomen RIP and the pneumotachograph (PNT). Although the PNT is commonly used and has long been accepted as the sort of standard in exercise ventilatory studies, its usage of real time monitoring is limited because the measurement method includes a combination of a face mask or mouthpiece-nose clip assembly which is likely to induce some degree of anxiety and discomfort and invariably introduce abnormal respiratory pattern. Figure 4.24 shows the raw TIS waveform along with Resp_TIS, RIP and PNT waveforms. The results of correlation analysis are listed in Table 4.2 which shows that the Resp_TIS correlates quite well with the PNT and has a correlation coefficient close to 0.90.

Finally as an example of multi-modality monitoring, a typical result of the separated respiratory and rheopneumographic signals of a normal subject is shown in figure 4.25 along with the raw TIS and PNT waveforms.

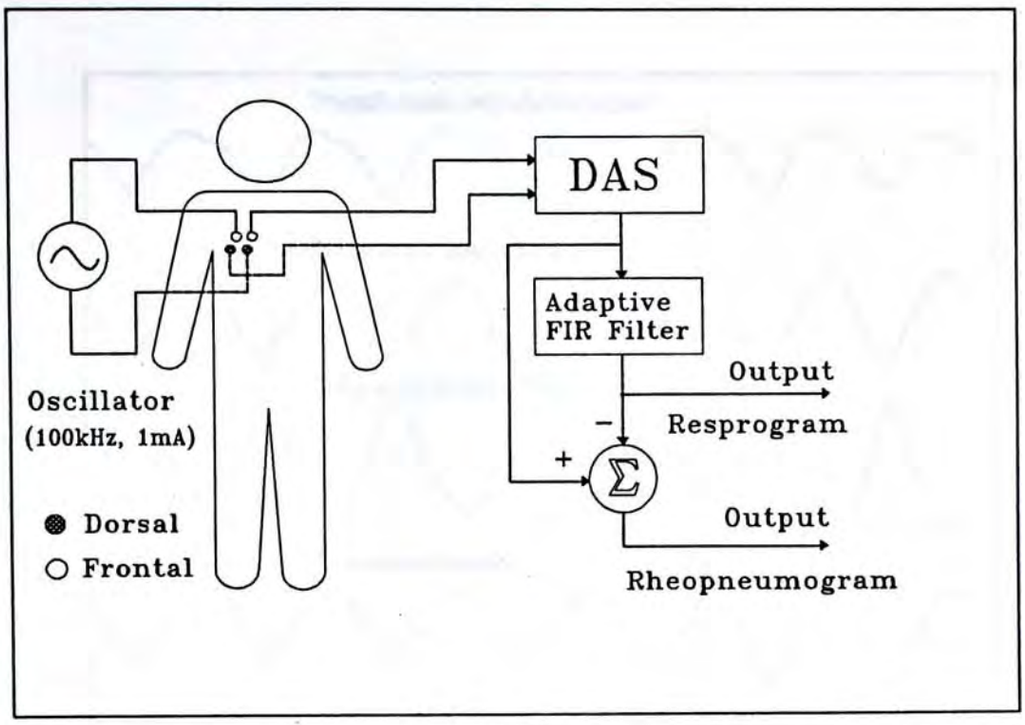

Figure 4.23 The diagram of the multi-modality monitoring system.

Table 5.2 The correlation coefficients

Corr. Coef.	TIS	Resp_TIS	RIP	PNT
TIS	1.0	0.9297	0.8560	0.8869
Resp_TIS		1.0	-0.8038	0.8177
RIP			1.0	-0.9115
PNT				1.0

where TIS is the transthoracic impedance signal; Resp_TIS, the respiratory signal processed from the TIS; RIP, the respiratory inductance plethysmogram; PNT, the pneumotachogram.

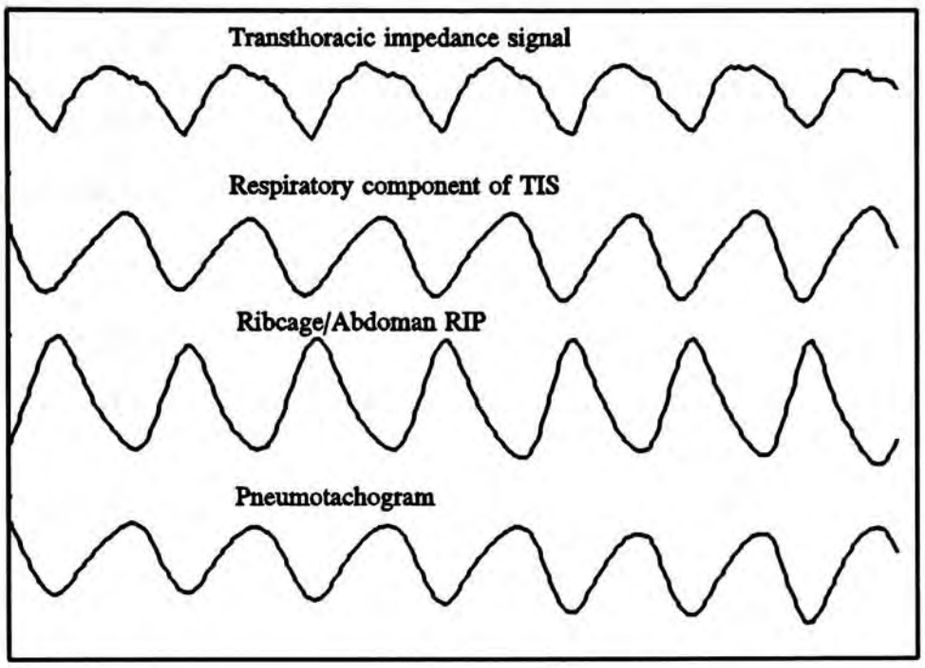

Figure 4.24 Respiratory signals obtained from TIS, RIP, and PNT. The RIP is in inverse phase with other signals because it is positively proportional to the air volume change and others are negatively proportional to the air volume change in the lung.

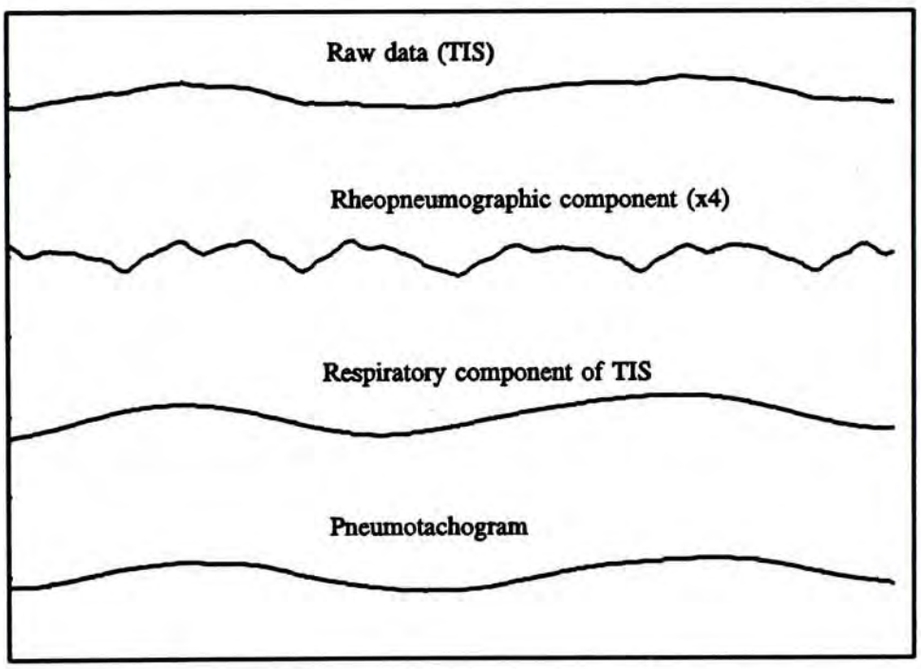

Figure 4.25. Raw and processed data along with a pneumotachogram. The resulted rheopneumogram is amplified four times in order to be observed easily.

4.7 COMPARISONS OF THE PROPOSED FILTER SCHEMES

Since 1988, several on-line artefact removal techniques have been studied and developed in our BME laboratory. These include, an adaptive noise canceller with the artefact reference obtained from RIP (ANC&RIP), a modified ANC with the artefact reference input obtained via applying a moving averager to the transthoracic impedance signal, an adaptive moving averager with variable window span adaptive to the cardiac cycle length, and finally an adaptive FIR filter based on a coefficient lookup table concept.

4.7.1 PERFORMANCE OF THE FILTERS

To compare the performance of these filters, a computer simulation was carried out to process an TIS waveform measured from a normal subject. Figures 4.26 and 4.27 show the results of all the methods in time and frequency domains respectively. Of all the methods, the AFIR presents the largest reduction of the respiratory artefact and the least distortion to the rheopneumogram.

In addition, the results were compared with the rheopneumogram recorded in apnea state of the same subject via the correlation analysis. The correlations were carried out respectively over a cardiac cycle and a respiratory cycle. The correlation conficients are shown in the table 4.3. Among all the filters, the AFIR method has the largest correlation coefficient and following by the MMA method. These results are quite compatible to figure 4.27 where the latter shows that the AFIR has the least signal distortion in the rheo-pneumographic frequency range. Both of the ANC methods have smaller correlation coefficients presenting larger signal distortions as shown in figures 4.26 and 4.27.

All correlation coefficients decrease when they are calculated over a respiratory cycle with respect to those calculated over only a cardiac cycle. However, the correlation coefficients of AMA and AFIR are still close to 0.90. But those of ANC methods decrease to around 0.50, which can be explained in view of the finite converging time of the LMS algorithm and hence it can not keep convergence over a longer time period.

4.7.2 COMPUTATIONAL COMPLEXITY AND REDUCED SCHEMES

In the previous sections, the performance of the filters is evaluated in terms only of the SNR and SDR. However, the computation complexity is also a very important index for real time processing. In order to compare the computation complexity of all the methods proposed in this study, the numbers of multiplications and additions needed are listed in table 4.4 where N stands for the filter's order and M the length of DFT.

Among all the filters, the MANC method needs the least computations and AFIR the most. But after closer examination of table 4.4, we can see that most of the computations in AFIR and MMA is carried out for the calculation of DFT. Actually in practice of real time monitoring, it is not necessary to analyze the power spectrum for each input (i.e., sample by sample). A reduced implementation scheme can be accepted which monitors the signal power spectrum in an intermittently way, i.e., calculating short time DFT once within one or several cardiac cycles. Of course, this may lose tracking of some instant changes in the input signal and hence the adaptive filters may not be able to find the most suitable cutoff frequency. However, with the limitation of processing time, this is a compromise. Moreover, it is reasonable to do like this with consideration of the biomedical signals which do not change so fast. Therefore, the reduced scheme can be applied and hence greatly decrease the calculations for the AFIR and adaptive MMA. Table 4.4 also shows the calculations for the reduced schemes with N=128 and M=512.

Among the reduced schemes, the MMA method is the most preferable because of its fast processing and easy implementation. Its characteristics of suppressing the respiratory artefact and signal distortion ratio as presented in last section are also very close to those of the AFIR method but much simpler and faster in implementation than the latter.

Table 4.3 Correlation Coefficients

Filter	One cardiac cycle	One Respiratory cycle
AFIR	0.9918	0.8842
MANC	0.7135	0.5703
ANC&RIP	0.7668	0.4407
MMA	0.9894	0.8307

Table 4.4 Number of computations (In reduced scheme, the calculations of FFT are not counted).

	Theoretical		N=256 M=512		Reduced scheme	
Filter	Number of Multiplications	Number of Additions	Muls	Adds	No. Mul	No.-Add
SMA	1	N	1	256	1	256
MMA	$M/2*\log_2(M/2)+1$	$M*\log_2 M+N-1$	2049	4863	1	255
ANC&RIP	6N	6N	1536	1536	1536	1536
MANC	3N+1	4N	769	1024	769	1024
FIR	N/2	N-1	128	255	128	255
AFIR	$M/2*\log_2(M/2)+N/2$	$M*\log_2 M+N-1$	2304	4863	256	255

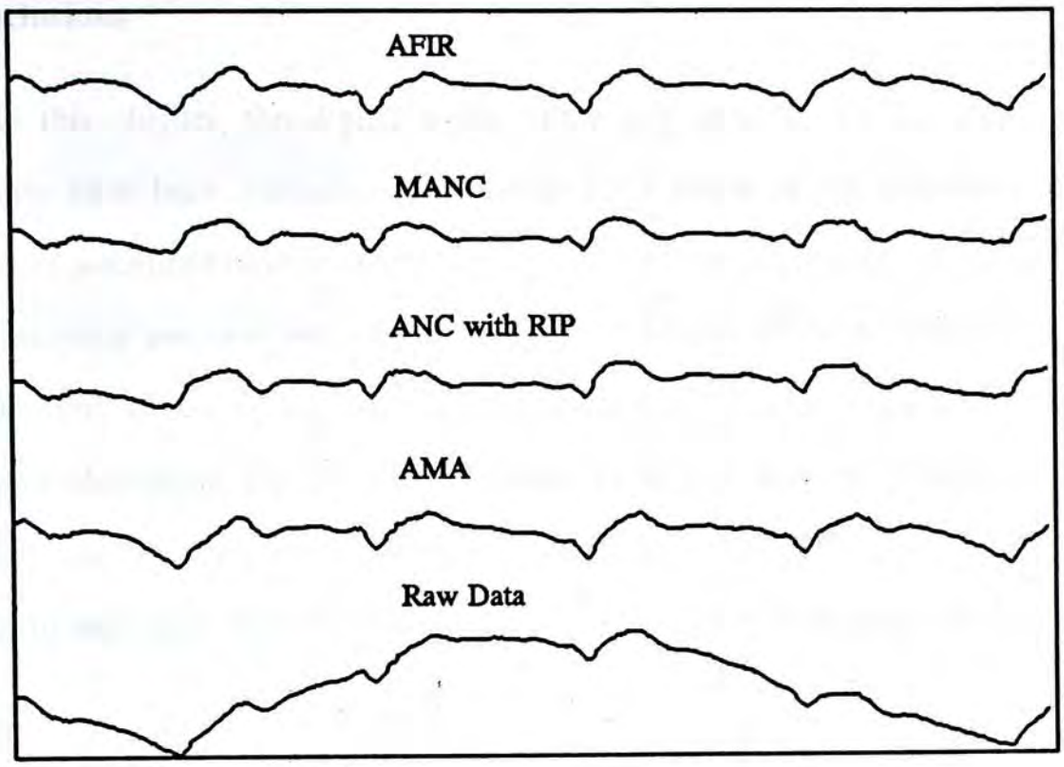

Figure 4.26 Data of raw and processed via the adaptive FIR filter, the modified ANC, the ANC with RIP respiratory reference signal and adaptive moving averager.

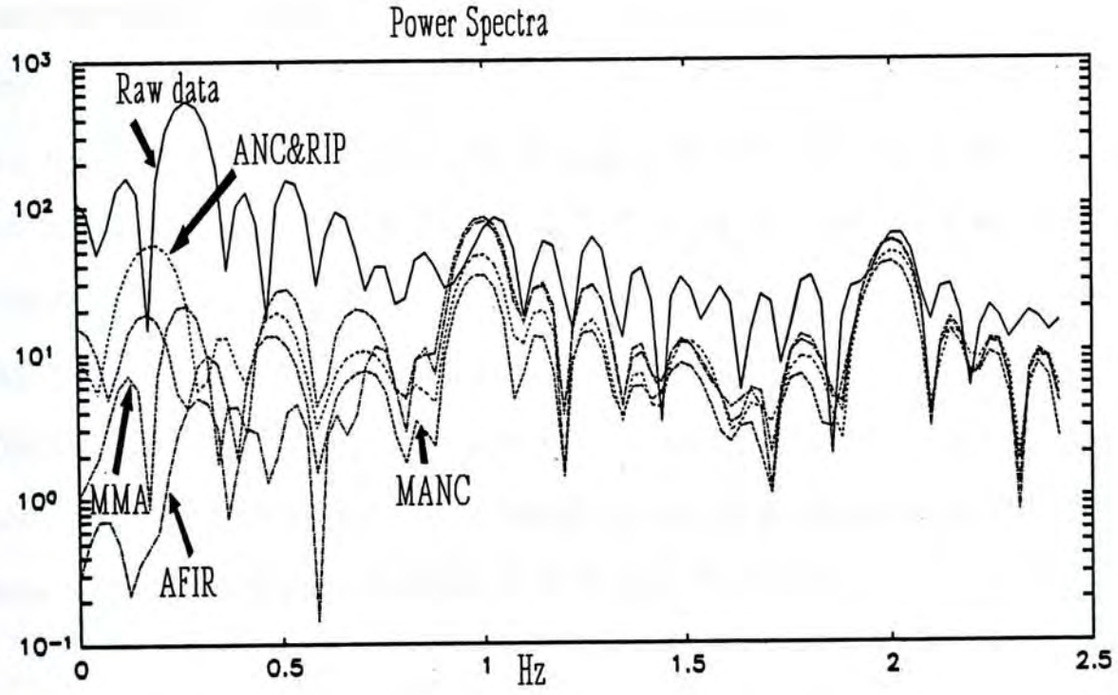

Figure 4.27 Power spectra of raw and processed data.

4.8 Conclusions

In this chapter, the digital signal processing methods for the respiratory artefact elimination have been studied. According to the features of the transthoracic impedance signal, more attentions have been paid on fast and on-line processing, viz the modified ANC, adaptive moving averager and adaptive FIR filter. Results show the respiratory artefact can better be eliminated with the adaptive FIR and MMA filters. It is necessary to study faster convergent algorithms for the ANC method so that it may be applied in the case of respiratory and rheopneumographic frequency overlap, while in such a case, the conventional low pass or high pass filter fails, even does the adaptive FIR proposed in the study.

4.9 NOTES ON PUBLICATIONS

A paper entitled "On-line Respiratory Artefact Removal in Rheopneumographic Measurement Via Moving Average Method" was presented at CMBES'92, Canada. Another paper entitled "On Line Respiratory Artefact Elimination in Rheopneumographic Measurement", was presented at ISSPA'92, Australia. Also, a paper entitled "Respiratory artefact elimination via adaptive FIR filter in rheopneumographic measurement" has been accepted and will be presented at SICON/ICIE'93, Singapore. A detailed version of this paper has been submitted to the journal Med. & Biol. Eng. & Comput. for consideration of publication. A paper entitled "On-line respiratory artefact removal in rheopneumographic measurement via an adaptive moving average method" has been accepted for publication in Electronic Letters. And finally a paper entitled "An EBI technique for simultaneous RT monitoring of respiration and pulmonary circulation" has been accepted and will be presented at FECMBE'93, Beijing. All these papers were jointly authored with Thomas T. C. Choy.

CHAPTER 5 MODELING ANALYSIS OF THE RHEOPNEUMOGRAM

5.1 INTRODUCTION

Electrical impedance rheopneumography (EIR) is defined as the measurement of the blood volume changes in the cardiopulmonary vessels. Since the pulmonary arteries and veins connect the two lungs to the relevant parts of the heart, any change in the physical conditions or dynamic behaviour of such parts can be reflected in the haemodynamics and vascular characteristics of these major pulmonary vessels. In particular, the volumetric variations at any section of these vessels due to the pulsatile action of the pulmonary circulation can be observed as corresponding variations in the rheopneumographic waveform.

Assessment of the EIR waveform has so far been based mainly on computation of the absolute, relative or ratiometric values of peak amplitude, time intervals or delays relative to some ECG or PCG landmarks ([WEGL 83] [LI 83a] [LI 92a]). As the physiological conditions or dynamic behaviour are not readily available from such assessed parameters, the etiopathology or at times the differential diagnosis is not too obvious. In fact, the composite EIR waveform observed cannot be resolved into its arterial and venous components with presently available techniques.

In view of this, a EIR modeling analysis method is presented, in which the pulmonary circulatory system is represented by a modified two-chamber model. Based on the composite wave theory, the model consists of two parts, viz arterial part and venous part. The model parameters are obtained by a two-stage identification approach and as a result, the measured rheopneumographic waveform is resolved into its arterial and venous components and corresponding model parameters can be obtained. These model parameters, reflecting the properties of the pulmonary circulatory system and related physiological pictures in terms of the blood vessel compliance, the blood inertance and the lung input impedance, can provide a better insight of the system concerned and hence may be more useful for clinical assessment than those of ratiometric values directly calculated from the waveform.

5.2 PULMONARY CIRCULATION MODELING

Many cardiovascular models have been developed and presented in the past ([BRUB 78] [CLAR 80] [BURA 82] [DAGA 82] [HARD 82b] [BOUR 83] [TOY 85]). These models can basically be divided into two categories, viz the lumped and distributed models for use for part of the cardiovascular tree or the entire circulatory system according to the purposes intended to serve. For the first kind of model, there are the famous "Windkessel" model and its many derivatives. In view of its simplicity, the lumped model is often preferred for applications in clinical diagnosis. However, since the circulatory system is not a lumped parameter system, more accurate models using distributed elements such as the transmission line model, are needed for better representation of the cardiovascular systems.

Correctly building up a model is very important. The parameters of the model must certainly reflect some properties of the real system and more important by, all unwanted or insignificant subsystems should be removed leaving a simplified model which is still sufficiently informative. Therefore, the resulted model should be detailed enough to account for the observed waveform morphology and simple enough to provide certain clinical useful data.

The EIR signal detected via the EBI technique is a global effect resulting from all the blood volume changes of the cardiopulmonary blood vessels including the pulmonary arteries and veins, the heart chambers and the capillaries. As this global result is a lumped effect, a two-chamber lumped model is proposed to be the heart of the EIR modeling. This model is a linear third-order modified "Windkessel" model with five elements similar in many aspects to those of Spencer and Denison ([SPEN 63]) and Godwyn and Watt ([GOLD 67]).

Moreover, our study on the composition of the EIR signal via a numerical model and the computer simulation technique (Chapter 3) shows that the principal origins of the EIR signal consist of mainly the larger vessels such as the major pulmonary arteries and veins. Contributions from the heart chamber contraction and aortic expansion may also be included but can be avoided by careful selection of the electrode positions. The blood volume

fluctuations resulted from the smaller vessels are not so significant and can almost be ignored as an approximation. With these considerations in mind, we can divide the cardiopulmonary system into two parts, viz the arterial part and venous part, and each part is represented by a modified two-chamber model.

The first or arterial part consists of the right ventricle and the lung connected by the pulmonary arteries. The right ventricle is regarded as a pump which injects blood into the lumped equivalence of the major pulmonary artery and its branches. The blood in the branches then discharges into the smaller vessels represented by a peripheral lung input resistance.

The second or venous part, similar to the arterial part, consists of the lung and the left atrium connected by the pulmonary veins. When the left atrium contracts, a reverse blood flow will produced and hence resulting in the a-wave. However, the main contribution of the venous part to the EIR signal is the back flow from the lung to the left atrium as the result of the pressure difference between the lung and the left atrium.

Here an assumption has been made which treats the contractions of the right ventricle and the left atrium as impulse sources. It is not true in practice and many improvements have been made based on the elastance concept ([GREE 73] [BUON 73] [BURA 83] [AVAN 85] [CAMB 86] [BERG 92]). However, because the pulmonary circulatory system acts as a load of the heart and assessing the properties of the former is only concerned in the EIR modeling analysis, this assumption is justified for the sake of simplicity. Even though this simplified EIR model is very crude, it is still useful and informative.

5.3 MODEL DEDUCTION

5.3.1 PRESSURE-FLOW IN ARTERIES AND VEINS

Arteries and veins may be assumed to be made up of cylindrical vessels with linearly elastic walls, and to a good approximation the blood that flows in them may be regarded as an incompressible fluid with simple Newtonian characteristics. An ideal segment of this kind

is shown in figure 5.2, where P_1 and P_2 are the pressures of the two ends of the segment; A, the area of the segment; Δz, the length of the tube and h, the thickness of the vessel wall.

Let us initially assume that the vessel wall is rigid, the force moving the blood in the segment is given by $(P_1-P_2)*A$. This force is balanced by the effects of fluid-flow resistance and of fluid-mass acceleration.

The resistance to the flow is given approximately by the poiseuille steady-state formula ([NOOR 78])

$$R=8\pi\mu\Delta z/A^2 \tag{5.1}$$

where μ is fluid viscosity. If the flow is assumed to be uniform across the diameter of the tube, the viscous resistance part of the pressure drop is given by

$$(P_1-P_2)|_{vis}=fR \tag{5.2}$$

and the force needed to balance the acceleration of blood is give by Newton's second law:

$$M\frac{dv}{dt} = (\rho A\Delta z)\frac{d(f/A)}{dt} \tag{5.3}$$

where $v=f/A$ is the blood flow velocity and M is the mass of the blood in the segment. This acceleration force must equal the acceleration part of the pressure difference times the cross-sectional area, thus

$$\begin{aligned}(P_1-P_2)|_{accel}&=(\frac{\rho\ \Delta z}{A})\ \frac{df}{dt}\\ &=L\frac{df}{dt}\end{aligned} \tag{5.4}$$

where $L=\rho\Delta z/A$ is defined as the blood inertance. The total pressure drop along the tube can be obtained by summing equation (5.2) and (5.4)

$$P_a - P_b = R\, f + L\, \frac{df}{dt} \tag{5.5}$$

5.3.2 THE TWO-CHAMBER MODEL

So far, we have neglected the elasticity of the vessel walls. It can be shown ([JAGE 65]) that the compliance C of a cylindrical vessel of radius r, length Δz, wall thickness h and Young's bulk modulus of elasticity E is

$$C = 3\pi r^3 \Delta z / (2\, E\, h) \tag{5.6}$$

However, the values of E and h are usually not available in practice, the compliance is usually determined by assuming that there is a constant linear relationship between the volume of the chamber and the net pressure in it, thus we have

$$V = V|_{unstretched} + C\, P \tag{5.7}$$

For a cylindrical blood vessel, the compliance C can be divided into two parts placed at each end of the vessel. These two parts can be represented by two elastic chambers connected with a rigid tube of blood forming a so-called two-chamber model as shown in figure 5.3. Let V_1 be the volume of the first chamber and V_2 the volume of the second chamber. Then we have

$$\begin{aligned} V_1 &= V_1|_{unstretched} + C_1 P_1 \\ V_2 &= V_2|_{unstretched} + C_2 P_2 \end{aligned} \tag{5.8}$$

where C_1 and C_2 represent the compliances of the two chambers respectively.

5.3.3 THE EIR MODEL

In the EIR modeling analysis, the pulmonary circulatory system can be simplified as composed of the heart and the lung connected by an elastic tube, where the heart is represented by a pump, the lung by a peripheral resistance and the blood vessel by a two-chamber model.

Since the EIR signal includes contributions mainly from the large vessels, the vascular resistance of these large vessels is very small compared to the lung input impedance (see equation (5.1)) so that they may be ignored for the sake of simplicity. With this assumption, the equation (5.5) can be simplified as

$$P_1 - P_2 = L\frac{df}{dt} \tag{5.9}$$

The blood flows in the two chambers are related by the following equation

$$f_{in} - f = \frac{dV_1}{dt} \quad and \quad f - f_{out} = \frac{dV_2}{dt} \tag{5.10}$$

Assuming that there is a constant linear relationship between the volume of the reservoir and the net pressure in it, one can write according to equation (5.8)

$$f_{in} - f = C_1\frac{dP_1}{dt} \quad and \quad f - f_{out} = C_2\frac{dP_2}{dt} \tag{5.11}$$

The blood discharging effect from the second chamber to the lung can be expressed as $f_{out}=P_2/R_0$, where R_0 represents the total lung input resistance into which the blood is discharged.

While the flow equations of EIR model could be handled by equations (5.9-5.11), it is convenient to consider the electrical analog of EIR model using the following analogies:

Physical Model	***Electrical Analog***
Flow rate f	Current i
Pressure P	Voltage V
Compliance C	Capacitance C
Mass equivalent L	Inductance L
Peripheral resistance R	Resistance R

Substituting the electrical analogies into equations (5.9-5.11) results in a set of equivlences,

$$\begin{aligned} &i_{in}-i=C_1\frac{dV_1}{dt}, \qquad i-i_{out}=C_2\frac{dV_2}{dt} \\ &L\frac{di}{dt}=V_1-V_2 \\ &R_0 i_{out}=V_2 \end{aligned} \tag{5.12}$$

For its arterial part of the EIR model, the equivalent electrical circuit is shown in figure 5.4. The right ventricle is treated as an impulse source (V_1) which squirts the blood into the pulmonary arteries. The R_i is the characteristic resistance of the impulse source; C_1 and C_2, the proximal and distal vessel compliancies; L, the blood inertance and R_0, the lung input impedance.

However, some modifications are necessary for the venous part. The pressure difference between the lung and the left atrium and the effects of mitral valve opening and closing must be taken into consideration. Figure 5.5 shows the circuit for the venous part, where V_2 stands for the pressure difference between the lung and the left atrium and R'_i has two forms corresponding to the closing or opening of the mitral valve, viz

$$R_i'=\begin{cases} R_i & t<td \quad (closing) \\ R_i e^{-\gamma(t-td)} & t\geq td \quad (opening) \end{cases} \tag{5.13}$$

where γ is a measure of the decay rate of the flow from the left atrium to the left ventricle after the mitral valve opening and t_d is the equivalent time lag of the mitral valve opening.

The superposition theorem is applied here as an approximation so that the venous output can be taken as the sum of the outputs resulted from the two sources, ie., the left atrium contraction and the pressure difference between the lung and left heart. For the first one, the output is just like that of the arterial part. But for the effect of the latter source, the circuit can be degenerated into a modified "Windkessel" model as shown in figure 5.6 if we ignore the blood inertial effect for the sake of simplicity. This assumption is reasonable

because the reverse flow from the lung is relatively steady compared to that arising from heart contraction.

5.4 PARAMETER ESTIMATION

Our objective of the modeling analysis is to achieve some indices from a measured rheopneumographic waveform. For this purpose, a fitting function is established from the inverse Laplace transform of the model output. The coefficients of the fitting function relate to the model parameters via a set of parameter equations, and these parameter equations can be solved with knowing the coefficients.

A two-stage parameter identification scheme is proposed to calculate the model parameters. The scheme first utilizes a non-linear curve fitting technique ([BROW 90]) to fit the fitting function to the measured rheopneumogram and then solves the parameter equations via the Gauss-Newton nonlinear method.

5.4.1 THE FITTING FUNCTION AND THE PARAMETER EQUATIONS

Output of the two-chamber model in response to an impulse input has a third-order solution with a Laplace transform given by

$$V_{c_2}(s)=\frac{\dfrac{V_1}{R_1LC_1C_2}}{s^3+\left(\dfrac{1}{R_iC_1}+\dfrac{1}{RC_2}\right)s^2+\left(\dfrac{1}{LC_1}+\dfrac{1}{LC_2}+\dfrac{1}{R_iRC_1C_2}\right)s+\dfrac{1}{RLC_1C_2}+\dfrac{1}{R_iLC_1C_2}} \quad (5.14)$$

To account for the possible recursive elastic recoil of the vessels subsequent to the pulsatile ejection, the inverse Laplace transform for the case of the two-chamber model with one real and two complex conjugate poles has been adopted to provide a time domain response function $v(t)$ as

$$v(t)=Ae^{-\alpha t}\sin^2(\beta t) \quad (5.15)$$

Equating the coefficients of equation (5.14) to those of the Laplace transform of equation (5.15), one gets the parameter equations for the two-chamber model as

$$\begin{aligned}
&\frac{V_i}{R_i LC_1C_2}=2A\beta^2 \\
&\frac{1}{R_iC_1}+\frac{1}{RC_2}=3\alpha \\
&\frac{1}{R_iRC_1C_2}+\frac{1}{LC_1}+\frac{1}{LC_2}=3\alpha^2+4\beta^2 \\
&\frac{1}{R_iLC_1C_2}+\frac{1}{RLC_1C_2}=\alpha^3+4\alpha\beta^2
\end{aligned} \tag{5.16}$$

Values of the circuit components can hence be solved in terms of the values of A, α and β in equation (5.16).

For the modified "Windkessel" model of the venous part as shown in figure 5.6, the output function is

$$v_{vy}(t)=\frac{V}{a_1+1}\left(1-e^{-(a_1+1)t/a_2}\right)u(t) \tag{5.17}$$

where $a_1=R_0/R'_i$ and $a_2=R_0(C_1+C_2)$.

According to the composite wave theory, the fitting function is the sum of the arterial and venous waves. Some reflection waves of the arterial wave have also been considered in view of the possible impedance mismatch in the arterial vessels. Whereas there are almost no reflections in the venous vessels, because they are more compliant and blood flows in them are more steady. Introducing the appropriate delays for each term and summing, the resultant fitting function becomes

$$f(t)=v_a(t)+\sum_{i=0}^{N}\kappa_i v_i(t-t_i)u(t-t_i)+v_{vy}(t-t_{vy})u(t-t_{vy}) \tag{5.18}$$

where $v_a(t)$ is the fitting function for the a-wave and has the form of equation (5.15), κ_i, the appropriate attenuation factor and $v_i(t)(i=0, 1, 2...N)$, the fitting functions for the Z-wave and its N'th order reflections with the same form as $v_a(t)$.

5.4.2 CURVE FITTING

The non-linear curve-fitting method of Marquardt ([MARQ 63]) has been used to curve-fit the measured data to obtain the coefficients of the fitting function. Consider a number of data points,

$(x_1, y_1, \ldots\ldots, x_n, y_n)$

each with standard deviation σ_n, and a fitting function,

$y=f(x; a)$

$a=a_0, a_1, \ldots\ldots, a_n$

where x is the independent variable, and the a's are adjustable parameters such that the quantity

$$\phi=\sum_{i=0}^{n}\left[\frac{f(x_i)-y_i}{\sigma_i}\right]^2 \qquad (5.19)$$

is minimized. This procedure provides values for the adjustable parameters such that the fitting function is optimum in a least-squares sense.

Marquardt has suggested a method, based on an earlier suggestion of Levenberg, which varies from the gradient method, used far from the minimum, to the Hessian method, as the minimum is approached (Appendix D).

The minimum reached via the Marquardt algorithm may be a local one. In order to obtain a global minimum, the algorithm is started with many different randomly selected initial values. After many trials, the global minimum is determined by comparing all the calculated local minima and selecting one which can best agree with the correspondingly physical and physiological pictures.

5.4.3 SOLUTION OF THE PARAMETER EQUATIONS

To solve the parameter equations of the two-chamber model as shown in equation (5.16), let $x=1/(R_iC_1)$, $y=1/(R_0C_2)$, $z=1/(LC_1)$ *and* $u=1/(LC_2)$. Substituting x, y, z and u into equation (5.16) and assuming $V_i=1$, one gets

$$\begin{aligned} xu &= 2A\beta^2 = b_1 \\ x+y &= 3\alpha = b_2 \\ xy+z+u &= 3\alpha^2+4\beta^2 = b_3 \\ yz &= \alpha^3+4\alpha\beta^2 = b_4-b_1 \end{aligned} \tag{5.20}$$

These equations can be simplified into a fourth order equation given by

$$x^4-2b_2x^3+(b_2^2+b_3)x^2+(b_4-2b_1-b_2b_3)x+b_1b_2=0 \tag{5.21}$$

Equation (5.21) is solved via the Gauss-Newton method ([DENN 77]), which may yield four real roots, or two real roots and a complex conjugate pair of roots, or two complex conjugate pair of roots. In the first and second cases, there might be two or four sets of parameters. In solving this equation, all complete sets are calculated and compared. The most reasonable set, which has physical meanings and must be real, is chosen. For example, the parameter values cannot be negative, value of C_1 is always larger than that of C_2 because the radii of the proximal vessels are larger than those of the distal vessels (see equation (5.6)). Accordingly the last case is not reasonable because there is no real solution to the model parameters. In fact we have not found any solutions without real roots in all of the calculations.

As an example of the solution of parameter equations, consider a simplified arterial parameter equation which has the form of $x^4-27.3x^3+320.7x^2-1614.1x+1385.6=0$ after substituting b_i in equation (5.21) with the fitted coefficients A, α, and β. This equation has four solutions, viz *8.1288+j9.029*, *8.1288-j9.029*, *9.9787* and *1.0637*. The first two solutions can be discarded in the first place because they are not real ones. The model parameters R_iC_1, R_0C_2, LC_1 and LC_2 of the third solution are *0.1002*, *0.2724*, *0.0114*, *0.0983* and for the last

one *0.9401, 0.0795, 0.0392, 0.0105*. Because it is unreasonable for C_1 to be smaller than C_2, the third solution is also discarded. So only the last set of solutions is left.

At this stage, there are five parameters in the two-chamber model (R_i, L, C_1, C_2, R_0) but only four parameter equations are available (see equation (5.16)). So the model parameters can only be estimated in pairs, i.e., in the product forms of the parameters such as RC and LC which are usually used to reveal the time constant and intrinsic frequency of an RLC circuit. In the EIR model, these terms are good indices for describing the response of the circulatory system to an impulse pressure change caused by the heart contraction and hence reflecting the properties of the circulatory system.

The parameters of the venous part of the EIR model can be solved just like the arterial part. But in some special cases, the a-wave can hardly be seen in the rheopneumogram and hence the venous part of the EIR model consists of only the modified "Windkessel" model. For such a case, the model parameters so reflected in the venous part are just a_1 and a_2 defined in equation (5.17)

5.5 STUDY OF THE MODEL PARAMETER SENSITIVITY

In the modeling analysis, the model parameters should be able to reflect the behaviour of the system, i.e., if there is any change in the system properties, corresponding responses of related model parameters should be observed. On the other hand, a model which is considerably sensitive to the relative small deviations of its parameters is of no use for system simulation and system study. This requires that the sensitivity analysis of the model has to be carried out before accepting the model as an adequate substitute for the real system.

Although modern methods of sensitivity analysis can successfully be applied to the direct study of parameter sensitivity of biomedical systems ([MOLL 84] [FRAN 78] [KING 67]), it can not unfortunately be directly applied to the analysis of the EIR model, because of the complexity and the intrinsic nonlinearity of the model itself. Thus indirect sensitivity analysis, based on simulation of the system model, has been applied here in order to avoid

the computational difficulties related to the problem.

In the simulations, values of model parameter R_i, R_0, C_1, C_2, L for both the arterial and venous parts and γ and V_2 for the venous part only are increased by 1, 5, 10, and 20 percents. While one of these parameters changes, others remain unchanged. The corresponding model output responses are calculated and shown in figures 5.7 to 5.16 respectively. From these figures, we can conclude:

1) increasing the characteristic resistance R_i of the heart output will decrease the amplitude of the flow waveform (figures 5.7 and 5.11);
2) the flow speed will be reduced if the blood inertial L increases (figures 5.10 and 5.14);
3) increasing the peripheral resistance R_0 will increase the blood speed (figures 5.8);
4) the more compliant the blood vessel becomes, the lesser recoiling effect is observable (figure 5.9);
5) The effects of increasing R, L, C, in the venous part are not so significant comparing to its arterial counterparts. However, increasing V_2 and γ, which are the indices of the pressure difference between the lung and the left heart and the blood decay rate through the mitral valve respectively, can result significant variations in the venous component.

While comparing these results to the physical and physiological picture of the human body, it has shown good agreements (more examples can be seen in the next section and chapter 6).

5.6 RESULTS

To illustrate the modeling technique, a typical rheopneumogram from a normal subject was studied. The resulted model parameters are shown in table 5.1, and the model output along with the raw data and resolved arterial and venous components are shown in figure 5.17.

From table 5.1, we can see some significant differences between the arterial and venous vessels. First, values of *LC*s and R_0/R_i of arterial vessels are larger than those of venous. Second, values of RCs of the arterial vessels are smaller than those of venous ones. If we assume that the blood inertance *L* is approximately the same in all cases - a reasonable assumption except for cases of haematologic origin, several results can be observed directly. The compliance of arterial vessel is much larger than that of venous counterpart, and the vascular resistance of the arterial vessel is much smaller than that of venous one. These results can be seen in table 5.2 corresponding to L=1.

Table 5.1 The model parameters

	Arterial	Venous
R_iC_1	0.8985	11.3357
R_0C_2	0.0805	0.1134
LC_1	0.0404	0.0035
LC_2	0.0107	0.0017
$R_0(C_1+C_2)$	0.3839	0.3504
R_0/R_i	0.3376	0.0209
γ		20.531
κ_1	0.3592	
κ_2	0.132	

Table 5.2 Model parameters with assumed L=1

	Arterial	Venous
R_i	22.24	3238.8
R_0	7.523	66.71
C_1	0.0404	0.0035
C_2	0.0107	0.0017

This EIR modeling technique was also applied to study the morphological variations in rheopneumogram caused by the posture and respiratory state of the subject.

When a subject is in the sitting upright position, the measured rheopneumogram has marked difference from that measured in the supine position. Figure 5.18 shows both waveforms of sitting upright and supine. One can observe the marked time lag in the leading edge and the amplitude difference of the Z-wave. This morphological change may be caused by the gravity effect. As the main pulmonary branch is perpendicular to the plane of the earth when the subject is in the position of sitting upright, the blood flows injected from the heart need to overcome the gravity in addition to the vascular bed resistance. As a result, the flow accelerate slowly resulting in the time lag of the leading edge and a decrease in amplitude of the Z-wave.

This phenomenon due to the effect of gravity was studied via the EIR modeling method. Figures 5.19 (supine) and 5.20 (sitting upright) show the fitted data along with their resolved arterial and venous component waves. The model parameters are calculated and shown in table 5.3 again with an assumption that the blood inertial L equals 1 in all cases.

Table 5.3 The model parameters of supine/situp with assuming L=1

Supine/Situp	Arterial	Venous
R_i	300.34/338.98	6236.9/19259
R_0	13.1 /12.76	30.0 /30.2
C_1	0.0116/0.0130	0.0021/0.0024
C_2	0.0020/0.0021	0.0006/0.0005
κ_1	0.4289/0.3980	
κ_2	0.3821/0.2228	

From table 5.3, one can conclude that there are not marked changes between the two cases except for the values of R_i of both the arterial and venous parts. The characteristic resistance R_i increases very significantly due to the effect of gravity in the sitting upright position .

Besides the effect of postures, the respiration may also change the pulmonary vascular resistance and compliance and hence the beat-to-beat rheographic variations. When the lung expands during respiration, the large pulmonary vessels are pulled open by the radial traction of the elastic lung parenchyma which surrounds them ([WEST 79]). As a result, the effective pressure acting around these vessels from outside is low. The calibers of these vessels increase so that the pulmonary vascular resistance decreases (see equation (5.1)) and the vessel compliance increases (equation (5.6)).

To verify this phenomenon, the rheopneumograms measured at two different apneic states, viz apnea at deep inspiration and end of expiration are studied and the measured data are shown in figure 5.21. The fitted data along with their arterial and venous component waves are shown respectively in figures 5.22 and 5.23 for the two respiratory states. The model parameters are shown in table 5.4, which are in good agreement with the physiological and physical pictures described above. The compliance is larger and the vascular resistance

is smaller in apnea at the deep inspiration than those of apnea at the end of expiration.

Table 5.4 The model parameters of Ins./Exp. with assuming L=1

Inp./Exp.	Arterial	Venous
R_i	457.7/568.9	2252.2/9631.2
R_0	13.11/16.08	80/53.40
C_1	0.0128/0.0080	0.0042/0.0012
C_2	0.0018/0.0012	0.0017/0.0005
κ_1	0.2985/0.2872	
κ_2	0.0730/0.1988	

5.7 CONCLUSION

In this chapter, an EIR modeling method has been presented to estimate the properties of the pulmonary circulatory system from a measured rheopneumographic waveform. The model parameters are calculated by a two-stage parameter identification scheme. The rheopneumogram variations resulted from the effect of gravity and different respiratory states are studied via this model-based method. Results show that the model parameters are in good agreement with the physiological and physical pictures.

5.8 NOTES ON PUBLICATIONS

A paper entitled "Modelling Analysis of the Rheopneumogram Via Bio-electrical impedance Technique" was presented at Inter. Conf. on Electrical Bio-impedance'92, Finland. A more detailed version of this paper has been submitted to the journal *Medical Progress Through Technology* for consideration of publication. Another paper entitled "Modelling of the Pulmonary Circulation via Electrical Bio-impedance Technique" was presented at 14th Annual IEEE-EMBS'92 Conf., Paris. All these papers were jointly authored with Mr Thomas T. C. Choy.

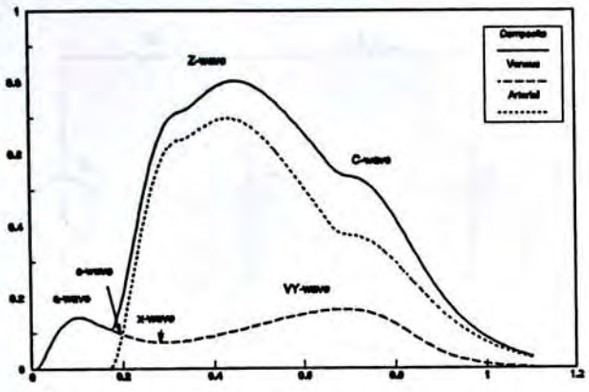

Figure 5.1 A typical rheopneumogram with its arterial and venous components.

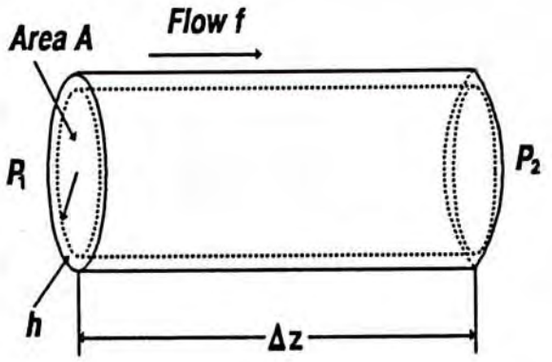

Figure 5.2 A cylindrical vessel, where P_1 and P_2 are the pressures at the two ends, Δz the length of the vessel, h the thick of the vessel wall, A the area of cross section.

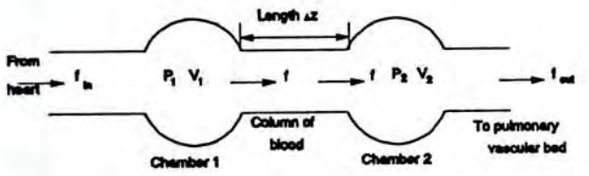

Figure 5.3 The physical two-chamber model, where P_1 and P_2 are the pressures of the two chambers, V_1 volume of the first chamber, V_2 volume of the second chamber, $\dot{\eta}z$ length of the vessel;

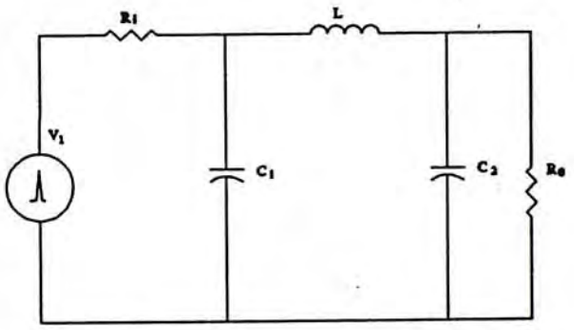

Figure 5.4 The electrical model of arterial vessel, where V_1 is the impulse source, R_i the characteristic resistance, L the blood inertance, C_1 and C_2 the compliancies, R_0 the peripheral resistance.

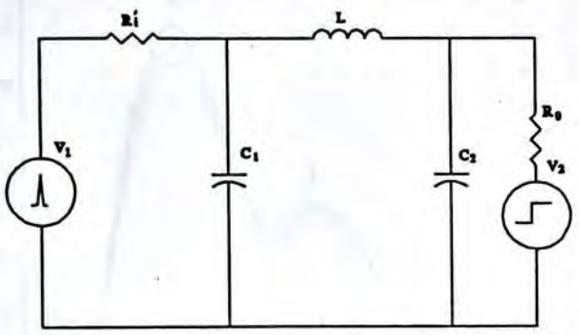

Figure 5.5 The electrical model of the major venous vessel, symbols are identical to those defined in figure 4.4 and V_2 is a step source standing for the pressure difference between the lung and the heart.

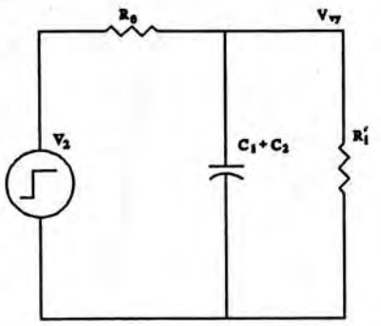

Figure 5.6 The electrical model of the blood charging effect degenerated from figure 4.5 with some simplifications.

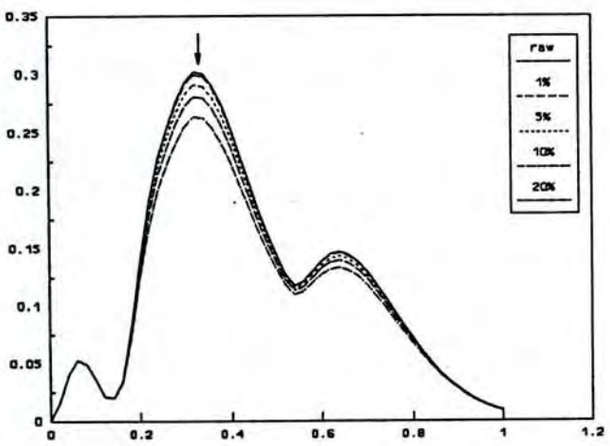

Figure 5.7 Responses of the model output with R_i of the arterial part increased by 1%, 5%, 10% and 20%. Arrow shows the trend of variation.

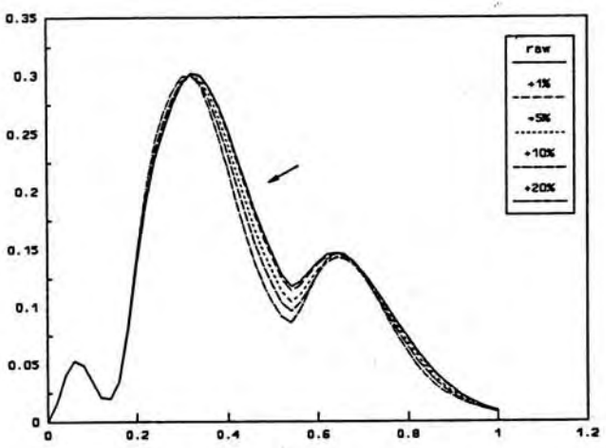

Figure 5.8 Responses of the model output with R_0 of the arterial part increased by 1%, 5%, 10% and 20%. Arrow shows the trend of variation.

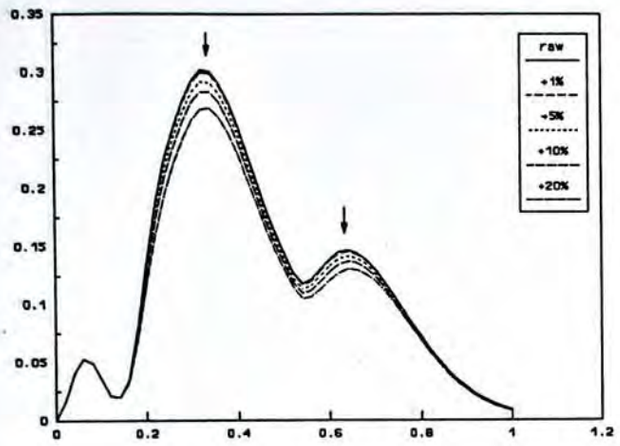

Figure 5.9 Responses of the model output with C_1 and C_2 of the arterial part increased by 1%, 5%, 10% and 20%. Arrow shows the trend of variation.

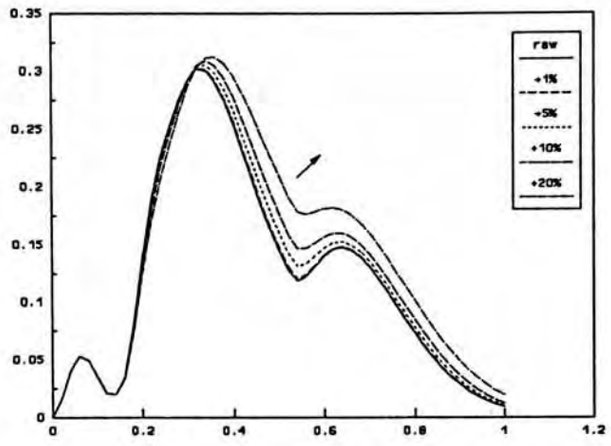

Figure 5.10 Responses of the model output with L of the arterial part increased by 1%, 5%, 10% and 20%. Arrow shows the trend of variation.

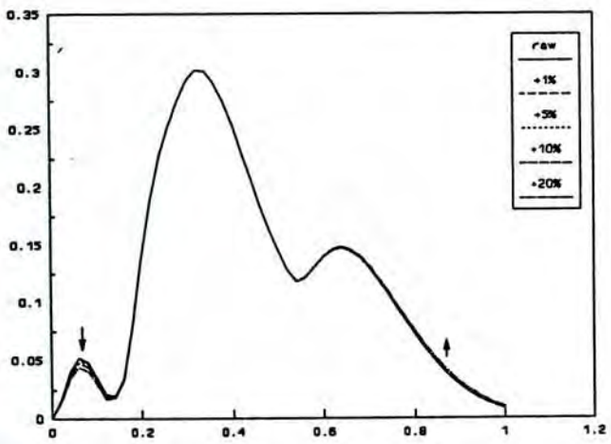

Figure 5.11 Responses of the model output with R_i of the venous part increased by 1%, 5%, 10% and 20%. Arrow shows the trend of variation.

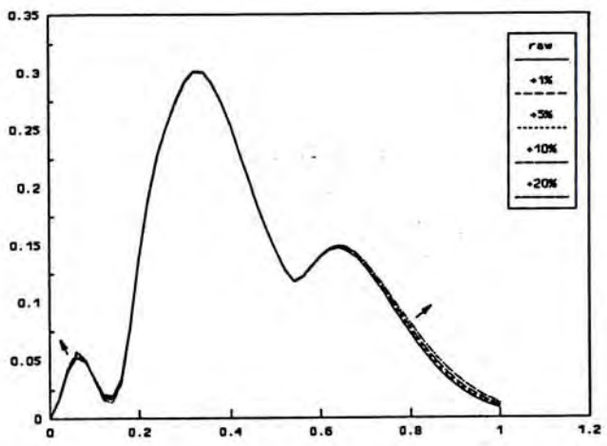

Figure 5.12 Responses of the model output with R_0 of the venous part increased by 1%, 5%, 10% and 20%. Arrow shows the trend of variation.

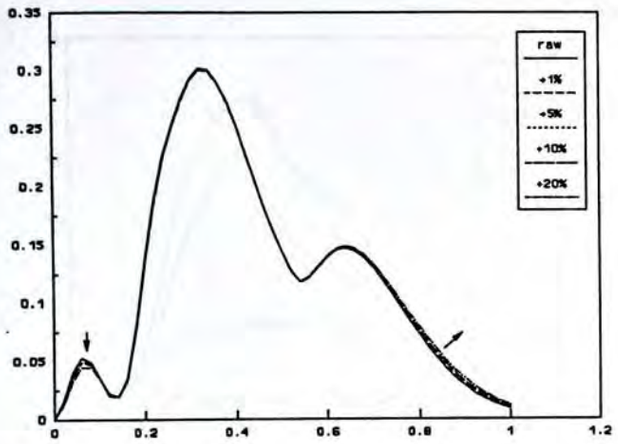

Figure 5.13 Responses of the model output with C_1 and C_2 of the venous part increased by 1%, 5%, 10% and 20%. Arrow shows the trend of variation.

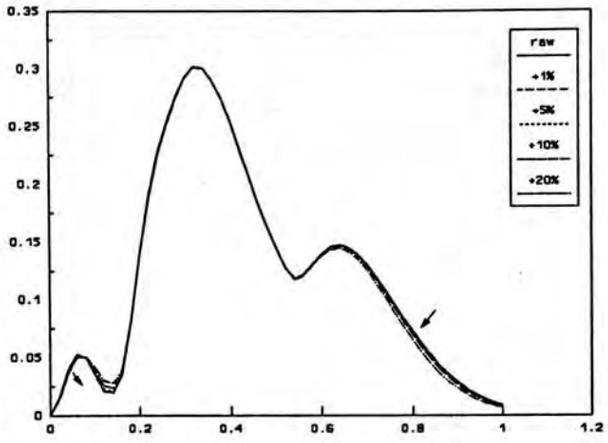

Figure 5.14 Responses of the model output with L of the venous part increased by 1%, 5%, 10% and 20%. Arrow shows the trend of variation.

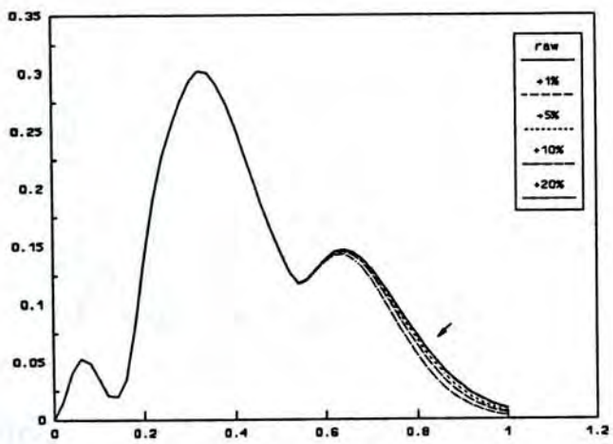

Figure 5.15 Responses of the model output with the value of γ of the venous part increased by 1%, 5%, 10% and 20%. Arrow shows the trend of variation.

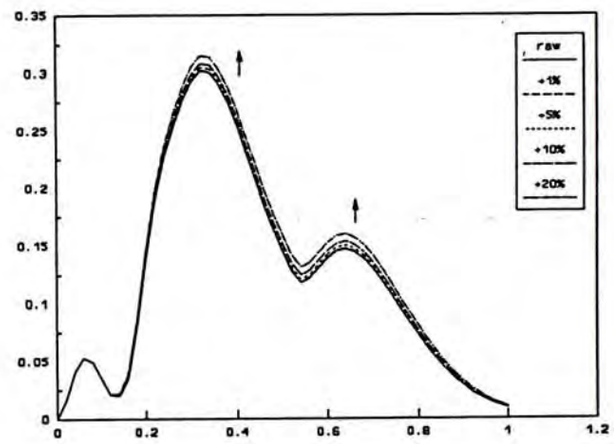

Figure 5.16 Responses of the model output with the value of pressure difference (V) of the venous part increased by 1%, 5%, 10% and 20%. Arrow shows the trend of variation.

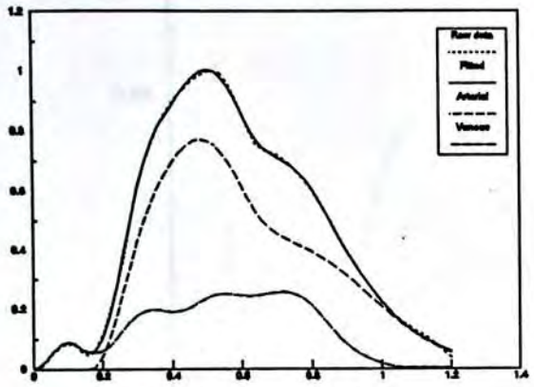

Figure 5.17 Raw and fitted data of a typical normal rheopneumogram along with its arterial and venous components.

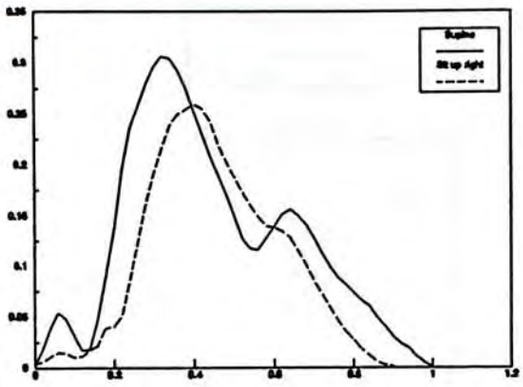

Figure 5.18 Rheopneumograms recorded in supine and sitting upright positions.

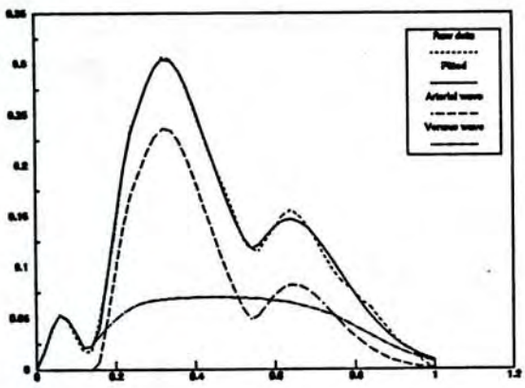

Figure 5.19 Raw and fitted data of supine with its resolved arterial and venous components.

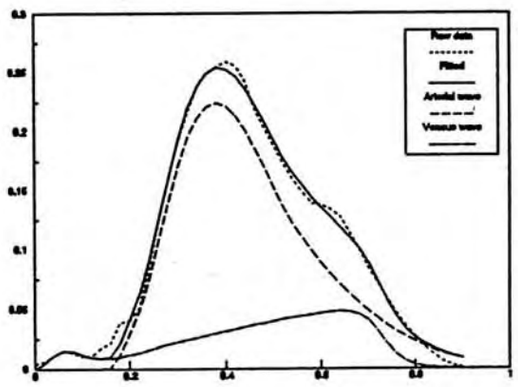

Figure 5.20 Raw and fitted data of sitting upright along with its resolved arterial and venous components.

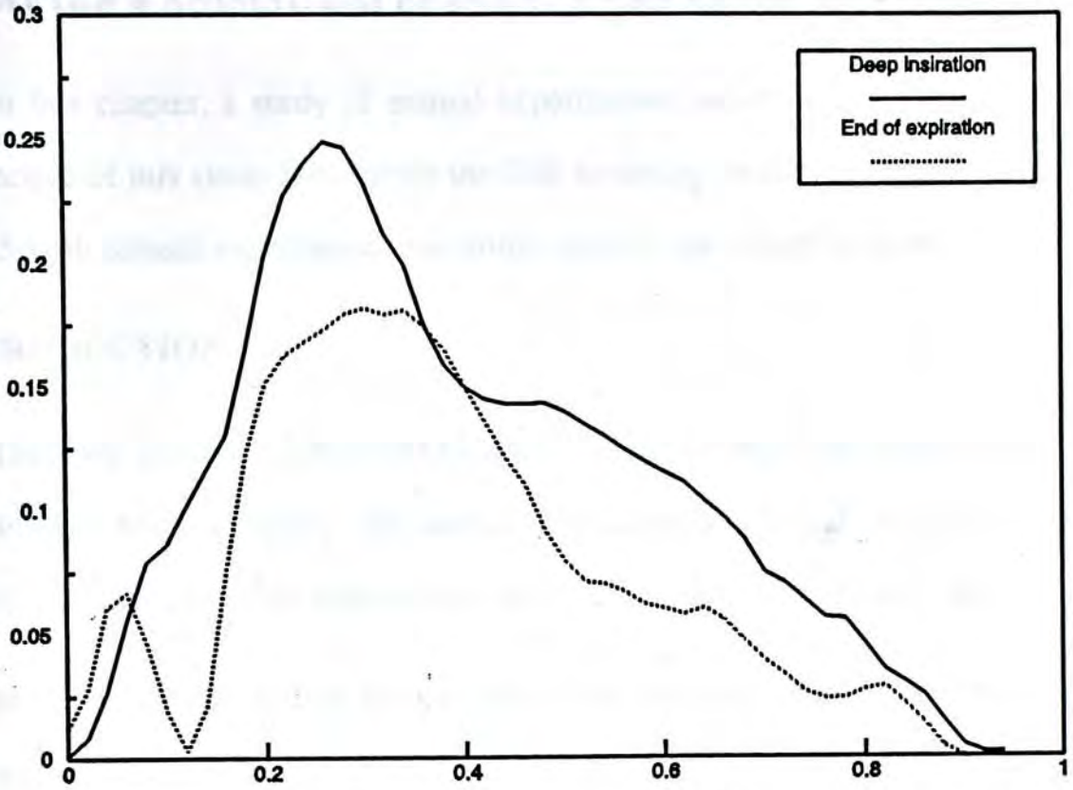

Figure 5.21 Rheopneumograms measured in apnea at deep inspiration and end of the expiration.

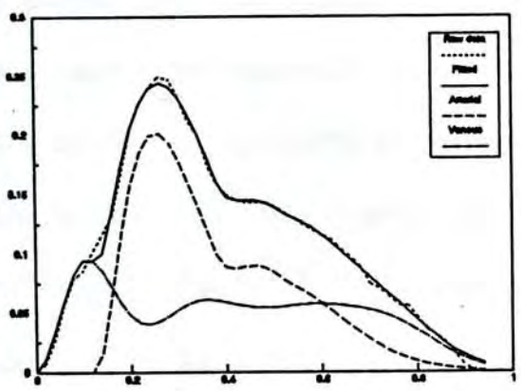

Figure 5.22 Raw and fitted data along with its arterial and venous components (apnea at deep inspiration).

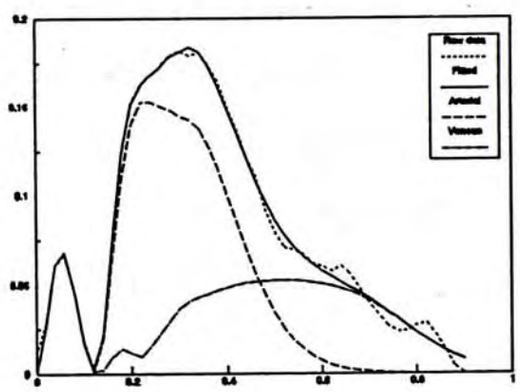

Figure 5.23 Raw and fitted data along with its arterial and venous components (apnea at the end of expiration).

CHAPTER 6 ANIMAL EXPERIMENTS AND CLINICAL OBSERVATIONS

In this chapter, a study of animal experiments and clinical observations is reported. The objective of this study is to verify the EIR modeling methods proposed in chapter 3 and chapter 5 with animal experiments and some specific pathological cases.

6.1 INTRODUCTION

There are three major methods for physiologists to obtain the physiological knowledge of the human body systems, viz animal experiments, clinical observations and recent commonly applied computer simulations with analog and mathematical models.

In the previous chapters, the computer simulation methods were introduced and used to analyze the EIR signal. These simulation methods can not only provide an insight into the circulatory system in terms of system dynamics but also be used to estimate the system properties.

On the other hand, the animal study can also provide some useful information about the human systems because the human systems are much like those of other animals, particularly other mammals. Physiologists have taken advantage of these similarities to study many aspects of physiological systems in animals. Even though animals may differ markedly from humans in some aspects, however, the resemblances in the amazingly complex physiological systems in different mammalian species are more important than the differences. Moreover, in the animal experiments, some unwanted and insignificant subsystems can be removed to make the observation more easily.

The objective of the present work is to test and verify our modeling methods. For this purpose, we had gone to the Guangxi Medical University to carry out two animal experiments, viz pulmonary artery occlusion and deformation. Clinical data of some specific cases were also taken.

6.2 ANIMAL EXPERIMENTS

Previous works on pulmonary artery occlusion had been carried out on animals by Xiong ([XION 81], [XION 83]) and Kuwahira ([KUWA 81]). In their experiments, they observed an amplitude decrease in the rheopneumographic waveform after the pulmonary blood flow of the side blocked, and an amplitude increase at the other side of the lung at the same time. They concluded that the rheopneumogram was mainly composed of impedance changes from the pulmonary circulation. However, they only paid attention to observed amplitude variations but ignored waveform morphological variations.

To study the rheopneumographic composition of pre-/post-occlusion, an animal experiment was carried out in which the pulmonary arterial blood flow was partially occluded and then completely occluded at the root of the right pulmonary artery. Besides, another experiment was performed to observe the arterial wave reflections after the pulmonary artery was deformed by an external force.

6.2.1 METHODS

Experiments were carried out on two healthy dogs, weighing about 10 to 15 kilograms. During the experiments, the dogs were intubated intra-tracheally under general anesthesia using sodium pentobarbital. Curare (0.5-0.7 mg/kg) was given intravenously to stop the respiration of the dogs to eliminate the respiratory artefact and instead, a respirator was provided to maintain a vital capacity of 300ml. While the rheopneumographic recordings were going on, the respirator was switched off so that no respiratory artefact was involved.

Rheopneumographic signals were recorded simultaneously for both sides of the lungs along with the ECG signal. Figure 6.1 shows the diagram of the data acquisition system and the electrode placement using the conventional electrode placement scheme (chapter 3).

6.2.2 OCCLUSION OF THE RIGHT PULMONARY ARTERIAL BLOOD FLOW

The objective of this experiment is to account for the rheopneumographic signal

variations of pre-/post-occlusion of the pulmonary arterial blood flow by external ligation. The experiment was carried out in two stages. The right pulmonary arterial blood flow was first partially blocked at the position I (ie, only the lower and middle branches of the right pulmonary arteries were blocked as shown in figure 6.2), and then completely blocked at the root (position II as shown in figure 6.2).

Rheopneumograms of normal, partial and complete occlusions along with simultaneous ECG signal are shown respectively in figures 6.3, 6.4 and 6.5. From these figures we can observe that, 1) Significant amplitude variations take place on both sides of the lungs; 2) The right side wave morphology varies markedly but the left side one does not. For the amplitude variations, a decrease from the right side original value of 0.2 to 0.18, and an increase from 0.34 to 0.7 of the left side can be observed when occluding the right pulmonary lower and middle branches.

For the waveform morphological variations, one can observe that the right side waveform morphology changes much as the occlusion becomes more serious, but the left side does not show such a trend. Moreover, while observing the rheopneumogram with the time landmark of the simulations ECG signal, one can see that the leading edge of the right side rheopneumogram of the lung shifts to the left in the case of complete occlusion as shown in figure 6.4, which indicates that the rheogram is mainly composed of systemic circulation component in view of the blood flow speed difference between the systemic and pulmonary circulations.

These observed results are quite compatible with that of Xiong's ([XION 83]) and in good agreement with what we obtained in chapter 3 (see figures 3.8 and 3.9) where the composition of the rheopneumogram was calculated via computer simulations on a numerical model. Hence we can conclude that the rheopneumogram is composed mainly of the component of pulmonary circulation, however, the interference from the systemic circulation still exists.

6.2.3 REFLECTION WAVES IN RHEOPNEUMOGRAM

In the measurements, some ripples were often observed in the descending slope of the Z-wave. Such ripples were treated as the arterial reflection waves in the modeling analysis and believed that they related to the vessel compliance and the impedance mismatch in the vessels. To observe how the vessel compliance and the impedance mismatch can affect the waveform morphology, an animal experiment was carried out by deforming the pulmonary artery with an external press as shown in figure 6.2.

Figure 6.6 and 6.7 show the rheopneumographic waveforms of pre-/post-deformation. Since this experiment was carried out after the experiment of arterial occlusion, the arterial component waves became smaller than those of the venous ones in both the normal and deformed cases. In figure 6.7, one can observe that there are more ripples in the arterial component wave when the pulmonary artery is deformed.

The two waveforms of pre-/post-deformation were analyzed by the EIR modeling method. After assuming the blood inertance to be the same in all cases, model parameters can be calculated as shown in table 6.1. The venous model parameters are almost the same for both waveforms, but the arterial model parameters changes markedly. This is because that the arterial vessels are squashed under the external force so that the vascular resistance increases and the vessel compliance decreases. The reflection factors κ_1 and κ_2 are also increased due to the impedance mismatch resulting from the vessel deformation.

6.3 CLINICAL OBSERVATIONS

To further verify the EIR modeling method, normal and typical pathological cases of mitral valve stenosis and obstructive emphysema were studied and compared to the normal ones.

Table 6.1 Model parameters of Normal/Deformed rheopneumograms (L=1)

Normal/Deformed	Arterial	Venous
R_i	170.28/721.66	431.42/474.96
R_0	11.63 /21.28	30.06 /26.76
C_1	0.0163/0.0053	0.0042/0.0045
C_2	0.0024/0.0007	0.0017/0.0017
κ_1	0.5318/1.0	
κ_2	0.0 /0.4839	

6.3.1 MITRAL VALVE STENOSIS

The mitral valve stenosis is a kind of heart disease in which the mitral valve becomes narrower resulting in difficulty for the blood to empty from the left atrium to the left ventricle after the mitral valve opening and the blood over-filling the venous system. In the EIR waveforms, one can easily observe the a-wave with respect to the arterial wave in the case of mild stenosis as shown in figure 6.8. However, when the stenosis becomes serious, the venous system is filled with too much blood resulting in increases in the blood pressure and vascular resistance so that the a-wave may decrease in amplitude (figure 6.9). With the stenosis becoming even more serious, the a-wave can disappear (figure 6.10). The blood flow in the arteries is also impeded by the high blood pressure in such vessels as a result of over-filling of the blood in the pulmonary circulatory system. In such a case, the arterial wave can even become smaller than its venous counterpart (VY-wave).

Results of model parameters are shown in table 6.2, where the model parameters for normal subjects are the averaged values from 9 normal subjects aged about 21 years old and the three cases of mitral valve stenosis are classified as mild, average and serious in condition.

Table 6.2. Model parameters of normal and mitral valve stenosis.

	Normal	Mitral Valve Stenosis		
V/A		(Mild	Average	Serious)
R_iC_1	5.8747/1.2028	1.8404/1.1016	2.3996/1.2553	/1.94
R_0C_2	0.0533/0.0369	0.0328/0.0221	0.0324/0.0168	/0.014
LC_1	0.0029/0.0146	0.0033/0.0081	0.0033/0.0076	/0.0032
LC_2	0.0012/0.0034	0.0012/0.0014	0.0012/0.0009	/0.0006
$R_0(C_1+C_2)$	0.1770/0.2015	0.1227/0.1504	0.1215/0.1524	0.17/0.094
R_0/R_i	0.0253/0.1530	0.0488/0.1164	0.0372/0.1080	0.1/0.0412
γ	25.756/	8.0988/	13.549/	12.0/
κ_1	/0.739	/0.361	/0.5154	/0.9
κ_2	/0.363	/0.328	/0.3126	/0.9

** V/A: Values of the venous and arterial model parameters

Among the model parameters, the parameter γ (defined in equation (5.13)), which is a measure of the decay rate of the flow from the left atrium into the left ventricle after the mitral valve opening, is the most significant index to distinguish whether the rheopneumogram is normal or indicative of stenosis. A smaller value γ corresponds to a narrower aperture of the mitral valve and hence a slower filling of the left ventricle from the left atrium. However, the values of γ listed in table 6.2 do not relate to the extent of the stenosis. The stenosis becoming serious means that other effects such as the venous system over-filling and increase in blood pressure are resulted because of the stenosis.

With a more careful study of the values shown in table 6.2, more information about the cases studied can be obtained. For the venous part of the stenotic cases, the values of RCs are smaller than those of the normal, which indicates that the veins of the former can respond faster to the left atrium contraction so that the a-wave can be more readily observed. Moreover, because the value of $R_0(C_1+C_2)$ becomes smaller and the value of R_0/R_i larger compared to those of the normal, the blood volume in the veins and the left atrium resulted from the return blood flow from the lung can be built up faster and hence further contributes

to the prominence of the C-wave (see equation (5.17)).

On the other hand, the arterial part of the stenotic cases also shows some changes. The values of *LC*s are relatively smaller which indicates a faster recoil effect of the arterial wave subsequent to the pulsatile ejection.

Furthermore, if we assume that the blood inertance L is approximately the same in all cases - a reasonable assumption except for cases of haematologic origin, several results can be deduced.

First, for the venous part, the compliance values of C_1 and C_2 have not changed so much among all cases. So the characteristic resistance R_i and the peripheral resistance R_0 of the mitral valve stenosis are smaller than the normal values and that is the reason why the a-wave and C-wave can be more readily observed as shown in figure 6.8 and 6.9.

Second, for the arterial part of the model, the values of C_1 and C_2 in the case of mitral valve stenosis are smaller than those for the normal and become even smaller as the stenosis become more serious but the resistance to the blood flow becomes larger and larger. This results in greater impedance mismatch in the blood vessels so that the reflection factors κ_1 and κ_2 are larger in the case of the serious stenosis.

6.3.2 OBSTRUCTIVE EMPHYSEMA

The obstructive emphysema is resulted from the small pulmonary vessels being widely damaged. Blood flows in the arteries are impeded and the blood volume in the venous system is also decreased. As a result, the a-wave can hardly be observed and the amplitude of Z-wave decreases.

Figure 6.11 shows a typical rheopneumogram of obstructive emphysema along with the fitted data and its arterial and venous component waves. The averaged model parameters of four subjects suffering from the emphysema are shown table in 6.3.

Table 6.3 Model parameters of the normal and the obstructive emphysema (OE)

Normal/OE	Arterial	Venous
R_iC_1	1.2028/0.9093	
R_0C_2	0.0369/0.0228	
LC_1	0.0146/0.0147	
LC_2	0.0034/0.0018	
$R_0(C_1+C_2)$	0.2015/0.2110	0.1770/0.1430
R_0/R_i	0.1530/0.2083	0.0253/0.1048

For the arterial part, if we assume that the blood inertance is the same for normal and the emphysema, we can see that the distal compliance C_2 for the emphysema is smaller than that of normal. Whereas the proximal compliance C_1 does not change so much. Moreover, the value of R_0/R_i becomes larger in the case of OE indicating the peripheral resistance increase. And for the venous part, similar result can be obtained. These results are quite good in agreement with the physiological picture where the compliance decrease and peripheral resistance increase are a consequence of the vascular damage in the obstructive emphysema.

6.4 CONCLUSION REMARKS

In this chapter, studies on animal experiments and clinical observations have been reported. Results have shown good agreements between the model parameters and the physiological and physical pictures. However, it does not mean we can apply this result in clinical diagnosis, because at this present stage, all indices or model parameters are obtained from a very limited measurements so they can only be used to verify the usefulness of the method.

6.5 NOTES ON PUBLICATIONS

A paper entitled "Non-invasive estimate of the properties of the pulmonary circulation from electrical impedance rheopneumographic measurements by modeling method" has been submitted to the Journal of Biomedical Eng. This paper was jointly authored with Thomas T. C. Choy, G.F. Xiong and Dr H.S. Chan.

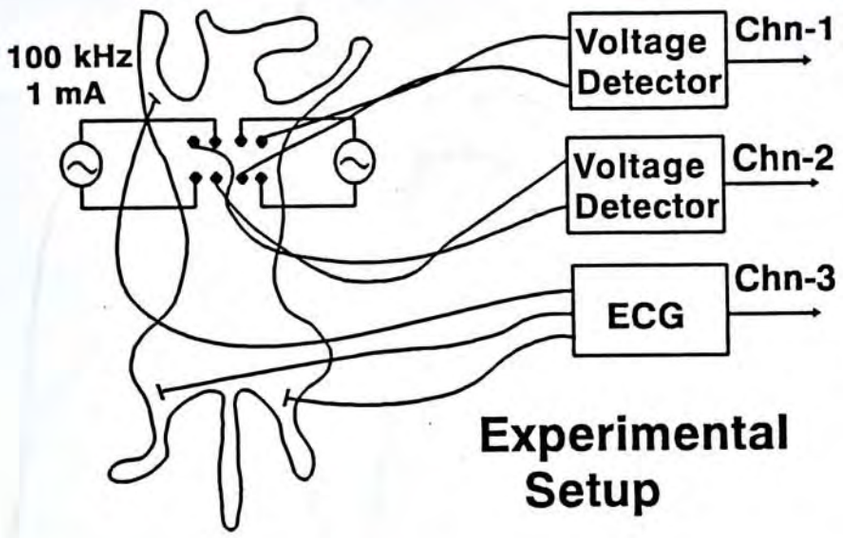

Figure 6.1 The equipment setup and electrode placement.

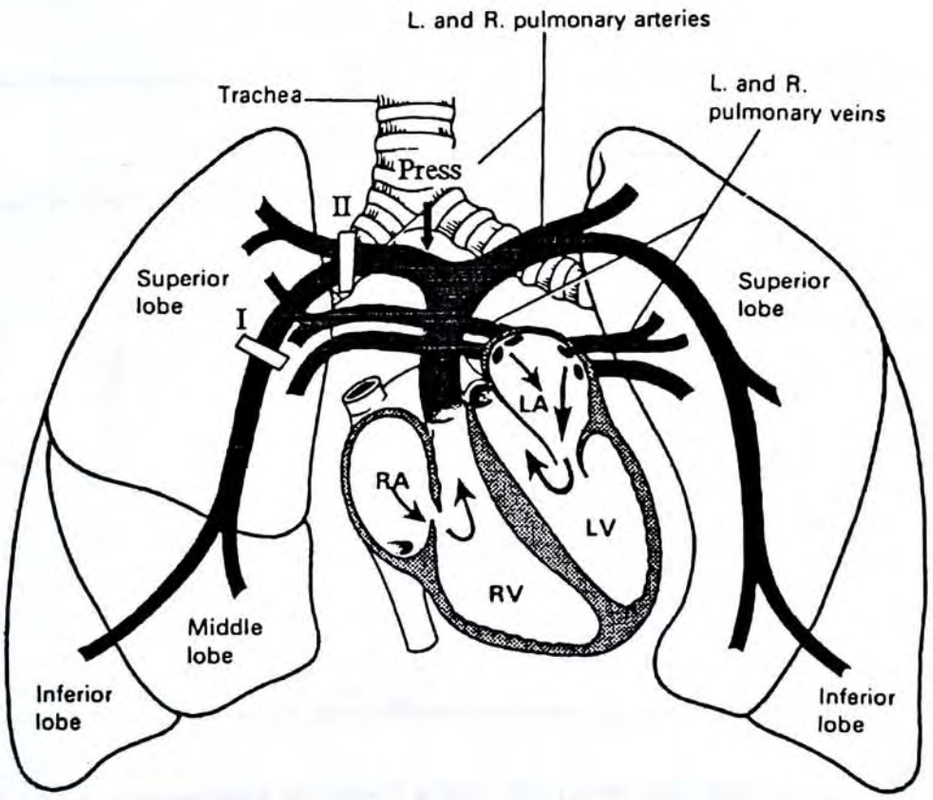

Figure 6.2 Diagram of animal experiments. Positions of occlusion and deformation are indicated.

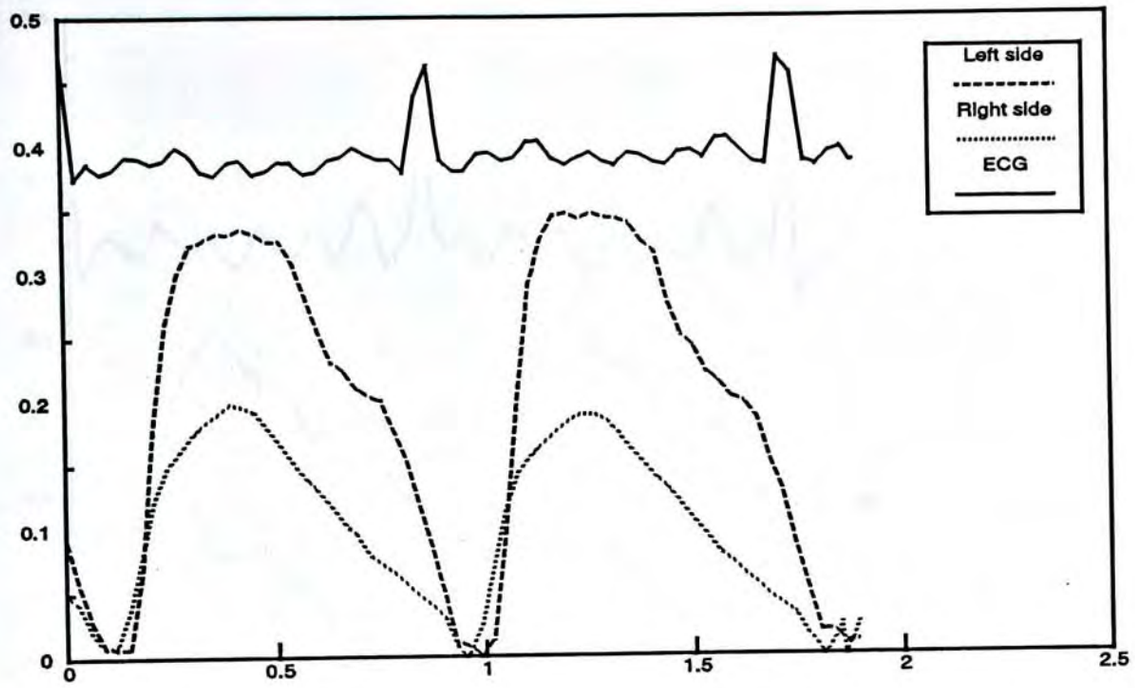

Figure 6.3 Rheograms measured from a dog before the occlusion of the right side pulmonary artery.

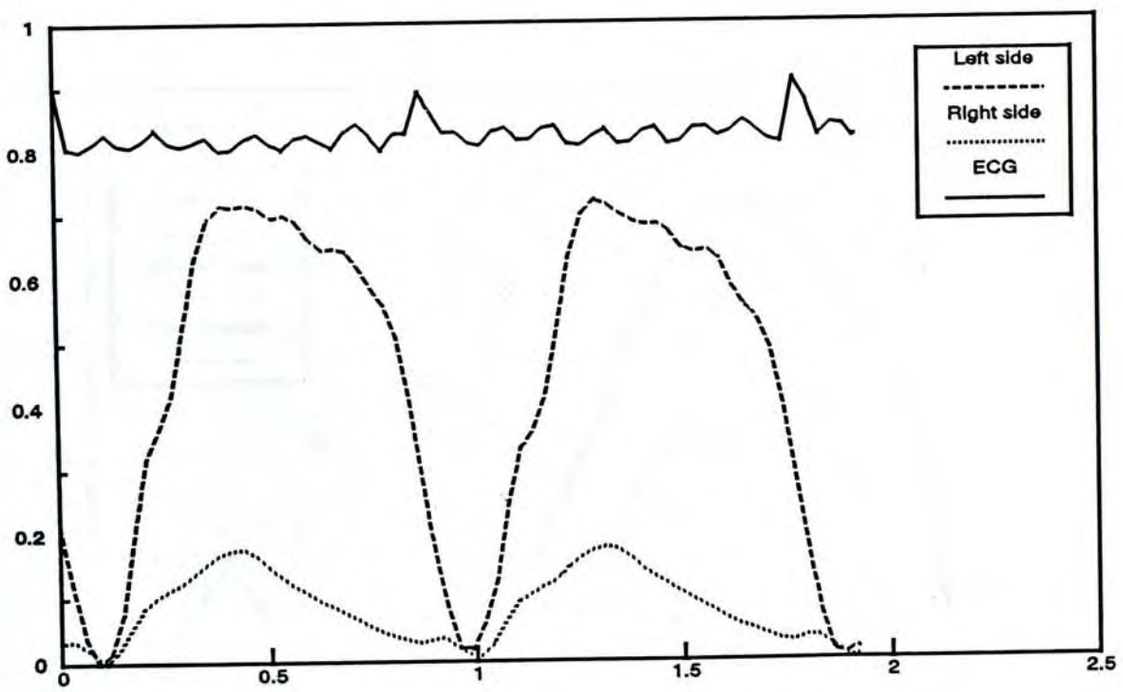

Figure 6.4 Rheopneumograms recorded when the right side pulmonary arteries are partially occluded. The amplitude variations can be observed.

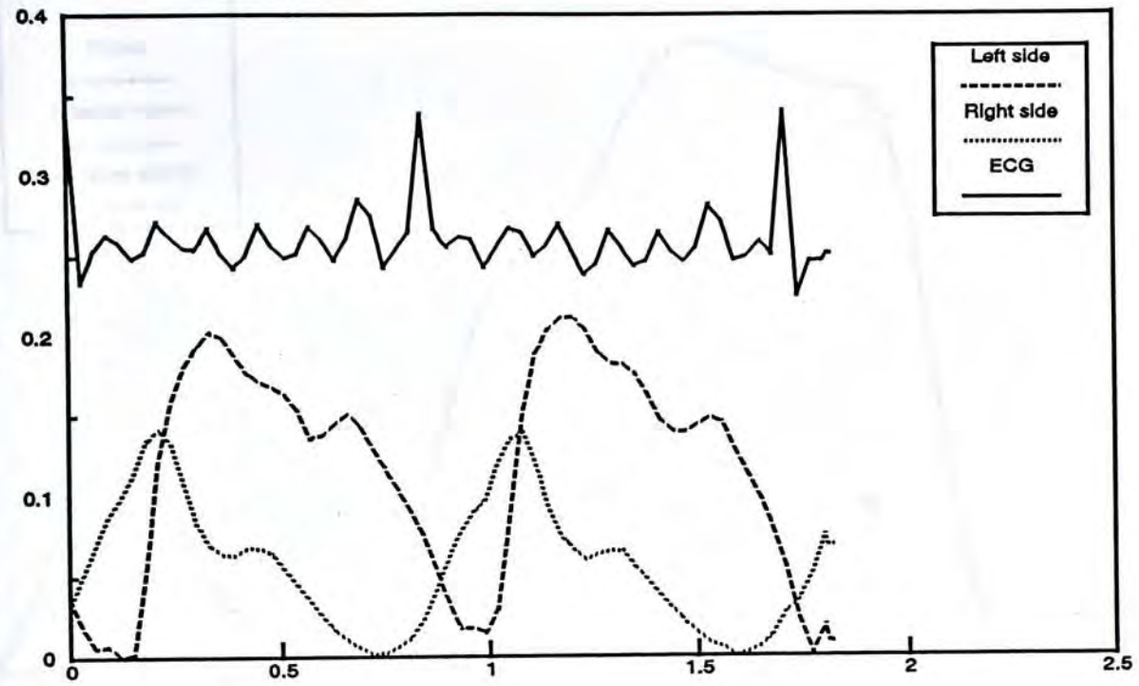

Figure 6.5 Rheopneumograms recorded when the right side pulmonary arteries were completely occluded. Since the dog was dying during this experiment, therefore, the recorded rheopneumograms of both sides became small compared to those of normal. However, the wave morphology can also show the effect of occlusion.

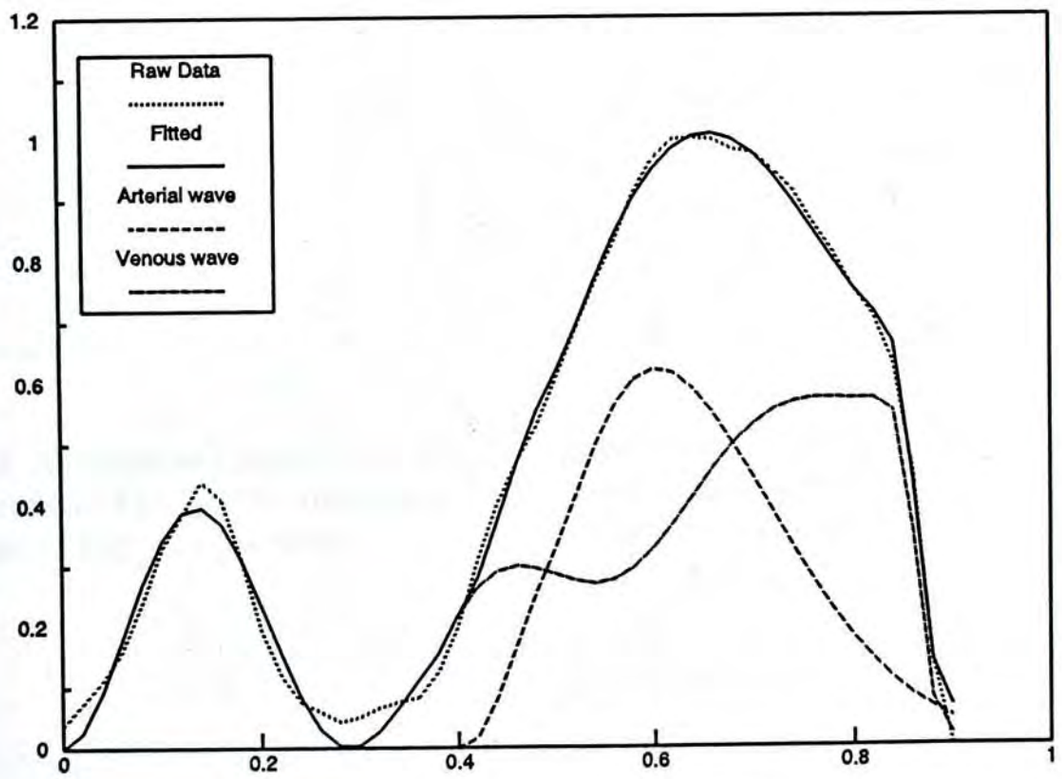

Figure 6.6 Raw and fitted data of a dog along with the arterial and venous component waves. (no deformation of the pulmonary artery)

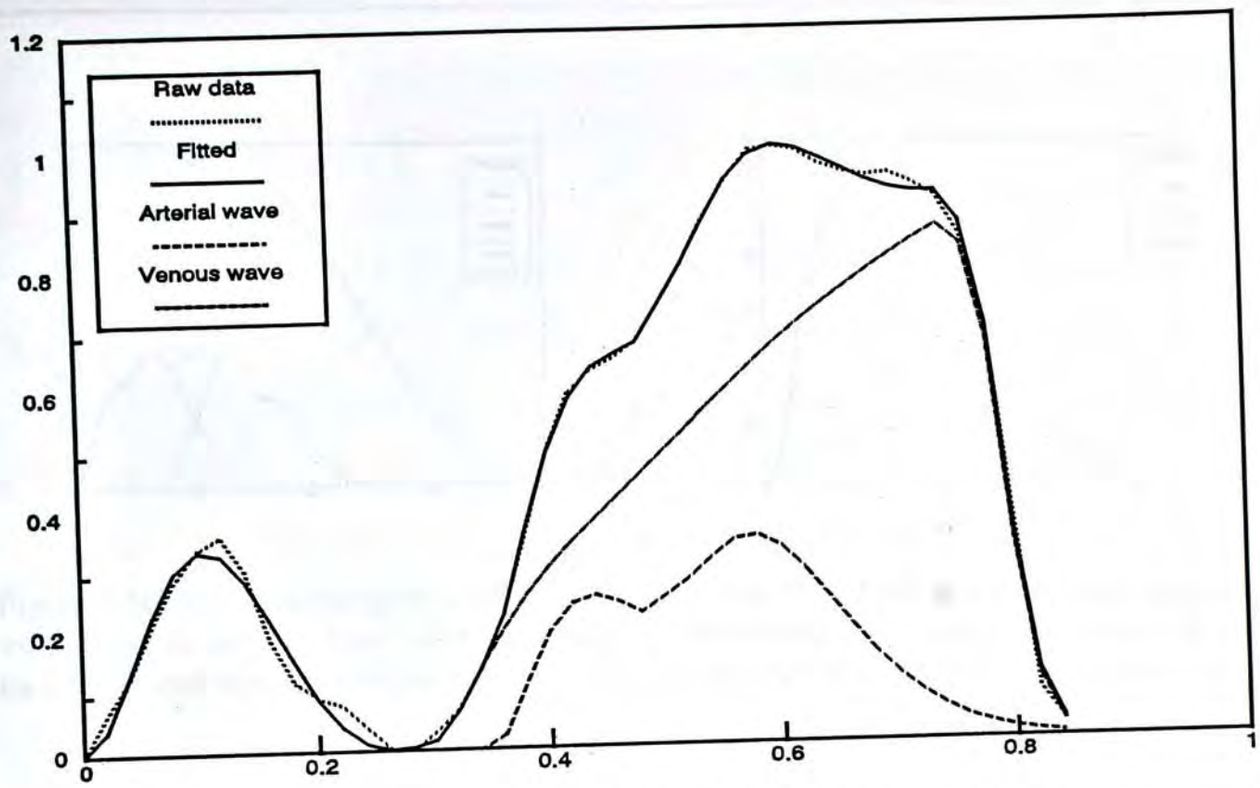

Figure 6.7 Raw and fitted data along with the arterial and venous component waves. (Deforming the right side pulmonary artery by external force).

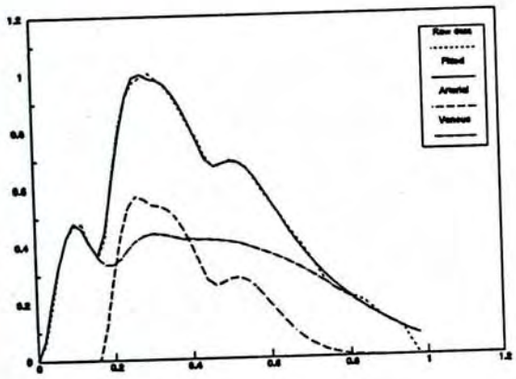

Figure 6.8 Rheopneumogram of the mitral valve stenosis (light) with fitted and its arterial and venous components.

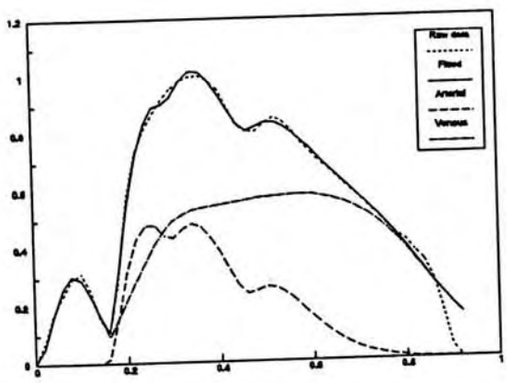

Figure 6.9. Rheopneumogram of the mitral valve stenosis (average case) with fitted and its arterial and venous components.

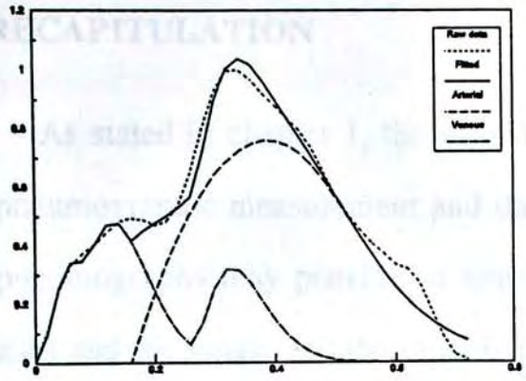

Figure 6.10. Rheopneumogram of the mitral valve stenosis (serious case) with fitted and its arterial and venous components.

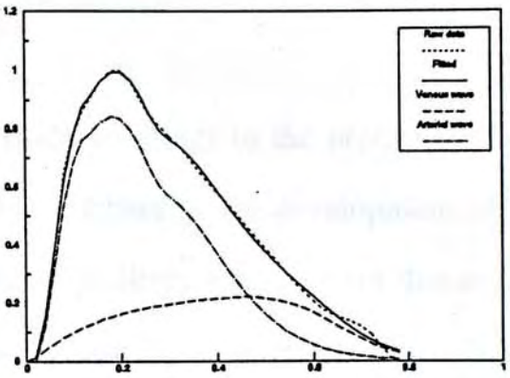

Figure 6.11 Raw and fitted data along with the arterial and venous component waves of a subject with obstructive emphysema.

CHAPTER 7 RECAPITULATION AND TOPICS FOR FUTURE INVESTIGATION

7.1 RECAPITULATION

As stated in chapter 1, the goal of work is to study solutions to the problems in the rheopneumographic measurement and data analysis. The success in the development of the rheopneumography may provide an non-invasive method for clinicians to detect diseases in the heart and the lungs, and the most important the blood flow in the pulmonary circulation. This thesis essentially contains several contributions to the development of this technique - suggesting an optimum electrode configuration, eliminating the respiratory artefact and analyzing the rheopneumogram with modeling method.

In chapter 3, the possible origins of the impedance change were studied and their contributions to the rheopneumogram were estimated via numerical methods and computer simulations. A numerical 2D model of a transthoracic section was developed and corresponding tissue resistivity was assigned. In order to calculate contributions of all possible origins, dimension and resistivity changes of each origin between the heart in the states of end diastole and end systole were simulated and the resulted differential potential distribution was calculated via the finite element method. As such, the composition of the rheopneumogram with the conventional electrode was given, which had never been reported before. An optimum electrode configuration was suggested with which the rheopneumogram could be measured with the least interference of other origins.

In chapter 4, much attention was paid to develop real-time and adaptive processing techniques dealing with the respiratory artefact. Several signal processing methods such as the moving averager, the adaptive noise canceller and the FIR filter were studied and improved on. The impedance signal measured on the transthoracic surface from a group of subjects were first statistically analyzed in the frequency domain, which showed the frequency distributions of the rheopneumogram and the respirogram. With regarding to the features of the transthoracic impedance signal which were time varying and sometimes frequency inbanding, improvements to the three methods mentioned above were made.

For the ANC method, the respiratory reference signal was picked up with another pair of surface electrodes where the respiratory signal was more prominent and the rheopneumographic signal much smaller. Moreover, a moving averager was applied in the reference path so that the rheopneumographic component so picked up was much less significant. With these modifications, better signal to noise ratio and signal distortion ratio in the ANC output had been obtained. As the ANC method required a finite time to converge and might not be able to track the varying of the respiratory signal at times, improvements to the moving averager and FIR filter were made via adaptive tracking of the frequencies of the respiratory and rheopneumographic components so that at any time the optimum cutoff frequency could be obtained. On-line short time DFT technique was applied to guarantee the speed of spectrum analysis and a coefficient look-up table was used so that all coefficients could be obtained in the CLT with no need of recalculation.

Filters mentioned above were implemented and their results were compared in terms of SNR and SDR indices and correlated to the impedance waveform measured at the apneic state. The comparison results showed that the adaptive FIR filter presented the best performance, whereas the adaptive moving averager was the simplest and the fastest in implementation and processing.

Finally, an EIR lumped model for the pulmonary circulation was derived in chapter 5 and was further verified with animal experiments and clinical observations in chapter 6. As the impedance detection over a region is a lumped effect, the development of the EIR model is developed mainly based on a lumped two-chamber model, which can reflect not only the properties of the circulatory system such as the proximal and distal vessel compliance, the blood inertance and peripheral resistances, but also other parameters corresponding to the characteristics of the mitral valve and the pressure difference between the lung and the left heart. The model parameters were calculated via a two-stage identification scheme, i.e., a fitting function derived from the model output was first fitted to the measured data, and in the second stage the model parameters were calculated from a set of parameter equations

which was derived from the Laplace transforms of the fitting function and the model output. This EIR model was proved in several aspects, viz computer simulations, animal experiments and some specific physical and pathological cases. Results of these case studies demonstrated the usefulness of the modeling method.

7.2 CONCLUSIONS

This study has primarily solved three basic problems in the electrical impedance rheopneumography. These include avoiding the systemic interference, eliminating the respiratory artefact, analyzing the EIR waveform with physiologically modeling method.

The problem of interference between the systemic and pulmonary circulations was first paid attention by this study and solved via computer simulations and as a result, an optimum electrode configuration was determined and suggested.

To the problem of respiratory artefact, it was found that a filter with ability of adaptively adjusting its cutoff frequency was needed to separate the respiratory and rheopneumographic components. Therefore, an adaptive FIR filter with a coefficient look-up table was proposed in this study. This filter can also be used to process other biomedical signals with similar problems of rheopneumographic measurements.

This study was the first to analyze the EIR waveform by modeling analysis method. This EIR modeling method has many advantages over the analysis methods adopted in China. It can provide more physiological information and estimate the properties of the cardiopulmonary system.

In conclusion, the EIR technique proposed in this study has been proved to be valuable and it is believed that it can be a useful diagnostic and monitoring tool in clinical applications of ICU and CCU.

7.3 TOPICS FOR FUTURE INVESTIGATION

In this section, we present some limitations of the methods proposed in this work and highlight some possible research works for further investigation.

- Analyzing the composition of EIR via 3D thoracic model

In chapter 3, the composition analysis based on the 2-D numerical model might raise inaccuracy due to the ignorance of contributions from some other impedance change origins lying in the same and other transthoracic layers. These possible origins include the heart chambers, the lungs and systemic blood flows in the extrathoracic cage. From the simulation result on the layer T7 and T8 showed in chapter 3, the contribution from the heart contraction might be quite considerable. As such, the computer simulation based on a 3D numerical model of the thorax is necessary to gain more accurate composition calculations and hence the optimum electrode configuration for the rheopneumographic measurement.

- Noise cancelling with better noise reference signal

Even though the adaptive FIR filter can well eliminate the respiratory artefact in most circumstances. However, some patients can not breath smoothly and their respiratory pattern may vary unexpectedly which will result in considerable frequency inbanding between the respiratory and rheopneumographic components. Even the adaptive FIR filter might fail in such cases because no suitable cutoff frequency would be available.

In view of this, the signal cancelling technique with good artefact reference signal may be a solution to the problem of frequency inbanding. The ANC method with LMS algorithm did not perform satisfactorily due to its finite converging time. However, some other algorithms of fast converging feature such as the lattice algorithm may give a better result. Moreover, with the help of electrical field analysis using a 3D numerical model, a more truly optimum electrode configuration could possibly be found such that the respiratory signal can be picked up with as small cardiac components as possible. With these improvements, the modified ANC method may better remove the respiratory artefact even with possible

frequency inbanding.

- ***More complicated EIR model***

For the modeling method proposed in chapter 4, many simplifications and assumptions were made and these included: 1) treated the heart as an impulse source. This is not the case in practice because of the finite rise and fall times and smoothing effect of the heart contraction; 2) the blood vessels in the pulmonary circulation were grouped into just two parts viz, the arterial and venous parts. Each part was represented by a modified two-chamber model. Such an EIR model is too crude and some factors are not considered. These factors, such as valve functions of the heart and branching effect in major pulmonary arteries, may affect the waveform morphology. The mismatch in such branch points may also result in flow reflections and hence variations of the wave morphology.

Instead of the simple heart model, a more complicated one might be necessary to account for other features such as valve actions which posses strong non-linearities (but can be treated as piecewise linear). In the EIR model, if the pulmonic valve and the mitral valve were involved, the model output could possibly improve the overall accuracy. Some small morphological peaks (i.e., the c-wave, the x-wave in the rheopneumogram) in the waveform can also be taken into consideration so that more information can be revealed.

On the other hand, the non-linear curve fitting technique needs to be improved for locating the global minimum. In this study, the global minimum was searched by starting the algorithm at random initial values and the resulted model parameters should match to the real physiological picture. This searching approach is slow and hence very time consuming. Some fast algorithm is necessary.

7.4 APPLICATIONS OF THE EIR TECHNIQUE

As stated in chapter 1, the most attractive feature of this impedance technique is its non-invasive nature and its ability to provide real-time monitoring and on-line analysis of the pulmonary circulation all of which are hitherto unavailable. Moreover, the technique itself is

simple to employ. In china, this technique has been widely used to detect various diseases of the cardiopulmonary origin in spite of the existing limitations. Li in his book showed observations of 45 kinds of such diseases and the corresponding rheopneumograms. The most useful aspect of the technique may lie in the detection of the blood flows in the pulmonary circulation non-invasively. It is also useful in monitoring valve replacement the effect of artificial pacemaker and in assessment of results of during treatment, etc.

Studies in this work have solved some basic problems lying this technique. It is first hoped that the suggested optimum electrode configuration can be widely adopted to measure the rheopneumogram with as small interference of other origins as possible so that a "pure" rheopneumogram can be observed. Secondly, The proposed signal processing scheme provide a multi-modality monitoring method that respiration and pulmonary circulation can be observed and analyzed simultaneously. Although many researchers in China have been involved in the study of the EIR technique, there is no widely adopted analysis method. As a result, the method or result of one researcher can hardly be repeated and followed by other researchers. Hence finally, it is hoped that the EIR modeling method proposed in this study can be widely adopted because of its physiological basis and more informative feature.

[ALLI 65] Allison, R.D., Nyboer J., "*The electrical plethysmography determination of pulse volume and flow in ionic circulatory systems*", New Istanbul. Contrib. Clin. Sci., 1965, Vol. 7, pp281-306.

[AVAN 85] Avanzolini, G, Barbini, P., etal., "*Time-varying mechanical properties of the left ventricle-a computer simulation*", IEEE trans. on biomed. eng., Vol. 32, No. 10, (Oct. 1985) pp756-763.

[BAKE 89] Baker, L.E. "Principles of the Impedance Technique", *IEEE Eng. Med. Bio. Mag.*, 1989, pp11-15.

[BARA 92] Barak C, Leviatan Y, Inbar G F, "*Simulation method for cardiac stroke volume estimation by intracardiac electrical impedance measurement*", Med. & Biol. Eng. & Comput., Vol. 30, (1992) pp473-480.

[BERG 92] Berger, D. S., Li, J. K. J., "*Temporal relationship between left ventricular and arterial system elastances*", IEEE Trans. on biomed. eng., vol. 39, no. 4, Vol. 39, No. 4, (April 1992) pp404.

[BHAT 88] Bhattacharya, B., Tandon, S. N., "*Potential distribution in the thorax in relation to electrical field plethysmograph*", Med. & Biol eng. & comput., Vol. 26, (May, 1988) pp303-309.

[BOUR 83] Bourne, P. R., Kitney, R. I., "*Comparison of computer models of the human arterial system for the assessment of clinical data*", Medical & Biological Eng. & Comput., Vol. 21, (May 1983) pp319.

[BROW 83b] Brown B. H., *Tissue impedance measurement imaging with non-ionising radiations*, ed. D F Jackson (Guildford: Surrey University Press) 1983, pp85-110.

[BROW 85] Brown, B. H., Barber, D. C., etal, "*Applied potential tomography: possible clinical applications*", Clin. Phys. Physiol. Meas., Vol. 6, No. 2, (1985) pp109-121.

[BRUB 78] Brubakk, A. O., Aaslid, R., "*Use of a model for simulating individual aortic dynamics in man*", Med. & Biol. Eng. & Comput., Vol. 16, (1978) pp231--242.

[BUON 73] Buoncristiani, John F., Liedtke, A. James, etal., "*Parameter estimates of a left ventricular model during ejection*", IEEE trans. on biomed. eng., Vol. 20, No. 2, (March 1973) pp.110-114.

[BURA 83] Burattini, R., Gnudi, G., "*Assessment of a parametric identification*

procedure of simple models for left ventricular afterload", Medical @ Bio. eng. & Comput., Vol. 21, (Jan. 1983) pp39.

[BURA 82] Burattini, R., Gnudi, G., "*Computer identification of models for the arterial tree input impedance: Comparison between two new simple models and first experimental results*", Med. & Biol. eng. & comput., Vol. 20, (March 1982) pp134.

[BURG 61] Burger H. C. and van Dongen R., "*Specific electric resistance of body tissues*", Phys. Med. Biol., 1961, Vol. 5, pp431-47.

[CAMB 86] Cambell, Kenneth B., Ringo, John A., etal., "*Validation of optimal elastance-resistance left ventricle pump models*", Amer. J. Physiol., Vol. 251, (1986) ppH382-H397.

[CHOY 92a] Choy T. C., Leung C. C. and Chung Y. C. "*Rheopneumogram extraction from lung impedance plethysmogram*", Proc. Medicon'92, Capri, Italy, 1992, Vol II, pp1177-80.

[CHUN 88] Chung, Y. C. *Respiratory Artefact Elimination from Impedance Lung Rheogram*, M. Ph thesis, Dept. of Elec. Eng. CUHK, 1988.

[CLAR 80] Clark J. W. Jr, , Ling, R. Y. S., "*A two-stage identification scheme for the determination of the parameters of a model of left heart and systemic circulation*", IEEE trans. on biomed. eng., Vol. 27, No. 1, (Jan. 1980) pp20.

[COHN 78] Cohn, M.A., et al., "*A transducer for non-invasive monitoring of respiration*", in Proc. 2nd ISAM, by Stott, F.E., et al. (ed.), London, Academic Press, 1978.

[COOL 68] Cooley W. L., Longini R. L., "*A new design for an impedance pneumograph*, J. appl. physiol., Vol. 25, No. 4, (1968) pp429.

[DAGA 82] Dagan, J., "*Pulsatile mechanical and mathematical model of the cardiovascular system*", Med. & Biol. Eng. & Comput., Vol. 20, (1982) pp601-607.

[DENN 77] Dennis, J. E. Jr., "*Nonlinear Least Squares*", State of the Art in Numerical Analysis, ed. D. Jacobs, Academic Press, (1977), pp269-312.

[DINN 81] Dinnar, U., "*Cardiovascular fluid dynamics*", CRC Press, Inc. Boca Raton, Florida, 1981.

[ELLI 91] Ellis, H., etal, "*Human cross-sectional anatomy atlas of body sections and CT images*", Butterworth-Heinemann Ltd, 1991.

[ELLI 87] Elliott, D. F. *Handbook of digital signal processing*, Academic press, San

Diego, 1987.

[EMRC 91a] EMRC, NISA/DISPLAY III user's manual, 1991.

[EMRC 91b] EMRC, NISA/EMAG user's manual, 1991.

[ENDR 76] Endresen J., Hill, D.W., "*The effect of respiration on the monitoring of stroke volume and cardiac output by the electrical impedance technique*", Europ J. Intensive Care Medicine, Vol. 2, (1976) pp3-6.

[FRAN 78] Frank, P.M., "*Introduction to system sensitivity theory*", Academic Press, New York, 1978.

[GEDD 67] Geddes, L. A., Baker, L. E., "*The specific resistance of biological material - a compendium of data for the biomedical engineer and physiologist*", Med. & Biol. Engng., Vol. 5, (1967) pp271-293.

[GEDD 89] Geddes, L. A., Baker, L.E., "*Detection of physiological events by impedance*", in Principles of applied biomedical instrumentation, 3rd, 1989, (John Wiley&Sons: New York), pp537.

[GESE 71] Geselowitz, David B., "*An application of electrocardiographic lead theory to impedance plethysmography*", IEEE trans. on biomed. eng., Vol. 18, No. 1, (Jan. 1971) pp38-41.

[GOLD 67] Goldwyn, Roger M., Watt, Thomas B., "*Arterial pressure pulse contour analysis via a mathematical model for the clinical quantification of human vascular properties*", IEEE trans. on biomed. eng., Vol. 11, No. 1, (Jan. 1967).

[GREE 73] Greene M. E., Clark, J. W., et al. "*A mathematical model of left ventricular function*", Med. Biol. Eng., vol.11, (1973), pp126-134.

[HADI 72] Hadijev, D. "*Impedance methods for investigation of cerebral circulation*", Prog. Brain Res., 1972, Vol. 35, pp25-85.

[HARD 82b] Hardy, H. H., Collins, R. E., "*A digital computer model of the human circulatory system*", Med. & Biol. eng. & Comput., Vol. 20, (Setp. 1982).

[HOWE 65] Howells, P., "*Intermediate frequency side-lobe canceller*", U. S. Patent 3 202 990, Aug. 24, 1965.

[HUGH 87] Hughes, T. J. R., *The finite element method - Linear static and dynamic finite element analysis*, Prentice-Hall, 1987.

[ICEBI 92] Proceedings of the 8th International Conference on Electrical Bio-impedance: 1992 July: Kuopio, Finland.

[ICEBI 87] Proceedings of 7th International Conference on Electrical Bio-impedance: 1987: Klagenfurt, Austria.

[ICEBI 83] Proceedings of 6th International Conference on Electrical Bio-impedance: 1983: Zadar, Yugoslana.

[ICEBI 81] Proceedings of 5th International Conference on Electrical Bio-impedance: 1981 August: Tokyo, Japan.

[KENT 81b] Kentie M. A., Schee E. J. van der, etal, "*Adaptive filtering of canine electrogastrographic signals. Part 1: system design*", Med.& biol. eng.& comput., Vol. 19, (1981) pp759-764.

[KENT 81a] Kentie, M. A., Schee, E.J.van der, etal, "*Adaptive filtering of canine electrogastrographic signals. Part 2: filter performance*", Med. & Biol. eng. & comput., Vol. 19, (1981) pp765-769.

[KIM 86] Kim, D. W., Baker, L. E., "*Electrode configurations of impedance cardiography by 3d FEM*", IEEE/Eighth annual conference of the engineering in medicine and biology society, (1986).

[KIM 88] Kim, D. W., Baker, L. E., "*Origins of the impedance change in impedance cardiography by a three-dimensional finite element model*", IEEE trans. on biomed. eng., Vol. 35, No. 12, (Dec. 1988).

[KING 67] King, R.E.:"*Parametric sensitivity of physiological system-prognostic analysis*", IEEE trans. on Biomed. eng., vol BME-14 (1967) No. 4, pp209-215.

[KUBI 74] Kubicek, W.G., et al., "*The minnesota impedance cardiograph theory and applications*", Biomed Eng., 1974, Vol. 9, pp410.

[KUBI 66] Kubicek, W.G., et al., "*Development and evaluation of an impedance cardiac output system*", Aerosp. Med. 1966, Vol 37, pp1208-12.

[KUWA 81] Kuwahira, I., et al., "*Static and dynamic aspects of pulmonary circulation assessed by simultaneous measurements of six local electrical impedances*", Proc. of the VIth ICEBI, 1981, Tokyo.

[LEHR 72] Lehr, J., "*A vector derivation useful in impedance plethysmography field calculations*", IEEE trans. on biomed. eng., (Mar. 1972) pp156.

[LI 92a] Li, Z. M., et al. "*Cardiac admittance differential loop - a new method for the detecting of cardiac functions*", Proc. of ICEBI '92, Kuopio, 1992.

[LI 82] Li X. Z. *Clinical impedance rheography of the lung*, Heilongjiang Sci. &

Tech. Press.

[LI 83a] Li, X. Z., Cheng, S. Y., "*Lung rheography used as a non-invasive method for observing the left heart preload and monitoring the pulmonary circulation*", Proc. of VIth ICEBI, Zadar, (1983), pp328-333.

[LI 83b] Li, X. Z., et al, "*Study on the regularity of the changes of the lung impedance rheography in the aged*", Proc. of VIth ICEBI, Zadar, (1983), pp334-338.

[MARQ 63] Mardquardt, D.W. "*An algorithm for least-squares estimation of nonlinear parameters*", J. Soc. Ind. App. Math., 1963, Vol.11, No.2, pp431-441.

[MILN 90] Milnor, W. R., "*Cardiovascular physiology*", Oxford University Press, New York Oxford, 1990.

[MIYA 81] Miyamoto Y., Takahashi M., et al "*Continuous determination of cardiac output during exercise by the use of impedance plethysmograph*", Med. & Biol. Eng. & Comput., 1981, 19, pp638-644.

[MOLL 84] Moller, D., et al., *Modelling, Simulation and Parameter-Estimation of the Human Cardiovascular System*, in Advances in control systems and signal processing, vol 4, I. Hartmann (Ed.), 1984, Vieweg&Sohn.

[MUZI 85] Muzi, M., Ebert T. J., et al "*Determination of cardiac output using ensemble-averaged impedance cardiograms*", J. Appl. Physiol., 1985, 58, pp200-205.

[NYBO 44] Nyboer, J., "*Electrical impedance plethysmography*", In Medical Physics, Vol. 1, ed., Glasser, O., Year Book Pubblishers, Chicago, IL, 1944, pp744.

[NYBO 50] Nyboer, J., "*Electrical impedance plethysmography*", Circulation, 1950, Vol 2, pp811-887.

[NYBO 59] Nyboer, J., "*Electrical impedance plethysmography*", Thomas, Springfield, IL, 1959.

[PATT 78] Patterson R. P. "*The use of signal averaging of the electrical impedance signal to determine cardiac timing information during uninterrupted exercise*", Proc. 13th Ann. Meeting of AAMI, Arlington, Virginia, USA, 1978, pp206.

[PATT 85] Patterson, R. P., "*Sources of the thoracic cardiogenic electrical impedance signal as determined by a model*", Med. & Biol. Eng. & Comput., Vol. 23, (1985) pp411-417.

[PENN 86] Bill, C. P. "Theory and Cardiac application of Electrical Impedance

Measurements", *CRC Critical Reviews in Biomedical Engineering*, 1986, Vol. 13, Issue 3, pp227-281.

[PLON 77] Plonsey, R., Collin, R., "*Electrode guarding in electrical impedance measurements of physiological systems-a critique*", Med. & Biol. Eng. & Comput., Vol. 15, (1977) pp519-527.

[QU 86] Qu, M. H., Zhang, Y.J., Webster, J. G., "*Motion artifact from spot and band electrodes during impedance cardiography*", IEEE Trans. on Biomed. Eng., Vol. BME-33, No. 11, (Nov. 1986) pp1029.

[ROSS 83] Ross J. S., Wilson, K.J.W, *Foundations of anatomy & physiology*, Churchill Livingstone, 1983.

[SEVE 72] Severinghaus J. W., et al., "*A focusing electrode bridge for unilaterial lung resistance*", J. Apppl. Physiol. (1972) Vol. 32 pp526-30

[SHIM 81] Shimazu, H. Yamakoshi K., et al., "*Non-invasive measurement of blood resistivity and haematocrit*", Proc. Vth Int. Conf. Electrical Bioimpedance (ICEBI), tokyo, pp233-8.

[SPEN 63] Spencer, M.P., Denison, A.B., "*Pulsatile blood flow in the vascular system*", in Handbook of Physiology, vol. 11, No. 2, Washington, DC: Amer. Physio. Soc., 1963, ch.25.

[SPIE 83] Spier, S., England, S., "*The respiratory inductive plethysmograph: bands versus jerkins*", Am. Rev Resp. Disease, Vol. 127, No. 6, (June 1983) pp784.

[STUC 84] Stuchly M. A., Stuchly S.S., "*Electrical properties of biological substance*", Biological effects an medical applications of electromagnetic fields, ed. Gandhi, O. P. (New York: Academic).

[TOY 85] Toy. S. M., "*Reduced models of arterial system*", IEEE trans. on biomed. eng., Vol. 32, No. 2, (Feb. 1985) pp174.

[WATS 80] Watson, H. "*The technology of respiratory inductive plethysmography*", Proc. 3rd ISAM, by Stott, F.D., Raftery, E.B. and Goulding, L. (ed.), London, Academic Press, 1980.

[WEGL 83] Weglarz, J, et al. "*Attempt on the assessment of the coronary flow by the precordial rheogram*", Proc. of VIth ICEBI, Zadar, (1983), pp107-111.

[WEST 79] West, J.B., *Respiratory physiology-the essentials*, 2nd ed., 1979, Williams & Wilkins.

[WHEE 73] Wheeler, H.B., et al., "*Impedance testing for venous thrombosis*", Arch.

Surg., 1973, Vol. 106, pp762-763.

[WHEE 74] Wheeler, H.B., et al., "*Occlusive venous phlebography*", Prog. Cardiovasc. Dis., 1974, Vol. 17, pp199-203.

[WIDR 75] Widrow, B. et al "*Adaptive noise cancelling: Principles and applications*", Proc. IEEE, 1975, vol.63, no.12, pp1692.

[XION 83] Xiong, J.F., et al, "*Observations on experimental pulmonary electrical impedance plethysmogram (rheopneumogram) III. Correlation between right and/or left heart function and rheopneumogram*", Proc. of VIth ICEBI, Zadar, 1983.

[XION 81] Xiong, J.F, et al., "*Observations on experimental pulmonary electrical impedance plethysmogram*", Proc. of the Vth ICEBI, 1981, Tokyo.

[YE 92c] Ye, J. and Choy, T.T.C. "*Peak model analysis of electrical impedance wave of pulmonary circulation*", Proceedings of BME'92, Hong Kong, 1992, pp150-153.

[ZIEN 89] Zienkiewicz, O. C. and Taylor R. L., *The finite element method*, vol.1, McGRAW-Hill, 1989.

APPENDICES

APPENDIX A. A CIRCUIT DIAGRAM FOR THE FOUR-ELECTRODE SYSTEM

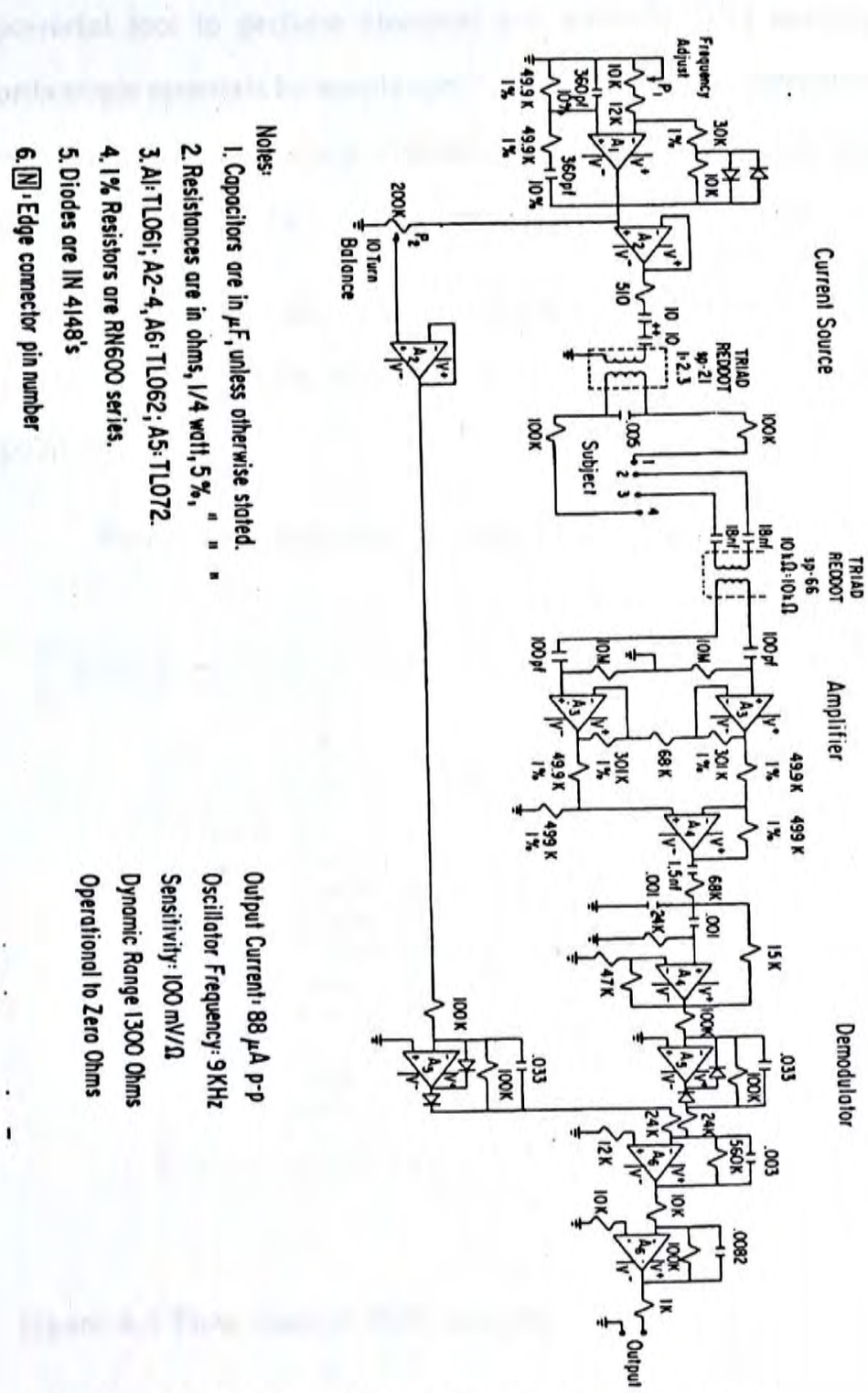

Figure A.1 A circuit diagram of the four-electrode system.

APPENDIX B. NISA/EMAG (A SOFTWARE PACKAGE OF FEM)

NISA/EMAG is a 2D and 3D general purpose program for computer aided analysis and design of electromagnetic devices. The program provides the design engineering with a powerful tool to perform electrical and magnetic field analysis in linear, nonlinear and orthotropic materials by simply specifying the material properties and excitation sources along with appropriate boundary conditions. NISA/EMAG is also capable of performing field computations under DC, AC and transient loading conditions.

The output of this program contains values for electric fields, magnetic fields, currents and power distributions, which are the most important parameters from a design optimization point of view.

Following a flow chart of using FEM to solve a problem is given.

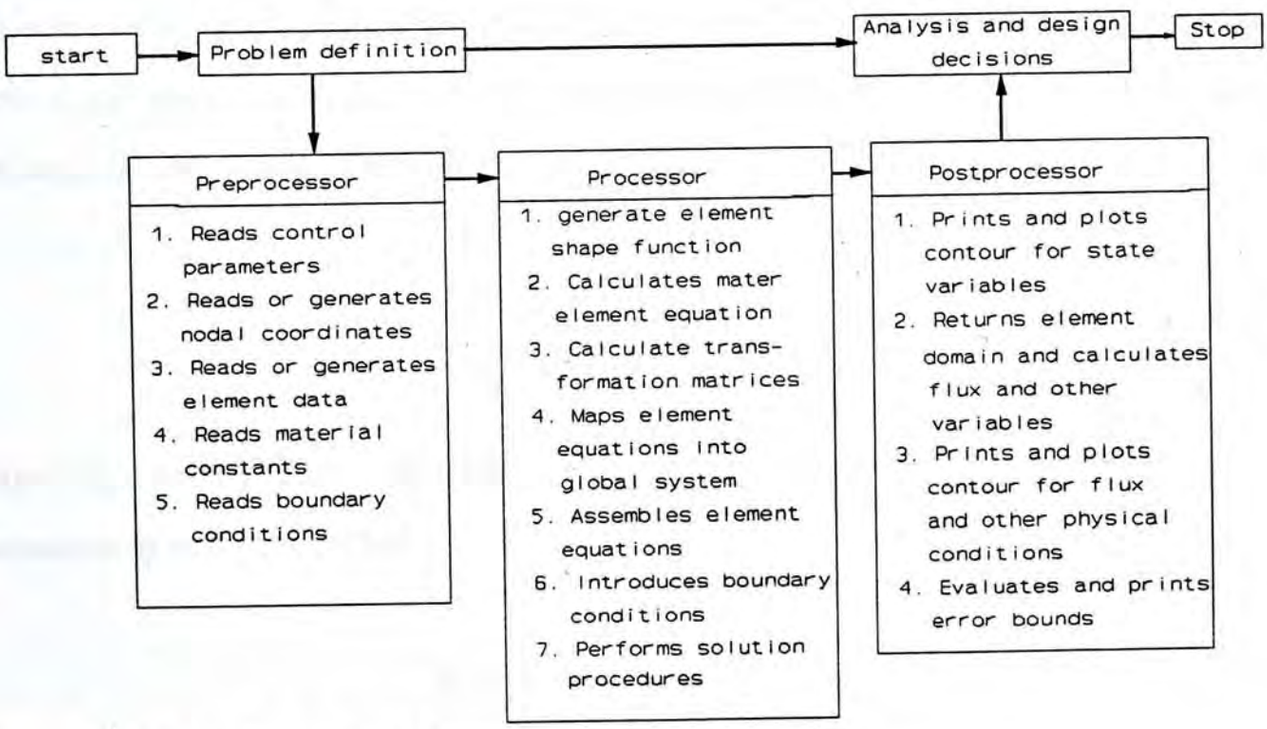

Figure A.1 Flow chart of FEM solution.

APPENDIX C. LMS ALGORITHM[1]

The adaptive filter is the heart of the adaptive noise canceller. Figure A.3 shows how a FIR filter is used in the noise canceller. The filter weights and sums the signal from the primary input. Following the notations in figure A.3, the filter output at the i^{th} instant is given by

$$y_j = X_j^T W_j = W_j^T X_j \tag{A.1}$$

where $X_j = [x_j, x_{j-1}, \ldots, x_{j-n+1}]^T$

$W_j = [w_{1j}, w_{2j}, \ldots, w_{nj}]$

n = the filter order

The weigths of the adaptive filter are adjusted for every input sample with the aim of minimizing the mean-square error. Assuming that the filter input signal x_j and the primary input d_j are statistically stationary (see figure 4.5 also figure A.3), a general expression for the mean-square error as a function of the wight vector can be derived as follows:

$$\begin{aligned} e_j &= d_j - y_j = d_j - X_j^T W_j \\ E[e_j^2] &= E[d_j^2] - 2P^T W_j + W_j^T R W_j \end{aligned} \tag{A.2}$$

where E[] stands for the expectation, P is the cross-correlation vector and R is the input correlation matrix defined by

$$P = E[d_j\ X_j], \qquad R = E[X_j\ X_j^T] \tag{A.3}$$

Using the steepest-descent method and approximating gradient mean-square error by gradient square error

[1] This description of the LMS algorithm is based on Widrow and Chen ([WIDR 75] [CHEN 89]).

$$W_j+1=W_j-\mu\nabla_j\ , \quad \nabla_j=\partial e_j^2/\partial W_j \tag{A.4}$$

The Widrow-Hoff LMS algorithm ([WIDR 75]) is derived:

$$W_{j+1}=W_j+2\mu e_j X_j \tag{A.5}$$

where μ is the step-size which controls the stability and the rate of the convergence.

The LMS algorithm required that the next weight vector W_{j+1} is equal to the present weight vector W_j plus a change proportional to an estimate of the negative gradient of the error surface. After the convergence of the algorithm the weight vector obtains its optimal value and the mean-square error is minimised.

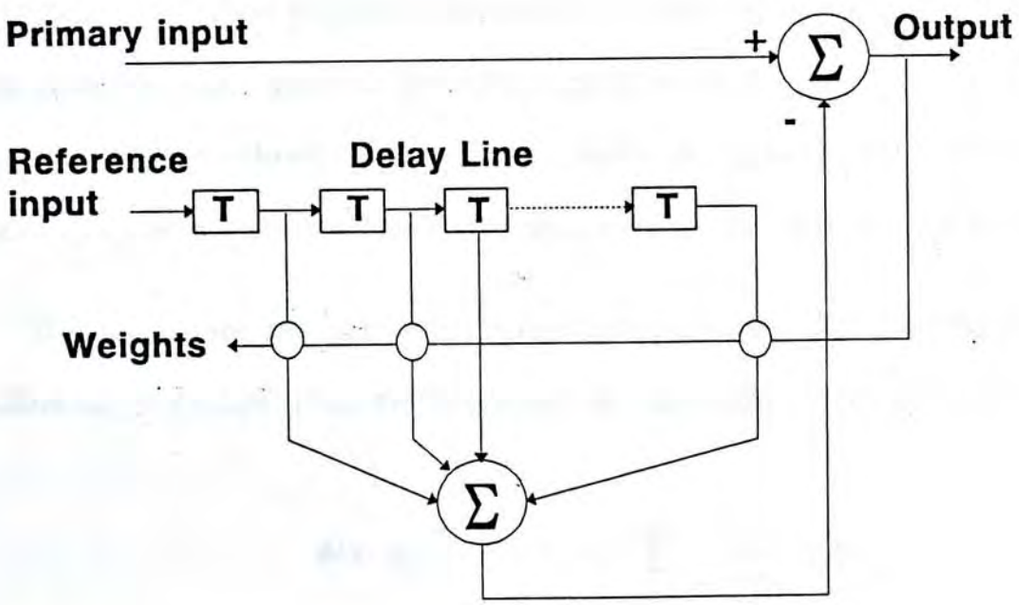

Figure A.3 Adaptive noise canceller.

APPENDIX D. CURVE FITTING

HESSIAN METHOD

Following the introduction in section 5.4.2, where we defined a fitting function and an error function

$$y=f(x;a)$$

$$\phi=\sum_{i=0}^{n}\left[\frac{f(x_i)-y_i}{\sigma_i}\right]^2 \tag{A.6}$$

If the fitting function f is linear in the a's, the contours of constant Φ are ellipsoids, and the optimization can be carried out by standard linear methods, setting

$$\frac{\partial\phi}{\partial a_j}=0 \tag{A.7}$$

for all j. However, when f is non-linear in the a's, the contours are distorted. Typically, they are attenuated in some dimensions and elongated in others, so that the minimum value lies the bottom of a long curving trough-shaped valley. In addition, there is a strong possibility that there may be a number of such valleys, each of which has its own local minimum.

If we had some accurate initial guess for the a's, we could find the minimum of Φ by the following procedure. Near the minimum, we can expand Φ as a Taylor series,

$$\phi(x;\ a_0+\delta a)=\phi(x;\ a_0)+\sum_j \frac{\partial^2\phi}{\partial a_j\partial a_k}\delta a_j\delta a_k \tag{A.8}$$

if we define

$$c\equiv\phi(x;\ a_0) \qquad b\equiv-\nabla\phi\,|_{x;\ a_0} \qquad [H]_{j,k}\equiv\frac{\partial^2\phi}{\partial a_j\partial a_k}\,|_{x;\ a_0} \tag{A.9}$$

then we can write in matrix notation

$$\phi(x;\ a_0+\delta a)=c-b\cdot\delta a+\frac{1}{2}\delta a\cdot H\cdot a \tag{A.10}$$

where the matrix H, whose components are the second partial derivatives of Φ with respect to the adjustable parameters, is called the Hessian matrix.

If we take the gradient of the previous equation,

$$\nabla_a\phi\,|_{x;\ a_0+\delta a}=H\cdot\delta a-b \tag{A.11}$$

then we can find the minimum of Φ, where its gradient vanishes, by solving the equation

$$H\cdot\delta a=b \tag{A.12}$$

This is called the Hessian method.

MARQUARDT ALGORITHM

Marquardt ([MAEQ 63]) has suggested a method, which varies from the gradient method, used far from the minimum, to the Hessian method, as the minimum is approached. He first chooses the constant to scale the step size in the gradient method,

$$\delta a_j=\frac{b_j}{\lambda H_{jj}} \tag{A.13}$$

since b_j has the dimensions of $1/a_j$, dividing by the diagonal term of the Hessian H_{jj} scales the equation to the appropriate dimensions. The quantity λ is a dimensionless factor which we can adjust to further reduce the step size.

The gradient and Hessian methods are combined by defining a new matrix

$$\begin{aligned}\hat{H}_{jj} &= H_{jj}(1+\lambda)\\ \hat{H}_{jk} &= H_{jk} \quad (j\neq k)\end{aligned} \tag{A.14}$$

and then δa_k is found by solving

$$\sum_{j=1}^{n} \hat{H}_{jk}\delta a_j = b_k \qquad \text{(A.15)}$$

To implementing the algorithm, the search direction and integral error are calculated according to the following steps and the loop is continued until a final minimum is reached,

1. Choose a starting value a for the parameter.
2. Compute $\Phi(a)$.
3. Pick a value for λ, say 10^{-3}.
4. Solve the equation (A.12) for δa and evaluate $\Phi(a+\delta a)$.
5. If $\Phi(a+\delta a) > \Phi(a)$, increase λ by a factor of 10 and go back to 4.
6. If $\Phi(a+\delta a) < \Phi(a)$, decrease λ by a factor of 10, replace a by $a+\delta$ and go back to 4.

APPENDIX E. LIST OF PUBLICATIONS

[1] Choy, TTC, Ye, J., "***Scarred tissue characterisation with transient thermal response of TcPO2***", Proc. 16th Inter. Conf. on med. & Bio. Engg. & 9th Inter. conf. on Med. Phys., Japan, 1991.

[2] Choy, TTC, Ye, J., "***On-line Respiratory Artefact Removal in Rheopneumographic Measurement Via Moving Average Method***", Proc. CMBES Conf., '92, Toronto, Canada, p148-149.

[3] Choy, TTC, Ye J., "***Modelling Analysis of the Rheopneumogram Via Bio-electrical Impedance Technique"***, Proc. of ICEBI '92, Kuopio, Finland, July 92, p54-56. A more detailed version of this paper has been submitted to the journal *Medical Progress Through Technology* for consideration of publication.

[4] Ye, J., Choy, TTC., "***On Line Respiratory Artefact Elimination in Rheopneumographic Measurement***", Proc. ISSPA'92, Queensland, Australia, p501-504.

[5] Ye, J., Choy, TTC., "***Modelling of the Pulmonary Circulation via Electrical Bio-impedance Technique***", Proc. of 14th Annual IEEE-EMBS Conf., Oct. Paris, 1992.

[6] Ye, J., Choy, TTC., "***Peak Model Analysis of Electrical Impedance Wave of Pulmonary Circulation***", Proc. BME'92, Hong Kong.

[7] Ye, J., Choy, TTC., "***Analysis of electrical field in the human thorax via a numerical model and finite element method***", submitted to FECMBE'93, Beijing, China (accepted).

[8] Ye, J., Choy TTC., "***On-line respiratory artefact removal via adaptive FIR filter in rheopneumographic measurement***", been submitted to *Medical & Biological Engineering & Computing* for consideration of publication.

[9] Choy, TTC., Ye, J., "***On-line respiratory artefact removal in rheopneumographic measurement via an adaptive moving average method***", has been accepted by *Electronic Letters* for publication.

[10] Choy, TTC, Ye, J., Xiong, GF., Chan, HS., ***Non-invasive estimate of the properties of the pulmonary circulation from electrical impedance rheopneumographic***

measurements by modeling method, submitted to Journal of Biomedical Eng. for consideration of publication.

[11] Ye, J., Choy, TTC., "***Respiratory artefact elimination via adaptive FIR filter in zrheopneumographic measurement***", accepted by SICON/ICIE'93, Singapore.

[12] Ye, J., Choy TTC., "***Search of optimal electrode configuration for impedance rheopneumographic measurements by finite element method***", accepted by CMBES'93, canada.

[13] Choy TTC., Leung, GCC., Ye, J., "***An improved model for the impedance rheopneumogram***", accepted by CMBES'93, canada.

[14] Choy TTC., Ye J., et al., "***An EBI technique for simultaneous RT monitoring of respiration and pulmonary circulation***", accepted by FECMBE'93, Beijing.

[15] Yu, KY, Choy TTC., Ye, J., Chu, SM., "***A Quantitative Method of Exercise Value Assessment via Circuit Model of the Radial Pulsewave***", accepted by FECMBE'93, Beijing.